UNIVERSITY OF CALIFORNIA,
IRVINE

Functions and clinical relevance of voltage-sensitive proteins without pore domains

DISSERTATION

submitted in partial satisfaction of the requirements
for the degree of

DOCTOR OF PHILOSOPHY

in Biomedical Sciences

by

Iris H. Kim

Dissertation Committee:
Professor Francesco Tombola, Chair
Professor Ivan Soltesz
Professor Albert Zlotnik

2014

DEDICATION

To my family – Heakyung, Youngil, Irene Kim and Rodrigo Torres.

To my advisor – Francesco Tombola.

TABLE OF CONTENTS

LIST OF FIGURES

LIST OF TABLES

ACKNOWLEDGMENTS

I would like to express the deepest appreciation to my committee chair, Professor Francesco Tombola. Professor Tombola has been both a wonderful presence and exceptionally intelligent person to look up to. Without his guidance and persistent help this dissertation would not have been possible. I am so grateful for his support and mentorship.

I would like to thank my committee members, Professor Ivan Soltesz and Professor Albert Zlotnik, who have given me valuable advice and guidance. I am honored to have them both as my committee members.

I thank everyone who has assisted me during my work in the Tombola lab. I thank Dr. Liang Hong, who has been a great colleague. I thank Truc Tran, Chau Tran, and Dennis Ta, who have given me assistance during my work in the lab. I thank Dr. Medha Pathak for giving me valuable advice about how to think about science in general, and I am a better scientist today for working in the same lab as her. I would also like to thank Logan Roberts and Dr. Amanda Burkhardt for their support.

I thank my family, to whom this thesis is dedicated, and to my friends. Thanks to my jaeger co-pilot Abbie Theuma for all her support during the writing of this thesis.

I would also like to thank and give recognition to Josh M. Clark and Charles W. "Chuck" Bryant. There was a period of time I deeply considering leaving graduate school, but, of course, I didn't. It would not have been possible for me to complete my degree if they hadn't come along into my life at exactly the right moment.

I thank Cell Press for allowing permission for the reprinting of Chapter 2, and the authors who contributed to the work: Dr. Liang Hong, Dr. Medha Pathak, Dennis Ta, and Dr. Francesco Tombola. I also thank the Proceedings of the National Academy of Sciences for permission for reprinting of Chapter 3, and the authors who contributed to the work: Dr. Liang Hong and Dr. Francesco Tombola. I also thank the Public Library of Science for the reprinting of Chapter 4, and the authors who contributed to the work: Dr. Csaba Varga, Dr. Peter Hevezi, Dr. Medha Pathak, Dr. Liang Hong, Dennis Ta, Dr. Albert Zlotnik, Dr. Ivan Soltesz, and Dr. Francesco Tombola. Financial support was provided through the American Heart Association and the National Institutes of Health.

CURRICULUM VITAE

Iris Kim

EDUCATION

Doctor of Philosophy in Biomedical Science **2014**
University of California, Irvine *Irvine, California*

Bachelor of Science in Biological Science **2008**
University of California, Irvine *Irvine, California*

RESEARCH EXPERIENCE

Graduate Student Researcher **2009 – 2014**
Tombola Lab, University of California, Irvine *Irvine, California*

Laboratory Manager **2008 – 2009**
Schilling Lab, University of California, Irvine *Irvine, California*

Undergraduate Researcher **2007 – 2008**
Schilling Lab, University of California, Irvine *Irvine, California*

Undergraduate Researcher **2006 – 2007**
Brachmann Lab, University of California, Irvine *Irvine, California*

MEMBERSHIPS

Biophysical Society **2012 – Present**

PUBLICATIONS

Kim, I.H., Hevezi, P., Varga, C., Pathak, M.M., Hong, L., Ta, D., Zlotnik, A., Soltesz, I., Tombola, F. (2014). Functional diversity between the voltage-gated proton channel Hv1 and its closest related protein HVRP1. PLOS One. **Under revision**.

Hong, L., **Kim, I.H.**, Tombola, F. (2014). Molecular determinants of Hv1 proton channel inhibition by guanidine derivatives. Proceedings of the National Academy of Sciences of the United States of America. **In press.**

Hong, L., Pathak, M.M., **Kim, I.H.**, Ta, D., and Tombola, F. (2013). Voltage-sensing domain of voltage-gated proton channel Hv1 shares mechanism of block with pore domains. Neuron *77*, 274–287.

TEACHING AND ORGANIZATION EXPERIENCE

Physiology & Biophysics Department Research in Progress **2013 – 2014**
Head of seminar organization

Teaching Assistant, Cell Biology **Winter 2013**
Undergraduate course, University of California, Irvine *Irvine, California*

Teaching Assistant, Ion Channels **Spring 2013**
Graduate course, University of California, Irvine *Irvine, California*

Teaching Assistant, Advanced Biochemistry Lab **Winter 2011**
Undergraduate course, University of California, Irvine *Irvine, California*

ABSTRACT OF THE DISSERTATION

Functions and clinical relevance of voltage-sensitive proteins without pore domains

By

Iris Kim

Doctor of Philosophy in Biomedical Sciences

University of California, Irvine, 2014

Professor Francesco Tombola, Chair

Voltage-gated ion channels contain a voltage-sensing domain and a pore domain. Two families of proteins have been identified that contain the voltage-sensing domain but no pore domain, the family of voltage-sensitive phosphatases and the family of voltage-gated proton channels. Hv1, the only known voltage-gated proton channel, has clinical relevance, having been found at high expression levels in cancer cell lines, and the inhibition of Hv1 has shown to slow the growth of cancer cells. Previously, there were no known blockers of this channel that could be developed for therapeutic use. Here I have identified two intracellular blockers of Hv1. The first, 2GBI, is an open channel blocker accessible from the intracellular side. The second, ClGBI, is also an open channel blocker but accessible from the extracellular side. Through mutagenesis of the Hv1 channel and electrophysiology techniques, we have investigated the binding environment of this inhibitor and studied the mechanism of intracellular gating in Hv1. Next, due to the clinical significance of Hv1, we searched for related voltage-sensitive proteins without a pore domain, and identified Hv1's closest related protein, called HVRP1. Using a combination of techniques including in situ hybridization, immunocytochemistry, and electrophysiology, I have begun initial

characterization of this new member of the family of voltage-sensitive proteins without a pore domain. The novelty of this research represents an entirely new family of proteins whose function is yet unknown, but likely to be a function yet unassociated with pore-domain-lacking voltage-sensitive proteins.

Chapter 1: Introduction

1.1 Voltage-gated ion channels

Ion channels are macromolecular pore-forming proteins found in the membranes of nearly all cells of an organism (Hille, 2001). They play important roles in numerous biological processes, including the establishment of a resting membrane potential and the shaping of electrical signals (Hille, 2001; Terlau and Stühmer, 1998).

There are other membrane proteins that transport ions in cell membranes, but two features distinguish ion channels from other transporter proteins. First, ion channels are able to permeate ions at a very high rate, often around 10^6 ions per second. Second, these ions are permeated down their electrochemical gradient, influenced by ion concentration and membrane potential, without the use of metabolic energy such as ATP (Hille, 2001).

All ion channels must respond to some type of stimulus in order to open or close, letting ions through, or disallowing them from pass in or out of the cell. Ion channels are thus divided into one of three superfamilies depending on whether they are voltage-gated, ligand-gated, or mechanosensitive. There are multiple other ion channel sub-families, however, including transient receptor potential (TRP) channels, whose members are activated by a wide range of stimuli, such as voltage, pH, mechanical stretch, and heat. Here, the superfamily of voltage-gated ion channels will be reviewed.

Voltage-gated ion channels

Channels in the superfamily of voltage-gated ion channels, found in excitable cells, play central roles in the nervous system by generating and propagating electrical signals (Hille, 2001). These proteins are activated by a depolarization of the membrane, which results in a conformational change of the protein. This change in conformation then allows ions to permeate through them. Thus, membrane potential both influences the open probability of the channel's gate, and acts as a driving force for ions going through the open gate. Many voltage-gated ion channels are composed of multiple subunits, arranged so that each subunit surrounds a central pore through which the ions permeate. Although multiple ions of similar size and charge can sometimes flow through them, voltage-gated ion channels are generally highly selective for their major permeant ion, and thus are further subdivided into these families: the sodium (Na^+), potassium (K^+), and calcium (Ca^{2+}) channels. Na^+ and K^+ channels are found in nerve and muscle cells, and have important roles in the generation and propagation of action potentials. Ca^{2+} channels have roles that include neurotransmitter release in pre-synaptic nerve endings.

Voltage-gated Na^+ channels

Voltage-gated Na^+ channels are essential for the rapid depolarization of nerves, in the rising of action potentials (Hille, 2001). A Na^+ channel from *Electrophorus electricus* was the first voltage-gated ion channel to be cloned. The cloning occurred in 1984 and revealed the presence of four repeated homology domains, I through IV. Eukaryotic members of the Na^+

channel family are all composed of this structural motif, with each of these four repeated domains being made up of six α-helices (Fig. 1.1). An analysis of the protein's amino acid sequence to predict its secondary structure and local hydropathy showed five hydrophobic regions, S1, S2, S3, S5, and S6. Another segment, named S4 and located between S3 and S5, was unique due to the presence of positively charged residues at every third position, the majority of those being arginines. It was determined from this study that S5 and S6 are most likely transmembrane α-helices. They are made up of a sequence characteristic of transmembrane protein segments, a span of 24 to 38 uncharged amino acids, many of which are nonpolar. S1, S2, and S3, on the other hand, contain hydrophobic regions 18 to 28 residues (Noda et al., 1984). This family contains 9 currently known members.

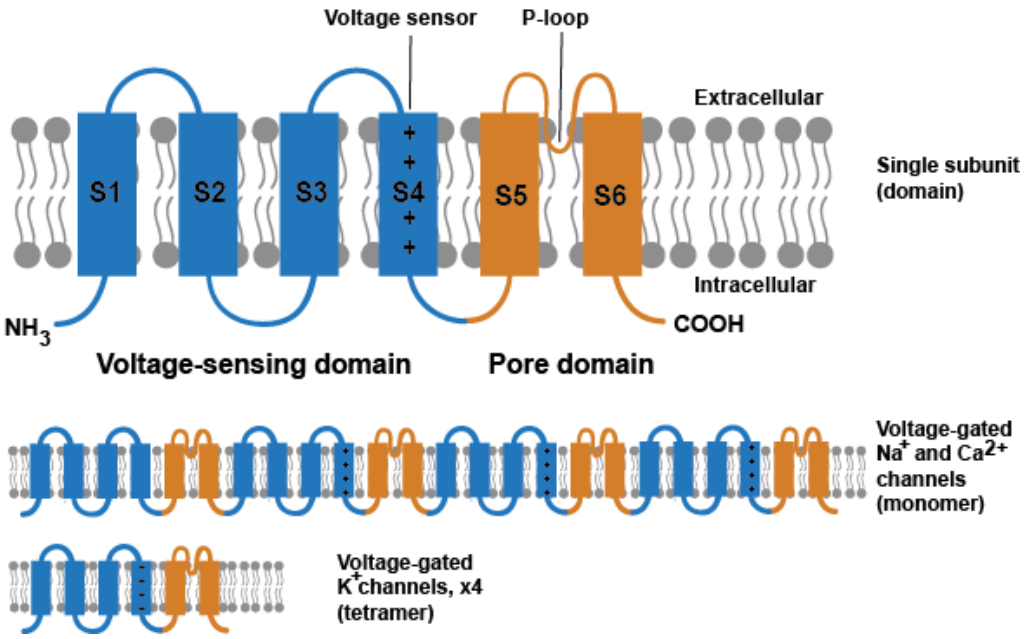

Figure 1.1. Topological organization of voltage-gated ion channels. Transmembrane segments S1 through S4 segments making up the voltage-sensing domain are pictured in blue, and transmembrane segments S5 and S6 making up the pore domain are shown in orange.

Voltage-gated Ca^{2+} channels

A few years after the cloning of the first Na^{+} channel, a Ca^{2+} channel from rabbit skeletal muscle was sequenced (Tanabe et al., 1987). These studies showed that these channels are homologous with the voltage-gated Na^{+} channel, in both amino acid sequence and topology of their transmembrane segments.

There are ten currently known members of the voltage-gated Ca^{2+} channel family, which all are activated by membrane depolarization and mediate the influx of Ca^{2+} in response to action potentials (Catterall, 2011). Many different neurological processes in the body are regulated by calcium – the release of neurotransmitters, neurosecretion, neuronal

excitation, and many others are all regulated by the cellular Ca^{2+} concentration. In presynaptic nerve terminals, neuronal Ca^{2+} channels are responsible for initiating neurotransmitter release by allowing the entry of Ca^{2+} upon depolarization (Catterall, 1995). Voltage-gated Ca^{2+} channels also have roles in cardiac action potential propagation, neurotransmitter and hormone release, and initiation of rapid muscle contraction (Catterall, 2011).

Voltage-gated K^+ channels

The largest group in this subfamily of voltage-gated ion channels is the voltage-gated K^+ channels. These channels were first identified in the fruit fly *Drosophila melanogaster* as the product of the *Drosophila* gene that encodes for the *Shaker* mutation. Several groups identified and cloned this gene at around the same time (Kamb et al., 1987; Kecskemethy et al., 1987; Tempel et al., 1987). The most well-studied function of these channels is the repolarization of the cell membrane after an action potential, which therefore makes voltage-gated K^+ channels necessary for proper function of the heart and brain and other parts of the nervous system (Hille, 2001). In all, this family of voltage-gated channels contains about 40 members, categorized into 12 subfamilies.

Most voltage-gated K^+ channels function as tetramers, where the four subunits come together to form a central pore domain. The oligomeric nature of this channel is necessary, since four subunits are needed to form a functioning ion conduction pathway (Doyle et al., 1998). The first structure of an eukaryotic voltage-gated K^+ channel was determined by X-

ray crystallography in 2005 confirming the tetrameric organization of the channel and revealing a previously unanticipated arrangement of the four voltage-sensing domains around the pore domain (Long et al., 2005).

Channelopathies associated with voltage-gated ion channels

Impaired ion channel function has been implicated in many neurological diseases. Voltage-gated ion channels, in particular, are the targets of many mutations that lead to a variety of disorders of hyperexcitability such as epilepsy, migraine, and cardiac arrhythmia (Catterall et al., 2008). It was shown in 1991 that mutation of the parts of the Na^+ channel responsible for inactivation in muscles caused hyperkalemic periodic paralysis, also known as muscular paralysis. It was observed in horses, but was found to also affect humans (Rojas et al., 1991). Following this discovery, many clinical diseases have been found to be associated with voltage-gated ion channels.

Channelopathy is the term given to diseases that result from ion channel dysfunction. The causes of channelopathies are diverse – these diseases can arise from genetic, autoimmune, or even toxic mechanisms. However, the most common cause of channelopathies is genetic, when mutations in the genes coding for ion channels occur. Interestingly, channelopathies of the central nervous system (CNS) are rare, although ion channels are widely abundant in the CNS. CNS channelopathies do overlap with known neurodegenerative diseases such as Alzheimer's, ataxia, epilepsy, and migraine (Li and Lester, 2001).

Episodic ataxia type I, resulting from K^+ channel mutation, is thought of as the human equivalent of the *Shaker* mutation in *Drosophila* (Browne et al., 1995; 1994; Comu et al., 1996), which was named because mutation to that gene caused the fly's legs to shake under ether anesthesia. Typically, channelopathies such as this are a result of up- or down-regulation/activation of the mutated channel in question. Other well-studied channelopathies include epilepsy, cardiac arrhythmia, renal failure, and migraine (Ashcroft, 1999; 2006). Over 60 ion channel genes have been found now that are associated with human disease (Ashcroft, 2006), making ion channels an attractive target for drug design and disease treatment.

Voltage-gated ion channel structure

Since the large size and amphiphilic nature of ion channels have made solving their three-dimensional structure by X-ray crystallography or NMR difficult, the first structural data of channel proteins was provided by electron microscopy (Terlau and Stühmer, 1998). Electron microscopy images of the Shaker K^+ channel revealed that it was square-shaped, with a large vestibule at the center of the protein, and four-fold symmetry. The vestibule was presumed to be the part of the pathway for ions (Li et al., 1994).

The crystal structure of a mammalian voltage-gated K^+ channel Kv1.2 was published in 2005, with the activation gate of the pore open. The selectivity filter was shown to be near the extracellular surface, where the pore is wider. The pore narrows on the intracellular side, giving it the appearance of an "inverted teepee" (Long et al., 2005).

An atomic resolution crystal structure for the Na^+ channel from the prokaryote *Arcobacter butzleri* (the channel is abbreviated NavAb) was published in 2011, revealing the channel in a closed-pore conformation and the voltage sensor in an activated state, which was an unusual combination due to two cysteine introductions near the intracellular side of S6. This allowed for the closed pore - presumably in a pre-open state while the voltage sensors were activated, at 0 mV(Payandeh et al., 2011).

The structure of the Na^+ channel allowed for analysis of the basis for selectivity and high conductance of the Na^+ ions. The pore of the NavAb has an outer funnel-shaped vestibule, a selectivity filter, a central cavity, and an intracellular activation gate. The pore (P) helices are situated near the top of the funnel and selectivity filter to help stabilize the Na^+ ions passing through, by means of helical-dipole interactions, as was proposed for K^+ channels (Doyle et al., 1998; Jogini and Roux, 2005). However, a feature not seen in the K^+ channels is that the Na^+ channel contains a second pore helix, called P2, which forms the extracellular funnel of the pore. This was suggested to be a conserved feature of both Na^+ and Ca^{2+} channels (Payandeh et al., 2011).

The crystal structure of an ortholog of the bacterial NaChBac channel was also solved and published in 2012, revealing an asymmetric tetramer and closed, non-conductive selectivity filter. The voltage sensors were in a depolarized conformation, exposing all gating charges to the extracelluar side, and these factors led to the conclusion of the channel being captured in the inactivated conformation. Fast (N-type) inactivation occurs

in these channels, although slow (C-type) also occurs when undergoing prolonged depolarization (Zhang et al., 2012). The NaChBac ortholog channel, NavRh, from an *alphaproteobacterium*, displayed what was thought to be a different state from the previously shown "pre-open" conformation, due in part to the lack of coupling between the voltage sensors and the inner gate. Additionally, the purification and crystallization process takes much longer than the inactivation of the channel, so it was unlikely to have been captured at an intermediary pre-open or pre-inactivated state, and thought to be completely inactivated (Zhang et al., 2012).

The S4 as the voltage sensor

The question of how a voltage-gated channel could sense voltage of the membrane was raised early into their study. Upon this sensing, the channel must undergo conformational changes. In order for the channel to switch from the closed to open state, charged amino acids in the voltage sensor must move within the membrane electric field. The movement, which creates what is known as a gating charge, triggers the pore to open (Armstrong and Bezanilla, 1974). The gating charge is a transient current that is created by the movement of charged amino acids in the S4 segment and precedes the ionic current through the pore. The movements of these charges could be measured. These transient currents can also be separated from the ionic currents, which are much larger (Armstrong and Bezanilla, 1973; Keynes and Rojas, 1974). It was found in voltage-gated K^+ channels that from residue 362 to 377 in the S4 segment, every third residue is positively charged. However, only four of

the five contribute charge to the gating current. These are R362, R365, R368, and R371 (Aggarwal and MacKinnon, 1996; Seoh et al., 1996).

Understanding the gating charges and identifying the region of the protein responsible for voltage sensing was one of the first major steps in studying voltage-dependent activation. Gating and ion conduction were confirmed to be two separate physical processes when mutation in the pore region of the Shaker K^+ channel abolished the ionic current but not the gating current. Much of the information we have today about voltage-gated ion channels in general comes from the study of the Shaker K^+ channel. This is due in part to that pore region mutation (tryptophan at residue 434 mutated to phenylalanine). Upon depolarization, the Shaker channel did not generate a K^+ current, but cut-open oocyte voltage-clamp experiments showed that there were still normal gating currents present (Perozo et al., 1993).

As early as the first Na^+ channel cloning, the positively charged S4 was hypothesized to act as the voltage sensor of the channel (Noda et al., 1984). S4, the fourth transmembrane segment of voltage-gated ion channels, is now known to be the sensor that mediates the protein's response to changes in the membrane's electric field (Aggarwal and MacKinnon, 1996; Seoh et al., 1996). In 1989, a study of the structure-function relationship of the Na^+ channel demonstrated that the positive charges of the S4 segment are involved in the mechanism of sensing voltage.

It is now an accepted model for voltage-gated channels that these positively charged residues in S4 act as the primary sensors of changes in membrane potential (Bezanilla, 2000; Tombola et al., 2005a). Although these S4 residues are important for voltage sensing, the residues in between them have also been found to be critical. Typically, the positive residues are followed by first a high-impact hydrophobic residue, then a low-impact hydrophobic residue. Mutation of a high-impact hydrophobic residue can cause disruptions in protein packing and impair a channel's ability to gate, while the low-impact hydrophobic residues most likely are on the face of the α-helix towards water or lipid (Gandhi and Isacoff, 2002).

To identify a gating charge transfer center within the S4 that facilitates its movement, Tao et. al mutated the S4 residues with natural and unnatural amino acids. Using electrophysiology and X-ray crystallography methods, they showed that two negatively charged amino acids interact with a third positive charge. For that positive charge, mutations could be made so that lysine or arginine were favored (Papazian et al., 1991; Shao and Papazian, 1993; Stefani et al., 1994; Tao et al., 2010).

Models of S4 movement

To account for the gating charges that are displaced during voltage sensing, there have been many purported models to demonstrate the mechanism by which the S4 moves and acts as a voltage sensor. Some models of movement proposed a large degree of translocation by the S4; others are small. An example of a model of large translocation is

the “sliding helix,” also known as “helical screw,” model, which said that the whole S4 travels across the membrane in a spiral, rotating in 60° units, while exchanging ion pair partners along the path. Its positively charged resides would interact with the fixed negative residues along the path it travels, on the other surrounding transmembrane segments. This model was based upon the observation that residues with positively charged side chains form a spiral-shaped ridge down and around the S4 α-helix (Catterall, 1986; Guy and Conti, 1990).

The “paddle model” of voltage gating, like the helical screw model, also incorporates a full translocation of the S4 across the lipid membrane. The term paddle refers to the shape of the helix-hairpin structure of the voltage sensor. This paddle structure contains the four arginine residues responsible for sensing voltage, and the rest of the structure is predominantly hydrophobic. This study also proposed a revision to the conventional nomenclature of the ion channel transmembrane segments, as the S3 was shown to be composed of two individual helices. These were called S3a and S3b by Jiang et. al. S3b and the S4 were shown to be tightly packed with each other. This is the unit that makes up what they called the voltage sensor paddle, each of which from each subunit surround the central pore. As the paddle structure is located on the outer perimeter of the channel, they move across the electric field, carrying their positively charged arginines, during voltage sensing. These movements then are able to couple pore opening to the changes in membrane voltage (Jiang et al., 2003).

Models alternative to the paddle and helical-screw models have also been proposed. For review see Ahern et. al 2004 *Trends Neurosci* and Tombola et al. *Annu. Rev. Cell. Devel. Biol.* 2006 (Ahern and Horn, 2004a; Tombola et al., 2006).

Leaky VSDs and the omega current

The question of S4 movement led to the discovery of the omega current. Mutations in the VSD of voltage-gated Na^+, K^+, and Ca^{2+} channels can occasionally lead to ions leaking through the VSD, resulting in what is known as the omega current. This phenomenon was first observed in the Shaker K^+ channel (Starace and Bezanilla, 2004; Tombola et al., 2005b) and then in Na^+ and Ca^{2+} channels (Sokolov et al. 2005 & 2007, Struyk & Cannon, 2007, Gosselin-Badaroudine et al. 2010, Wu et al. 2012).

Na^+, K^+, and Ca^{2+} channels sense voltage by the movement of arginine residues located in the S4 segment across the membrane's electric field, but there is a need to further understand the mechanism of this molecular pathway. Since there has been debate about the differing models of S4 movement during gating, there has also been a question of whether the arginines of the S4 interact with lipid, or with the rest of the channel. The paddle model had predicted that the S4 arginines interact with lipid, but studies on Shaker and KvAP in 2004 supported the idea that the S4 remains in a polar protein environment (Ahern and Horn, 2004b; Cuello et al., 2004; Starace and Bezanilla, 2004).

If the first arginine of the S4 (abbreviated R1) is substituted with a smaller, uncharged amino acid, there is a conductance pathway opened for solution cations to pass through the ion channel's VSD. This occurs only when the channel is at rest. In Shaker, the R1 is residue 362. A pathway could then be created for monovalent cations. The movement of these cations, independent of the central pore, created a current called the "omega current" which is specific for mutations at the R1. R1 was selected for the site of mutagenesis due to previous studies that showed that mutation of R1 to a histidine supports proton conduction (Starace and Bezanilla, 2004). In the experiments that demonstrated the omega current, the R1 mutations were selected to disfavor the formation of water wires. The mutations to alanine, cysteine, serine, and valine showed the largest inward currents in response to hyperpolarization ($V < -100$ mV). In both the wild-type channel and the R362H channel, this current is not observed. The omega current is observed only when the channel is at rest, putting the position of the R1 deep within the membrane (Tombola et al., 2005b).

There was then the question of which ions are carrying the omega current. Starace et. al demonstrated the existence of a proton current in the Shaker R362H channel in the presence of a proton gradient (Starace and Bezanilla, 2004); however, increasing the concentration of protons in the solutions did not alter the omega current when R362 was mutated to small uncharged residues, which indicated that the current of those mutant channels is not carried by protons. Similarly, it was determined that the current was not due to anions. Replacement of various cations in the bath and pipette solutions also showed that there is a weak selectivity for certain cations. Since the mutation causing the

omega current was the replacement of an arginine with a smaller amino acid, it was hypothesized that this mutation opens up a conduction pathway that could normally be occupied by the arginine side chains. Taken with the results that there is a weak selectivity within cations and selectivity against anions, guanidinium ions were tested in the Shaker R1C mutant. These experiments showed that not only did the guanidinium ions carry a current, this current was larger than that carried by other tested cations (Tombola et al., 2005b).

The results of the omega current studies revealed much insight into the different models of S4 movement. In particular, they agree with an S4 model of movement in which the S4 ratchets between resting, intermediate, and fully activated positions (Lecar et al., 2003), which would put one arginine in the narrowest part of the VSD permeation pathway most of the time. At this narrow portion of the VSD permeation pathway, the strength of the electric field is thought to rise, optimizing the response to changes in the membrane potential. This could also help prevent ion leak in the wild-type channel.

After the discovery of the omega current, it was shown that diseases could actually be caused by channels with leaky VSDs (Sokolov et al., 2007). Included among these is the Na^+ channel mutation previously discussed which causes hyperkalemic periodic paralysis (Matthews et al., 2009; Sokolov et al., 2007). Other channelopathies that could be associated with the omega current are epilepsy, long QT syndrome, and myotonia (Jurkat-Rott et al., 2012).

The pore domain and selectivity

Connected to the VSD of voltage-gated ion channels are the S5 and S6 transmembrane segments making up the pore domain. Pore loops are the extracellular loops that link together the S5 and S6 of each subunit. As these loops reach into the pore, they form what can be considered as the catalytic site of the channel, which acts as the selectivity filter for the permeant ions. The pore domain is formed either by all pore domain segments coming together, as in the Na^+ channel and Ca^{2+} channel, or by a tetrameric structure in which subunits assemble together to create the functioning pore, as in K^+ channel.

The concept of ion selectivity is of great interest to ion channel researchers, since the ability to differentiate between ions and select for their own permeant ion is crucial to the physiological function of ion channels. Much of the earlier work on ion transport and selectivity was based on studies of the K^+ channels, as structural information was available (Doyle et al., 1998). Comparable structural information for Na^+ channels was not available until much more recently, when an atomic resolution crystal structure of the voltage-gated Na^+ channel from the prokaryote *Arcobacter butzleri* (NavAb) was solved in 2011 (Payandeh et al., 2011) and from the *alphaproteobacterium* (NavRh) in 2012 (Zhang et al., 2012).

For high selectivity of cations, the ion channels must remove the ion's hydration shell, then coordinate the selectivity based on the size and charge of the ion. In K^+ channels, Na^+ ions pass through about 17 times less than K^+, although the Na^+ is smaller than the K^+ ion. The

pore of the K^+ channel should be large enough for the Na^+ ion to pass through, but the reason they are restricted is that they are actually too small to fit within the coordination cages in the pore, which act as replacements for the water molecules that are stripped from the passing ion. This concept was first introduced by studying the size of the K^+ pore in squid axons, by evaluating entry of Na^+, Li^+, Cs^+, and tetraethylammonium (TEA^+) ions into the pore (Bezanilla and Armstrong, 1972).

This mechanism of water molecule replacement was studied in the K^+ channel KcsA, whose structure revealed how the channel displaces those water molecules surrounding the K^+ ion. The central cavity of the K^+ channel can therefore hold a K^+ ion surrounded by eight ordered water molecules. While hydrated, the K^+ ion can be transferred from the extracellular solution to the selectivity filter and become dehydrated. The dehydration process is mediated by that specific arrangement of carbonyl oxygen atoms. The dehydration occurs at the channel's extracellular entryway. Once the hydration shell is removed, the waters of hydration are replaced by carbonyl oxygen atoms surrounding the K^+ binding sites. These oxygen atoms mimic the waters of hydration, and are arranged in a ring around the pore. The side chains of Glu71 and Asp80 form carboxyl-carboxylate pairs such that four negative charges are positioned directly at the extracellular pore entryway, providing an electronegative environment, attractive to cations. (Zhou et al., 2001).

It was also found that the selectivity filter can exist in two different conformations. The equilibrium between these conformations is dependent on the concentration of K^+ ions. The selectivity filter can be arranged such that it is non-conductive if the K^+ ion

concentration is low enough so that the filter loses one of its ions. Conversely, at high K^+ ion concentrations, the filter's conformation is made to be conductive.

In 1994, a partial sequence alignment was performed comparing the P-region of all cloned K^+ channels available at that time. This revealed that all examined channels contained a homologous sequence over eight amino acids (TXXTXGYG). This was termed the signature sequence for K^+ selectivity. It was then inferred that this signature sequence could be forming the catalytic domain responsible for the common conduction properties that exist in K^+ channels (Heginbotham et al., 1994). Although K^+ channels can be activated in a variety of ways, be it by voltage, Ca^{2+}, or ligand-binding (Hille, 2001), the actual mechanism of ion conduction appears to be the same in all. This signature sequence underlies the common mechanism of ion conduction in these K^+ channels.

A feature that appears to be unique to the K^+ channel is the central cavity, a point in the conduction pore that dilates to about 10 Å at the intracellular side of the selectivity filter, halfway across the membrane. The central cavity is thought to be the channel's way of solving the problem of the dielectric barrier. The low-dielectric membrane would repel cations, but with the central cavity, the channel can keep K^+ in a watery, high-dielectric environment (Zhou et al., 2001).

Following the first publication of an atomic structure of a Na^+ channel, new insights into ion selectivity have been shown. The energetics of ion permeation were modeled using the NavAb structure, which revealed a multi-ion conduction mechanism that actually differs

from that of K^+ channels. In Na^+ channels, the conduction mechanism involves the independent movement of solvated ions. Selectivity of Na^+ over K^+ is achieved by the chemical makeup of the pore lining and the size of the pore along the plane of four glutamate residues' side chains (Glu177). This plane of the Glu177 residues is located at the external end of the selectivity filter. The existence of a second P-region helix also was shown in the crystal structure, revealing P1 at the selectivity filter, deeper into the pore of channel, and P2 nearer to the extracellular funnel (Payandeh et al., 2011).

1.2 Voltage-sensitive proteins without a pore domain

Previous notions of the relationship between the VSD and the pore domain

Until the discovery of non-ion channel VSD-containing proteins, it was thought that VSDs could only function as controllers of effector pore domains. Now, it is known that the family of VSD-containing proteins also includes proteins whose VSDs perform functions outside of controlling ion conduction through a pore domain. Notable examples of VSD-containing proteins that do not have a pore domain are the voltage-sensitive phosphatase *Ciona intestinalis* VSP (Ci-VSP) and the voltage-gated proton channel Hv1.

Discovery of proteins that have a VSD attached to structures that are not a pore domain

Ci-VSP discovery

In 2005, a gene was discovered during a genomic survey of the ascidian *Ciona intestinalis* that contains domains homologous to both an ion channel and a phosphatase. This gene codes for a protein with a transmembrane domain homologous to the S1 through S4 segments of voltage-gated ion channels. The cytoplasmic domain, rather than the S5 and S6 transmembrane segments making up the pore domain of voltage-gated ion channels, is an enzymatic domain similar to phosphatase, tensin homolog, deleted on chromosome ten (PTEN). It was called *Ciona intestinalis* voltage-sensor-containing phosphatase protein (VSP), and its discovery was the first example demonstrating that VSD domains could be found in non-channel proteins. In CiVSP, the VSD senses voltage to control the enzymatic domain in its C-terminus, rather than opening a pore domain to conduct ions (Murata et al., 2005).

When the transmembrane domain of CiVSP was tested for voltage sensitivity by expression in *Xenopus* oocytes, a mechanism similar to that of ion channels was recorded – outward currents in response to depolarization and inward currents in response to hyperpolarization. This is the characteristic gating current that was shown in voltage-dependent ion channels. In the case of CiVSP, the voltage-dependence of charge movement was shifted positively to that of the Shaker K^+ channel (Murata et al., 2005).

As it is not a channel, this protein responds to membrane depolarization by dephosphorylating phosphatidylinositol (PI) lipids, thus regulating the levels of PI lipids (Murata et al., 2005). Prior to this discovery, voltage sensor-effector coupling had only been known in the context of one pore cooperatively gated by four VSDs. Combined with the fact that PTEN is a monomer, it was important to investigate whether Ci-VSP also exists as a monomer. In 2008, total internal reflection fluorescence (TIRF) microscopy and voltage-clamp fluorometry (VCF) revealed that Ci-VSP does indeed function as a monomer (Kohout et al., 2008).

The phosphate domain of VSPs can be thought of as indirectly regulating processes that depend on phospholipids, because it acts by removing phosphate groups from phospholipids. Their primary function is to degrade the major signaling phospholipids $PI(4,5)P_2$ and $PI(3,4,5)P_3$ (Halaszovich et al., 2009). This enzyme activity was shown to be activated upon depolarization (Murata and Okamura, 2007).

TPTE and TPTE2, and their relationship to PTEN

VSPs share structural similarities with the tumor suppressor lipid phosphatase PTEN. Its phosphatase domain is highly homologous to the PTEN protein. The phosphatase domain of VSPs removes phosphate groups from phospholipids but PTEN, discovered in 1997, has dual lipid and protein phosphatase functions. It was initially discovered by mapping

homozygous deletions on the human chromosome 10q23.3 (Li et al., 1997; Steck et al., 1997).

TPTEs (transmembrane phosphatase with tensin homology) are the human homolog of CiVSP. The TPTE gene sequences were found to be conserved in different species, including Rhesus monkey, rat, cow, and rabbit (Chen et al., 1999). TPTE was found to be testis-specific in both human and mouse (Chen et al., 1999; Wu et al., 2001). In human, there were two homologs of CiVSP found, called TPTE and TPTE2 (also called TPIP) (Tapparel et al., 2003; Walker et al., 2001). TPTE showed the same architecture as CiVSP, but did not show phosphatase activity (Leslie et al., 2007). TPTE2, however, did show phosphoinositide phosphatase activity *in vitro* and so it is proposed to be the true ortholog of CiVSP in mammals (Walker et al., 2001). After this discovery, it was proposed in 2012 to rename TPTE2 to hVSP1 and TPTE to hVSP2 (Halaszovich et al., 2012).

Diseases associated with VSPs and related proteins

PTEN is capable of dephosphorylating tyrosine and serine/threonine residues in protein as well as phosphoinositides. PTEN acts as a tumor suppressor by keeping cellular phosphatidylinositol-(3,4,5)-triphosphate (PIP3) at low levels. PIP3 is a second messenger molecule important to cell growth signaling (Maehama and Dixon, 1998). PTEN was discovered to be inactivated in many human cancers, notably prostate cancer (Li et al., 1997). Additionally, somatic mutations of the *Pten* gene has been seen in tumors such as glioblastoma, breast carcinoma, endometrial carcinoma, thyroid neoplasms, and skin

neoplasms (Shroff et al., 2013). The loss of the *Pten* gene was linked to the initiation and progression of refractory prostate cancer. This marked the PTEN protein as a therapeutic target for the treatment of prostate cancer (Uzoh et al., 2009). Besides having a role as a tumor suppressor, PTEN also plays important roles in embryogenesis and the maintenance of physiological functions of many organ systems (Knobbe et al., 2008).

Hv1

Structure and function of Hv1

Hv1, also known as HVCN1 or VSOP (Voltage Sensor Only Protein), is another example of a class of proteins with a VSD, but no pore domain. A description of the activity by what would later be known as voltage-gated proton channels first appeared in 1972 by Fogel et. al who, in a study of dinoflagellates, proposed that proton movement must occur through an imposed pH gradient, and that the cell membrane controls this movement in response to cellular excitability (Fogel and Hastings, 1972). Ten years later, proton currents were first recorded in snail neurons. Voltage-clamp was performed on snail neurons to make pH measurements, which provided evidence of a large increase in H^+ ion permeability in depolarized cells (Thomas and Meech, 1982). However, it was not until 2006 that the channel was identified at the molecular level. Hv1 is the first of its family of voltage-gated proton channels to be cloned (Ramsey et al., 2006; Sasaki et al., 2006), identified in mice (the murine homolog of Hv1 is mVSOP) in 2006 by using the amino acid sequence of the VSD of Ci-VSP as a protein database search query (Sasaki et al., 2006). Notably, this protein

is made up of four transmembrane segments that are homologous to the VSD, but does not have any structure homologous to the pore domains of voltage-gated ion channels. The human homolog to mVSOP, named Hv1, was identified in 2006 as well (Ramsey et al., 2006). Hv1 was found to be expressed in macrophages, neutrophils, eosinophils, and other immune cells.

This protein is a channel, and permeates protons, but does not have a separate pore domain. When Hv1 was initially sequenced, it was unclear how it worked as a functional channel without the pore domain seen in other channels. Based on those initial studies, it was suggested that Hv1 functions as a single VSD, with a pore pathway somewhere within that VSD.

The same structure serves as both the VSD and the pore domain. Here, the VSD is connected to a cytoplasmic coiled-coil domain rather than the pore domain, as in voltage-gated Na^+, K^+, and Ca^{2+} channels. Hv1 is gated by voltage, it opens in response to membrane depolarization and conducts measurable outward proton current that produces membrane repolarization.

Dimerization of Hv1

In channels with distinct pore domains, the ion permeation pathway is located at the interface of multiple subunits. As a result, oligomerization of the pore domain is required for channel function. Since Hv1 and VSOP were found to lack the pore domain, their VSD

was initially assumed to work as a monomer and to serve both as a voltage sensor and proton-conducting pore. However, later studies provided strong evidence for Hv1 functioning as a dimer.

Tombola et. al determined the number of subunits by using the single-molecule technique of subunit counting (Tombola et al., 2008). This method tags the subunit with GFP, ensuring that every subunit is labeled with one and only one GFP, thus eliminating the problem of nonspecific labeling that could occur with dyes. The photobleaching of the GFP attached is a discrete observable process such that the fluorescence intensity of a protein complex drops in a stepwise manner, depending on the number of subunits. The number of steps of decreasing fluorescence is correlated to the number of GFP-tagged subunits within a complex (Ulbrich and Isacoff, 2007). Tombola et. al found by using this method that Hv1 showed two bleaching steps, and therefore two subunits. The observations made were also similar to other known channels with two subunits (Tombola et al., 2008).

However, having two subunits does not necessarily mean two pores, so the number of pores in the functional channel was next investigated. A mutation screen was performed to find residues that, when substituted with a cysteine, block the proton current with the addition of the MTSET reagent, which is a thiol-modifying reagent, covalently adding a group with a positive charge to accessible cysteines. Wild-type Hv1 channels are not sensitive to MTSET at all. A substitution at N214C did create an Hv1 channel whose proton current was almost completely inhibited by MTSET. The residual proton current upon this inhibition was voltage-dependent as the normal current, which was consistent with the

idea that inhibition of Hv1 by MTSET was due to pore block. With the knowledge of a dimer structure, tandem dimers were constructed in which the C-terminus of one Hv1 subunit was linked to the N-terminus of another. If neither of those subunits were altered, this tandem dimer was called WT-WT. Other constructs had a N214C mutation in the first or in the second subunit, or in both. Under the assumption that each Hv1 subunit had its own pore, it was expected that the reduction of current observed in linked dimers with only one N214C subunit (N214C-WT and WT-N214C) would be ~50% of the reduction observed with N214C-N214C linked dimers. On the other hand, assuming that that both subunits were required to come together and form a central pore, a near complete block would be expected in all dimers that contained at least one N214C mutation. The results from these experiments supported the two-pore model of Hv1 (Tombola et al., 2008).

Another group, Lee et. al, found evidence that Hv1 is a dimer through crosslinking experiments. Disuccinimidyl suberate (DSS) was the crosslinking agent used, and it works by reacting with primary amines that happen to be in close proximity, forming stable amide bonds. Wild-type Hv1 and a mutant with cysteines removed both showed DSS-mediated crosslinking patterns, revealing a dimer band when the proteins were visualized with Western blots. It was found through these studies that the two voltage sensor protomers of the dimer directly come into contact with each other, at both the extracellular and intracellular sides of the membrane (Lee et al., 2008).

A third piece of evidence for Hv1 functioning as a dimer came from immunoprecipitation techniques and FRET (fluorescence or Forster resonance energy transfer) experiments by

Koch et. al. HA-tagged (human influenza hemagglutinin, a general epitope protein tag) and Myc-tagged mouse Hv1 constructs were co-expressed into tsA201 cells and then immunoprecipitated (an epitope tag for affinity studies) using anti-HA or anti-Myc antibodies. Both HA-tagged and Myc-tagged Hv1 subunits were immunoprecipitated by using either of the antibodies, showing that Hv1 forms multimers containing both tagged subunits. Hv1 was also tagged with fluorophoes to examine whether the individually tagged subunits were in close enough proximity to undergo FRET. FRET was used to measure the distance between the subunits of CiVSOP (another name for CiHv1). Mutant channels with an introduced cysteine were expressed into *Xenopus* oocytes and labeled with a fluorescent dye and subsequently also with a donor dye. These experiments suggested that Hv1 is a multimeric protein since a substantial fraction of energy absorbed by the donor fluorophores was transferred to acceptor fluorophores (Koch et al., 2008).

The studies from the previously mentioned groups also sought to find which region of the Hv1 protein was responsible for dimerization. As a protein closely related to Hv1, CiVSP was used as a reference. It was previously shown that CiVSP functions as a monomer (Kohout et al., 2008), and thus it was reasoned that by creating chimeric proteins of Hv1 and the monomeric CiVSP, it would be possible to determine which parts of Hv1 are responsible for dimerization. Substituting the N-terminus of Hv1 with that of either Ci-VSP or Shaker Kv1 compromised the protein's ability to dimerize, and substituting the C-terminus prevented dimerization completely, strongly suggesting that the C-terminus is responsible for the dimerization of the channel. Using these constructs, it was also discovered that Hv1 is able to function as a monomer (Tombola et al., 2008). Removal of

the C-terminus was also performed by Koch et. al, whose evidence also supported the finding that Hv1 can function as a monomer (Koch et al., 2008).

Hv1 cooperative gating

After experimental evidence showed that Hv1 can work as a monomer, the functional purpose of dimerization came into question. Investigations of the voltage dependence of monomeric and dimeric Hv1 channels bearing different mutations at one or two subunits lead to the conclusion that the two Hv1 subunits of open cooperatively in the dimer, wherein the opening of one subunit substantially increases the likelihood of the other subunit opening (Tombola et al., 2010).

Another question about the mechanism of gating of Hv1 that needed to be answered was whether the S4 helix is the voltage sensor of this channel. To show whether or not the S4 moves across the membrane electric field during activation, as it would if it were the voltage sensor, the solvent accessibility of introduced cysteines in and around the S4 helix were tested, using CiHv1/VSOP. Using these cysteine accessibility experiments and voltage-clamp fluorometry, changes in the modification of those cysteines were measured in the open and closed states. This determined whether some of these residues were moving between the open and closed states. In CiHv1, there was lack of proton current upon application of MTSET in certain cysteine-introduced mutants. N264C and I262C channels showed an abolished proton current, and internal MTSET modified these channels faster at hyperpolarized potentials than at depolarized potentials. This suggested that both of those

residues become inaccessible when the channel is open. These accessibility experiments showed that during activation, the positive S4 charges do move outward relative to the membrane electric field. In the dimeric Hv1 channel, both S4 segments of each subunit must move in order to activate the two proton pore pathways. This work provided strong evidence for the S4 moving and acting as the voltage sensor of Hv1 (Gonzalez et al., 2010).

Following the discovery that the gating movement of one Hv1 subunit influences the other in the dimer, it was still unclear where exactly the conformational change that is transmitted from one subunit to the other was occurring. Oligomer formation had been studied to find the dimer interfaces in Hv1, and two candidates were found. One interface was proposed to be mediated by the S1 and a nearby extracellular loop. The other was proposed to be mediated by a predicted intracellular coiled-coil domain (Lee et al., 2008).

The first descriptions of the coiled-coil came about in 1953 (Crick, 1953; PAULING and COREY, 1953), identifying it as the main structural feature of a class of fibrous proteins such as keratin, myosin, and fibrinogen. A coiled-coil is essentially a bundle of α-helices wound into a superhelix. A distinguishing feature of the coiled-coil is the packing of amino acid side chains into the core of that bundle, where a residue from one helix will pack into the space created by four side chains of a facing helix (Lupas, 1996).

Conventional nomenclature for coiled-coil structures names the positions in the heptad repeat of the structure *a* through *g* (Fig. 1.2). The key residues of the interface are at positions *c* and *f*. In an ideal situation, the *a* through *g* heptad motif is repeated and

positions *a* and *d* comprise the hydrophobic core of the two helix bundles (Lupas, 1996).

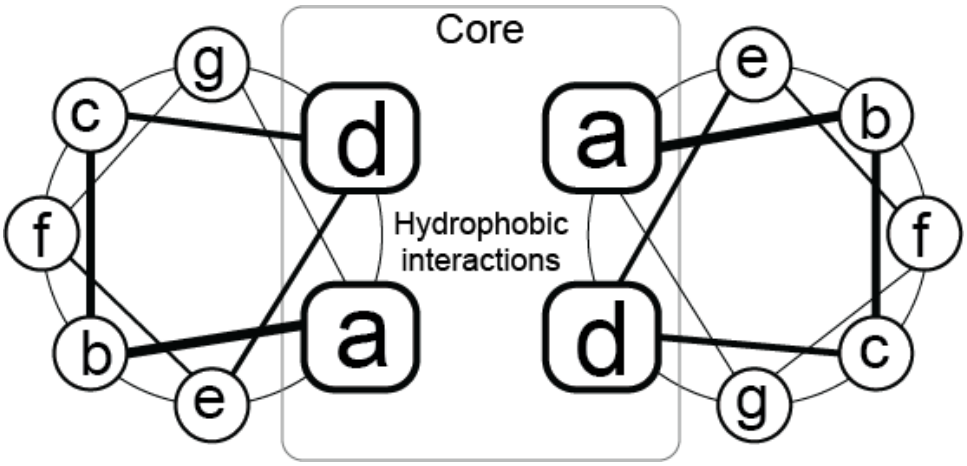

Figure 1.2. A top-down representation of the heptad repeat residues of the coiled-coil domain. Thicker lines represent regions closer to the top.

In 2010, an atomic crystal structure of the C-terminal domain of Hv1 was published, which revealed a dimer made of two parallel, coiled α-helices. Following the conventional coiled-coil domain nomenclature, the key residues involved in complementary hydrophobic and polar interactions in the hydrophobic core are at positions *c* and *f*, which are typically positions *a* and *d* in other coiled-coil structures. It also was suggested that local charge compensation may be occurring at heptad repeat positions *b* and *g* by charged side chains and polar residues. Notably, asparagine, histidine, and cysteine are usually very rare at heptad repeat positions *c* and *f*, in coiled-coil structures of other proteins. Most of the time, hydrophobic residues have been found at those positions (Li et al., 2010).

A pH-dependent structural change of the Hv1 C-terminus was observed, although the dimerization of Hv1 was unaffected by pH. Crosslinking assays were performed to verify that the C-terminal cytoplasmic domain is what is required for the Hv1 dimer (Li et al., 2010). More recently, the crystal structure of the coiled-coil domain from mouse Hv1 was also solved (Fujiwara et al., 2012) and compared to that of the human Hv1 (Li et al., 2010). In the mouse Hv1, the *a* and *d* positions, at the hydrophobic core of the coiled-coil domain, were found to be isoleucine, asparagine, cysteine, and leucine. This work in crystallizing the coiled-coil domain of mouse Hv1 investigated how dimerization is related to the gating of Hv1. It was found that both dimerization and cooperative gating are mediated by the cytoplasmic coiled-coil domain. Without the C-terminal coiled-coil domain, Hv1's activation kinetics are accelerated, showing that activation is regulated by the coiled-coil assembly. It was additionally shown that this regulation occurs in a temperature-dependent manner. The increase in H^+ conduction by depolarization appeared to be optimal in the range of body temperature. This temperature-dependent activation of current through the Hv1 channel was shown to be regulated by the thermostability of the coiled-coil domain. Wild-type channels showed a higher thermostability than channels with the C-terminus removed. Finally, it was shown that the linker between the S4 and the C-terminal coiled-coil domain is important for mediation of cooperative gating (Fujiwara et al., 2012).

Although the C-terminus is now known to be responsible for dimerization, it had also been implicated in localization function. As a membrane protein, the full-length Hv1 protein is mostly localized to the membranes of intracellular compartments, and less so to the plasma membrane. Experiments in which the N- and C-terminus were either truncated alone or

together showed that N terminal deletion did not affect localization, whereas truncation of the C-terminus did. Truncation of the C-terminus either alone or with the N-terminus led to Hv1 expression throughout intracellular membranes rather than the plasma membrane of the cell (Li et al., 2010).

Recently, an x-ray crystal structure for the mouse Hv1 was solved to a 3.45 Å resolution. Significantly, the structure was concluded to be in the resting state, while all other available crystal structures of voltage-gated channels are in the activated state. Several pieces of evidence supported this conclusion. . First, a Zn^{2+} molecule was found bound to the channel. Zn^{2+} is a known inhibitor of Hv1, and acts as a gating modifier. Two histidines, His136 and His189, were found in the structure at positions close enough to coordinate the Zn^{2+}. The corresponding residues in human were previously shown to be involved in Zn^{2+} coordination (Musset et al., 2010; Ramsey et al., 2006). Two negatively charged residues were also found near the Zn^{2+}, Glu115 and Asp119. These residues are highly conserved across Hv1s from different species (Glu119 and Asp123 in human). To investigate whether these residues were necessary for the coordination of the Zn^{2+}, they were mutated to serine, and electrophysiology experiments showed that when one residue was mutated, the channel was still sensitive to Zn^{2+} and current was inhibited. However, a double mutation did show a lack of Zn^{2+} sensitivity, indicating that the presence of at one of either Glu115 or Asp119 is sufficient for the coordination of the Zn^{2+} ion, but the loss of both residues preserved the inhibition by Zn^{2+}. The mechanism by which Zn^{2+} is able to inhibit Hv1 appears to be its interaction with these Glu115 and Asp119 residues, thereby preventing

them from interacting with the positively charged arginines of the S4. This, then, prevents the activation of Hv1 (Takeshita et al., 2014).

Second, the position of the arginines of S4, which function as the voltage sensor of the channel, was compared to that of other voltage-gated channel structures, Kv1.2, KvAP, and NaChRh. A phenylalanine residue conserved across all of these proteins was used as a reference point, as it is known to be a charge-transfer center. Hv1 contains three arginines in the S4 while the others contain four, and the sequence alignment was performed aligning the first arginine of Hv1 (R1) to the second arginine of the other channels. The other crystal structures deemed to be in the active state showed that these voltage-sensor residues were located above the phenylalanine reference, whereas two of the three where located below. One caveat to this is that the chimerization of the Hv1 channel necessary for crystallization may have been artificially lowering the S4 slightly, due to the fact that the reference point phenylalanine is next to a chimeric region, which was a sequence from CiVSP. These results were, however, consistent with data that mapped the S4 position using MTS-reagent accessibility experiments (Gonzalez et al., 2010; 2013; Kurokawa and Okamura, 2014). This newly solved crystal structure does suggest that the binding of Zn^{2+} and other metal ions to Hv1, thereby competing for binding with the residues that interact with the S4, stops the S4 from moving. This could represent a mechanism used by cells to regulate the activity of channels by use of ions such as Zn^{2+}, and as a possible regulatory mechanism, it could be one that is found in other voltage-gated channels as well (Takeshita et al., 2014).

Hv1 molecular function

Hv1 is exclusively selective for protons over other ions (Decoursey, 2003). Though it is voltage-gated, it only opens in a highly pH gradient-dependent manner. Hv1 gating is dependent on the pH of both the extracellular and intracellular sides (Okamura, 2007), as well as exhibiting a strong temperature dependence of conduction and gating (DeCoursey and Cherny, 1998). It is activated by membrane depolarization and intracellular acidification. The threshold of activation becomes less positive as delta pH (extracellular pH – intracellular pH) becomes larger. The channel also opens only when the electrochemical gradient is outward. These are features that allows Hv1 to permeate protons outwardly only (Okamura, 2007).

There are several differences between the activity of Hv1 and other voltage-gated channels. Hv1 does not exhibit a measurable gating current. It has not yet been experimentally determined whether this is due to slow kinetics of activation, or whether there are no gating currents to be measured. However, recordings performed using Hv1 orthologs with faster activation kinetics also showed no gating current (Okamura, 2007). The permeation of ions through Hv1 has been proposed to share some common features with the nonselective omega current. Even though the omega current is induced during hyperpolarization rather than depolarization as in the Hv1 channel (Tombola et al., 2005b), it was thought that a similar pathway for proton permeation would exist in the open state of the Hv1 channel. Since amino acid substitutions of one or more S4 arginines of K^+ and Na^+ channels resulted in the omega pore effect, the participation of S4 arginines in proton

permeation in the Hv1 channel was investigated. It was found that mutation of the third arginine (R3) in the Hv1 S4 compromised its ability to be selective for H^+. It resulted in the ability to conduct metal cations, and the large organic cation guanidinium (Berger and Isacoff, 2011), similarly to what was seen in Shaker's omega pore (Tombola et al., 2005b). Furthermore, mutation of both the R1 and R2 compromised cation selectivity even more. These experiments showed that H^+ and guanidinium ions were permeating the same pathway by use of Zn^{2+} inhibition. Since Zn^{2+} inhibited the current carried by guanidinium in the R3S mutant as it does the proton current in wild type Hv1, it was supported that the R3S mutation was allowing guanidinium through the same pathway as H^+. In these experiments, it appeared that the R3 was interacting with a residue that is unique to Hv channels, the aspartate at position 112 (D112). Together, the R3 and D112 were proposed to form the selectivity filter for the Hv1 channel, at the narrowest part of the Hv1 pore. Gating of this pore was proposed to involve the formation of this selectivity filter, as the movement of S4 upon membrane depolarization brings R3 in close proximity of D112 (Berger and Isacoff, 2011).

The aspartate at residue 112 was shown to be critical for proton selectivity in Hv1 by the DeCoursey group. Mutating this residue to a neutral amino acid was found to cause loss of proton specificity. Channel mutant at position 112 were found to be anion-selective or completely non-conducting. The closest other aspartate at residue 185 did not cause such impairment to the function of Hv1, indicating that that contribution of D112 to proton selectivity is unique (Musset et al., 2011).

The precise location of the activation gate within the voltage-sensing domain of Hv1 is not known. However, it was reasoned that, as the only transmembrane segment of Hv1, the VSD must contain the pore when studies showed that the protein could retain functionality when its coiled-coil domain was replaced or otherwise disrupted (Koch et al., 2008; Tombola et al., 2008). Additionally, it was shown that as a dimer, the individual pores of the Hv1 subunits could be blocked by site-specific attachment of cysteine-reactive probes (Tombola et al., 2008).

Physiological roles of Hv1

Hv1 is coexpressed on phagosomes with NADPH oxidase (NOX) subunits, and has a role in the production of reactive oxygen species (ROS) by neutrophils during the oxidative burst, which is involved in pathogen elimination. Hv1 is able to help maintain the NADPH oxidase activity by charge compensation and pH regulation (Okochi et al., 2009). Other roles of Hv1 include sperm cell capacitation (Capasso et al., 2011; Lishko and Kirichok, 2010), the activation and proliferation of B lymphocytes by initiating antigen response (Capasso et al., 2010), the regulation of intracellular pH in airway epithelia (Iovannisci et al., 2010), and histamine release by basophils (Musset et al., 2008). Hv1's role of proton extrusion during the respiratory burst has been well studied in in granulocytes and monocytes.

The role of Hv1 in the production of high-level superoxide by phagocytes was studied using Hv1 knockout mice (Chemaly et al., 2010; Okochi et al., 2009; Ramsey et al., 2009). These mice, though lacking the Hv1, still had the fully functioning oxidase. The knockout mice

were used to investigate the function of Hv1 in neutrophils. These studies showed that the oxidase does not function as a proton channel, since there was a lack of proton currents in the oxidase although they were still able to produce normal electron currents. Therefore, it was proposed that Hv1 interacts with some component of the oxidase complex assembling at the membrane, being in close association with the oxidase. It was also shown that Hv1 helps maintain a normal cytosolic pH and membrane potential during respiratory burst. Hv1-deficient neutrophils were defective in killing bacteria, due to decreased production of superoxide. However, the decreased ability to kill bacteria could also have been due to other factors – the altered pH homeostasis or altered Ca^{2+} that occurred as a result of the Hv1 deletion. It is therefore suggested that the loss of Hv1 results in multiple perturbations leading to the inability of the neutrophils to kill bacteria (Chemaly et al., 2010).

ROS are small molecules that are chemically reactive, and contain oxygen. The generation of ROS is typically begun with the production of superoxide, and this continues with a cascade of reactions. The ROS react with a number of different molecules, and can thus lead to alteration or even destruction of these molecules. However, the ROS do have a beneficial role in host defense (Bedard and Krause, 2007), and are involved in many signaling pathways. For example, ROS are involved in the regulation of cell homeostasis (Ray et al., 2012).

NADPH oxidase (NOX) activity leads to membrane depolarization and intracellular proton accumulation. Hv1 allows NOX activity to be sustained by re-polarizing the membrane,

preventing the membrane potential from becoming too positive, and extruding excess protons from the cell (Decoursey, 2003).

Microglial cells express many different kinds of ion channels, and changing the functional state of the cell can cause a change in the expression levels of those channels. In the central nervous system, there are significant changes in extracellular pH under a normally functioning brain, although large pH changes can also occur in pathological conditions such as ischemia and epilepsy. At the onset of normal neuronal activity, a rapid extracellular alkalinization occurs. (Eder and DeCoursey, 2001).

Hv1's roles in the sperm cell are involved with motility, capacitation, and the acrosome reaction (in which the cap-like structure over the sperm is fused to the egg), all vital to the sperm cell's ability to reach and fertilize the egg. The motility of sperm is in part regulated by the Hv1 channel. The intratesticular environment is known to be high in Zn^{2+}, as it is an environment where sperm motility is not necessary. Once the sperm is in the environment of the epididymis or vagina, the low Zn^{2+} concentrations activate motility. In human spermatozoa, Hv1 channels are colocalized with another pH-dependent channel, the Ca^{2+} channel CatSper (Kirichok et al., 2006). As the Hv1 channel extrudes protons, the CatSper channel becomes strongly potentiated by intracellular alkalinization. Therefore, the activity of Hv1 induces activity of CatSper channels. The activity of both channels is necessary for the regulation of human spermatozoa and fertilization. Interestingly, this is not seen in all mammals. The Hv1 current is not present in mouse spermatozoa, and Hv1 knockout mice are still fertile (Lishko and Kirichok, 2010). The study of Hv1 function in human

spermatozoa may therefore provide insight into the mechanism of human fertilization specifically.

Inhibition of Hv1

The inhibition of Hv1 currents by micromolar concentrations of Zn^{2+} was first shown in 1989 by using two-electrode voltage clamp on snail neurons. These studies also found that Zn^{2+} inhibited Ca^{2+} currents, but a higher concentration was required (Mahaut-Smith, 1989). Other divalent cations such as Cd^{2+} were also shown to inhibit the Hv1 proton current (Cherny and DeCoursey, 1999). After the cloning of Hv1, electrophysiology experiments were done with Zn^{2+} and the proton current inhibition was found to be rapid and reversible, when the Zn^{2+} was applied to the bath solution during measurements of whole-cell currents in transfected HEK cells. Residues that were putatively determined to be accessible to the extracellular solution were mutated to determine whether they may coordinate metal ions during this inhibition. These mutation studies showed that Zn^{2+} binds to histidine residues in Hv1. The mutation of H193 or H140 to alanine decreased Hv1's sensitivity to Zn^{2+}, but the combined mutation of both nearly eliminated the Zn^{2+} sensitivity altogether. In all three conditions, these mutants were able to display the same selectivity for H^+ and internal and external pH dependence as in the wild-type Hv1 channel (Ramsey et al., 2006).

Based upon these studies, it could be hypothesized that Zn^{2+} is able to inhibit the Hv1 proton current by binding to both H193 and H140. However, further studies on Zn^{2+}

inhibition of Hv1 were performed after analyzing a homology model of the Hv1 structure. This model revealed that in the Hv1 protein, these two histidines are about 14 Å apart, which is far too large of a distance for these residues to be coordinating a single Zn^{2+} atom within their electron orbitals (Musset et al., 2010). Previous studies of Zn^{2+} binding sites show that the binding distances between Zn^{2+} and their coordinating atoms in other proteins are between 1.9 – 2.4 Å (Alberts et al., 1998). To conform to both these findings, it was hypothesized that Zn^{2+} could be binding Hv1 at the interface between two monomers, since Hv1 functions as a dimer. The binding could be to the complementary histidine residues between different subunits. Modeling of the dimer showed that both pairs of histidines could form viable Zn^{2+} binding sites, which also takes into account that the binding of the Zn^{2+} atom would pull the histidines closer together. Further mutation studies were performed following the modeling analysis in order to better understand the Zn^{2+} binding sites. Since the Zn^{2+} was thought to bind to the Hv1 as a dimer, a method for testing this hypothesis was to express the Hv1 channel as a monomer and examine Zn^{2+} binding and inhibition there. These studies found that Zn^{2+} sensitivity in the monomeric Hv1 channel was weaker than in the wild-type dimer (Musset et al., 2010) but not completely abolished. In the recent Hv1 crystal structure, the Zn^{2+} was found bound within the VSD structure (Takeshita et al., 2014).

Hv1 and disease

The study of block in the Hv1 channel and the mechanism of inhibition of its proton current are especially pertinent when considering Hv1's roles in a variety of diseases. An

interesting association that Hv1 has with disease is its involvement with the generation of ROS. ROS are generated as a part of innate immunity, but this pathway can also be induced by ischemia (Wu et al., 2012). Ischemic stroke is the most common form of stroke, affecting about 88% of all stroke victims. Brain damage is caused by activation of the ischemic cascade, which prevents the production of high-energy phosphate compounds such as adenosine triphosphate (ATP) due to a lack of oxygen and glucose. This chain of events adversely affects the energy-dependent processes that are necessary for cell survival. Such downstream effects include the depletion of cellular energy store resulting from mitochondria failure, loss of membrane ion pump function leading to a dysregulated ion gradient, and release of excitatory neurotransmitters. Glutamate, necessary for neural plasticity, is released uncontrollably during ischemia, thereby resulting in neurotoxicity by over-activating a variety of enzyme systems (Deb et al., 2010).

The excessive activity of Hv1 was recently shown to exacerbate the recovery from ischemic stroke. NADPH oxidase (NOX), a membrane-bound enzyme, is now known to be a source of oxidative stress in the brain. It is largely expressed in phagocytic cells such as microglia. NOX-mediated ROS production has a role in defense against pathogens, but can also cause damage to cells such as neurons and glia does occur as a result of its activity (Bedard and Krause, 2007). Hv1 is required for the NOX-dependent generation of ROS in brain microglia, so mice lacking Hv1 were used in a study to examine NOX-mediated neuronal death and brain damage. Hv1 was shown to support NOX activity and blocking Hv1 lessened brain damage after stroke. Microglial Hv1 was shown to be necessary for NOX-dependent generation of ROS *in vitro* and *in vivo*, since the rapid export of positively

charged H^+ by Hv1 is needed by the NOX to transport electrons during ROS production. In microglia, Hv1 contributed substantially to this ROS production, leading to NOX-mediated neuronal cell death. This rate of cell death was higher in wild-type microglia as compared to Hv1-deficient microglia. In other brain cells tested, the hippocampal and cortical neurons, no voltage-gated proton currents were found. In these cells, NMDA induced a similar rate of cell death in both wild type and Hv1-deficient mice, which suggests that the glutamate neurotoxicity discussed earlier is likely not contributing to Hv1's effects on brain damage (Wu et al., 2012).

The options for treatment of ischemic stroke are limited. The inhibition of NOX has been considered, but this may not be a viable strategy since the results were not promising in recent studies (Moskowitz et al., 2010). Alternatively, the inhibition of Hv1 may be a much more promising strategy for ischemic stroke therapy based upon this recent work. The reduction of Hv1 activity by use of Hv1-targeted inhibitors could hasten the recovery from ischemic stroke in patients, particularly in its early stages. The work by Wu et. al clearly showed that Hv1 in microglia support brain damage that is mediated by NOX in early stages of ischemic stroke. Additionally, Hv1-deficient mice were protected from NOX-mediated neuronal death and brain damage, when examined 24 hours after stroke (Wu et al., 2012). Based upon this, therapy designed for patients of ischemic stroke would likely be most effective in the first 24 hours after stroke. If the activity of Hv1 could be inhibited at this early stage, brain damage could be lessened or prevented in patients of ischemic stroke.

Hv1 and cancer

Hv1's role of mediating NADPH oxidase function may lead to its overexpression in certain tumor tissues and cell lines. There is a growing body of evidence to suggest that hypoxia and acidity are associated with cancer progression, as well as affecting the tumor sensitivity to chemotherapy (Fais et al., 2007). Tumor cells are often found living in hypoxic microenvironments, with high glycolytic activity. These cells will also produce acidic metabolities. These factors contribute to an excessive production of intracellular acidity. Due to this drastically changed intracellular pH, tumor cells have to adapt a much more dynamic cytosolic pH regulation system than in normal cells (Wang et al., 2012).

Hv1 is expressed in metastatic human breast tissues and cell lines, with high levels of expression in highly metastatic tissues such as in the MDA-MB-231 cell line, which has high metastatic potential. However, Hv1 is expressed at low levels in poorly metastatic breast tissues and cell lines, such as the MCF-7 and T-47D cell lines (Wang et al., 2011). The metastatic potential of human breast cancer cell lines has been previously described (Sennoune et al., 2004). By inhibiting the expression of Hv1 mRNA in highly metastatic human breast cancer cells, the invasion and migration of those cells was greatly lowered. These studies also showed that Hv1 regulates intracellular pH in breast cancer, and contributes to the migratory ability of metastatic cells (Wang et al., 2011).

Studies inhibiting the function of Hv1 were able to slow the growth of cancer cells and suppress cancer metastasis, pointing to Hv1 as a potential target for anticancer drug

therapy, as well as a biomarker for the prognosis of breast cancer and possibly other types of cancers. In these studies, mice were injected with MDA-MB-231 cells, either with Hv1-siRNA lentivirus or Hv1-scr lentivirus, or without any lentivirus. The mice had tumor xenografts examined after thirty days, and it was revealed that in the mice injected with Hv1 knocked down by the siRNA, the proliferation of tumor cells was dramatically decreased. The overexpression of Hv1 was then concluded to contribute to the proliferation and invasiveness of breast cancer cells, and it is associated with a poor prognosis in breast cancer patients (Wang et al., 2012).

It was then found that Hv1 is highly expressed in other types of cancer cell lines as well. Hv1 is high expressed in colorectal tumor tissues and cell lines and adenocarcinomas, but poorly expressed in normal colorectal polyps. Hv1 could also be used as a biomarker for the prognosis and diagnosis of colorectal cancer patients in addition to breast cancer patients (Wang et al., 2013).

Based upon these studies, it is of interest to investigate whether there are other proteins closely related to Hv1, which may in turn also have implications in human disease. Hv1 is strongly linked to several types of cancers as well as ischemic stroke, and potentially other diseases of the immune system. Since Hv1 is expressed in microglia, it raises the possibility that other, related proteins that sense voltage could be expressed in neurons and have a role in cell electrical excitability, and therefore roles in diseases that affect the CNS.

The identification and characterization of such proteins associated with disease is of great importance to the fields of physiology and neuroscience, as well as having clinical significance. In the following chapters, I will describe the steps taken to identify novel voltage-sensitive proteins related to Hv1, and the work done to characterize the mechanism of block in Hv1 and the development of Hv1 inhibitors.

1.3 References

Aggarwal, S.K., and MacKinnon, R. (1996). Contribution of the S4 segment to gating charge in the Shaker K+ channel. Neuron *16*, 1169–1177.

Ahern, C.A., and Horn, R. (2004a). Stirring up controversy with a voltage sensor paddle. Trends Neurosci. *27*, 303–307.

Ahern, C.A., and Horn, R. (2004b). Specificity of charge-carrying residues in the voltage sensor of potassium channels. J. Gen. Physiol. *123*, 205–216.

Alberts, I.L., Nadassy, K., and Wodak, S.J. (1998). Analysis of zinc binding sites in protein crystal structures. Protein Sci. *7*, 1700–1716.

Armstrong, C.M., and Bezanilla, F. (1973). Currents related to movement of the gating particles of the sodium channels. Nature *242*, 459–461.

Armstrong, C.M., and Bezanilla, F. (1974). Charge movement associated with the opening and closing of the activation gates of the Na channels. J. Gen. Physiol. *63*, 533–552.

Ashcroft, F.M. (1999). Ion Channels and Disease (Academic Press).

Ashcroft, F.M. (2006). From molecule to malady. Nature *440*, 440–447.

Bedard, K., and Krause, K.-H. (2007). The NOX family of ROS-generating NADPH oxidases: physiology and pathophysiology. Physiol. Rev. *87*, 245–313.

Berger, T.K., and Isacoff, E.Y. (2011). The pore of the voltage-gated proton channel. Neuron *72*, 991–1000.

Bezanilla, F. (2000). The voltage sensor in voltage-dependent ion channels. Physiol. Rev. *80*, 555–592.

Bezanilla, F., and Armstrong, C.M. (1972). Negative conductance caused by entry of sodium and cesium ions into the potassium channels of squid axons. J. Gen. Physiol. *60*, 588–608.

Browne, D.L., Brunt, E.R., Griggs, R.C., Nutt, J.G., Gancher, S.T., Smith, E.A., and Litt, M. (1995). Identification of two new KCNA1 mutations in episodic ataxia/myokymia families. Hum. Mol. Genet. *4*, 1671–1672.

Browne, D.L., Gancher, S.T., Nutt, J.G., Brunt, E.R., Smith, E.A., Kramer, P., and Litt, M. (1994). Episodic ataxia/myokymia syndrome is associated with point mutations in the human potassium channel gene, KCNA1. Nat. Genet. *8*, 136–140.

Capasso, M., Bhamrah, M.K., Henley, T., Boyd, R.S., Langlais, C., Cain, K., Dinsdale, D., Pulford, K., Khan, M., Musset, B., et al. (2010). HVCN1 modulates BCR signal strength via regulation of BCR-dependent generation of reactive oxygen species. Nat. Immunol. *11*, 265–272.

Capasso, M., Decoursey, T.E., and Dyer, M.J.S. (2011). pH regulation and beyond: unanticipated functions for the voltage-gated proton channel, HVCN1. Trends Cell Biol. *21*, 20–28.

Catterall, W.A. (1986). Molecular properties of voltage-sensitive sodium channels. Annu. Rev. Biochem. *55*, 953–985.

Catterall, W.A. (1995). Structure and function of voltage-gated ion channels. Annu. Rev. Biochem. *64*, 493–531.

Catterall, W.A. (2011). Voltage-gated calcium channels. Cold Spring Harb Perspect Biol *3*, a003947.

Catterall, W.A., Dib-Hajj, S., Meisler, M.H., and Pietrobon, D. (2008). Inherited neuronal ion channelopathies: new windows on complex neurological diseases. J. Neurosci. *28*, 11768–11777.

Chemaly, El, A., Okochi, Y., Sasaki, M., Arnaudeau, S., Okamura, Y., and Demaurex, N. (2010). VSOP/Hv1 proton channels sustain calcium entry, neutrophil migration, and superoxide production by limiting cell depolarization and acidification. Journal of Experimental Medicine *207*, 129–139.

Chen, H., Rossier, C., Morris, M.A., Scott, H.S., Gos, A., Bairoch, A., and Antonarakis, S.E. (1999). A testis-specific gene, TPTE, encodes a putative transmembrane tyrosine phosphatase and maps to the pericentromeric region of human chromosomes 21 and 13, and to chromosomes 15, 22, and Y. Hum Genet *105*, 399–409.

Cherny, V.V., and DeCoursey, T.E. (1999). pH-dependent inhibition of voltage-gated H(+) currents in rat alveolar epithelial cells by Zn(2+) and other divalent cations. J. Gen. Physiol. *114*, 819–838.

Comu, S., Giuliani, M., and Narayanan, V. (1996). Episodic ataxia and myokymia syndrome: a new mutation of potassium channel gene Kv1.1. Ann. Neurol. *40*, 684–687.

Crick, F.H.C. (1953). The packing of α-helices: simple coiled-coils. Acta Cryst *6*, 689–697.

Cuello, L.G., Cortes, D.M., and Perozo, E. (2004). Molecular architecture of the KvAP voltage-dependent K+ channel in a lipid bilayer. Science *306*, 491–495.

Deb, P., Sharma, S., and Hassan, K.M. (2010). Pathophysiologic mechanisms of acute ischemic stroke: An overview with emphasis on therapeutic significance beyond thrombolysis. Pathophysiology *17*, 197–218.

DeCoursey, T.E., and Cherny, V.V. (1998). Temperature dependence of voltage-gated H+ currents in human neutrophils, rat alveolar epithelial cells, and mammalian phagocytes. J. Gen. Physiol. *112*, 503–522.

Decoursey, T.E. (2003). Voltage-gated proton channels and other proton transfer pathways. Physiol. Rev. *83*, 475–579.

Doyle, D.A., Cabral, J.M., Pfuetzner, R.A., Kuo, A., Gulbis, J.M., Cohen, S.L., Chait, B.T., and Mackinnon, R. (1998). The structure of the potassium channel: molecular basis of K+ conduction and selectivity. Science *280*, 69–77.

Eder, C., and DeCoursey, T.E. (2001). Voltage-gated proton channels in microglia. Prog. Neurobiol. *64*, 277–305.

Fais, S., De Milito, A., You, H., and Qin, W. (2007). Targeting vacuolar H+-ATPases as a new strategy against cancer. Cancer Res. *67*, 10627–10630.

Fogel, M., and Hastings, J.W. (1972). Bioluminescence: mechanism and mode of control of scintillon activity. Proc. Natl. Acad. Sci. U.S.a. *69*, 690–693.

Fujiwara, Y., Kurokawa, T., Takeshita, K., Kobayashi, M., Okochi, Y., Nakagawa, A., and Okamura, Y. (2012). The cytoplasmic coiled-coil mediates cooperative gating temperature sensitivity in the voltage-gated H(+) channel Hv1. Nat Commun *3*, 816.

Gandhi, C.S., and Isacoff, E.Y. (2002). Molecular models of voltage sensing. J. Gen. Physiol. *120*, 455–463.

Gonzalez, C., Koch, H.P., Drum, B.M., and Larsson, H.P. (2010). Strong cooperativity between subunits in voltage-gated proton channels. Nat. Struct. Mol. Biol. *17*, 51–56.

Gonzalez, C., Rebolledo, S., Perez, M.E., and Larsson, H.P. (2013). Molecular mechanism of voltage sensing in voltage-gated proton channels. J. Gen. Physiol. *141*, 275–285.

Guy, H.R., and Conti, F. (1990). Pursuing the structure and function of voltage-gated channels. Trends Neurosci. *13*, 201–206.

Halaszovich, C.R., Leitner, M.G., Mavrantoni, A., Le, A., Frezza, L., Feuer, A., Schreiber, D.N., Villalba-Galea, C.A., and Oliver, D. (2012). A human phospholipid phosphatase activated by a transmembrane control module. J. Lipid Res. *53*, 2266–2274.

Halaszovich, C.R., Schreiber, D.N., and Oliver, D. (2009). Ci-VSP is a depolarization-activated phosphatidylinositol-4, 5-bisphosphate and phosphatidylinositol-3, 4, 5-trisphosphate 5′-phosphatase. Journal of Biological Chemistry *284*, 2106–2113.

Heginbotham, L., Lu, Z., Abramson, T., and MacKinnon, R. (1994). Mutations in the K+ channel signature sequence. Biophys. J. *66*, 1061–1067.

Hille, B. (2001). Ion Channels of Excitable Membranes (Sunderland: Sinauer Associates Inc).

Iovannisci, D., Illek, B., and Fischer, H. (2010). Function of the HVCN1 proton channel in airway epithelia and a naturally occurring mutation, M91T. J. Gen. Physiol. *136*, 35–46.

Jiang, Y., Ruta, V., Chen, J., Lee, A., and Mackinnon, R. (2003). The principle of gating charge movement in a voltage-dependent K+ channel. Nature *423*, 42–48.

Jogini, V., and Roux, B. (2005). Electrostatics of the intracellular vestibule of K+ channels. J. Mol. Biol. *354*, 272–288.

Jurkat-Rott, K., Groome, J., and Lehmann-Horn, F. (2012). Pathophysiological role of omega pore current in channelopathies. Front Pharmacol *3*, 1–19.

Kamb, A., Iverson, L.E., and Tanouye, M.A. (1987). Molecular characterization of Shaker, a Drosophila gene that encodes a potassium channel. Cell *50*, 405–413.

Kecskemethy, N., Casal, J., Ferrus, A., and Pongs, O. (1987). Molecular organization of the maternal effect region of the Shaker complex of Drosophila: characterization of an IA channel transcript with homology to vertebrate Na+ …. The EMBO ….

Keynes, R.D., and Rojas, E. (1974). Kinetics and steady-state properties of the charged system controlling sodium conductance in the squid giant axon. The Journal of Physiology *239*, 393–434.

Kirichok, Y., Navarro, B., and Clapham, D.E. (2006). Whole-cell patch-clamp measurements of spermatozoa reveal an alkaline-activated Ca2+ channel. Nature *439*, 737–740.

Knobbe, C.B., Lapin, V., Suzuki, A., and Mak, T.W. (2008). The roles of PTEN in development, physiology and tumorigenesis in mouse models: a tissue-by-tissue survey. Oncogene *27*, 5398–5415.

Koch, H.P., Kurokawa, T., Okochi, Y., Sasaki, M., Okamura, Y., and Larsson, H.P. (2008). Multimeric nature of voltage-gated proton channels. Proc. Natl. Acad. Sci. U.S.a. *105*, 9111–9116.

Kohout, S.C., Ulbrich, M.H., Bell, S.C., and Isacoff, E.Y. (2008). Subunit organization and functional transitions in Ci-VSP. Nat. Struct. Mol. Biol. *15*, 106–108.

Kurokawa, T., and Okamura, Y. (2014). Mapping of sites facing aqueous environment of voltage-gated proton channel at resting state: a study with PEGylation protection. Biochim. Biophys. Acta *1838*, 382–387.

Lecar, H., Larsson, H.P., and Grabe, M. (2003). Electrostatic model of S4 motion in voltage-gated ion channels. Biophys. J. *85*, 2854–2864.

Lee, S.-Y., Letts, J.A., and Mackinnon, R. (2008). Dimeric subunit stoichiometry of the human voltage-dependent proton channel Hv1. Proc. Natl. Acad. Sci. U.S.a. *105*, 7692–7695.

Leslie, N.R., Yang, X., Downes, C.P., and Weijer, C.J. (2007). PtdIns(3,4,5)P3-Dependent and -Independent Roles for PTEN in the Control of Cell Migration. Current Biology *17*, 115–125.

Li, J., Yen, C., Liaw, D., Podsypanina, K., Bose, S., Wang, S.I., Puc, J., Miliaresis, C., Rodgers, L.,

and McCombie, R. (1997). PTEN, a putative protein tyrosine phosphatase gene mutated in human brain, breast, and prostate cancer. Science *275*, 1943–1947.

Li, M., and Lester, H.A. (2001). Ion channel diseases of the central nervous system. CNS Drug Rev *7*, 214–240.

Li, M., Unwin, N., Stauffer, K.A., Jan, Y.N., and Jan, L.Y. (1994). Images of purified Shaker potassium channels. Curr. Biol. *4*, 110–115.

Li, S.J., Zhao, Q., Zhou, Q., Unno, H., Zhai, Y., and Sun, F. (2010). The role and structure of the carboxyl-terminal domain of the human voltage-gated proton channel Hv1. J. Biol. Chem. *285*, 12047–12054.

Lishko, P.V., and Kirichok, Y. (2010). The role of Hv1 and CatSper channels in sperm activation. The Journal of Physiology *588*, 4667–4672.

Long, S.B., Campbell, E.B., and Mackinnon, R. (2005). Crystal structure of a mammalian voltage-dependent Shaker family K+ channel. Science *309*, 897–903.

Lupas, A. (1996). Coiled coils: new structures and new functions. Trends Biochem. Sci. *21*, 375–382.

Maehama, T., and Dixon, J.E. (1998). The tumor suppressor, PTEN/MMAC1, dephosphorylates the lipid second messenger, phosphatidylinositol 3,4,5-trisphosphate. J. Biol. Chem. *273*, 13375–13378.

Mahaut-Smith, M.P. (1989). The effect of zinc on calcium and hydrogen ion currents in intact snail neurones. J. Exp. Biol. *145*, 455–464.

Matthews, E., Labrum, R., Sweeney, M.G., Sud, R., Haworth, A., Chinnery, P.F., Meola, G., Schorge, S., Kullmann, D.M., and Davis, M.B. (2009). Voltage sensor charge loss accounts for most cases of hypokalemic periodic paralysis. Neurology *72*, 1544–1547.

Moskowitz, M.A., Lo, E.H., and Iadecola, C. (2010). The science of stroke: mechanisms in search of treatments. Neuron *67*, 181–198.

Murata, Y., and Okamura, Y. (2007). Depolarization activates the phosphoinositide phosphatase Ci-VSP, as detected in Xenopus oocytes coexpressing sensors of PIP2. The Journal of Physiology *583*, 875–889.

Murata, Y., Iwasaki, H., Sasaki, M., Inaba, K., and Okamura, Y. (2005). Phosphoinositide phosphatase activity coupled to an intrinsic voltage sensor. Nature *435*, 1239–1243.

Musset, B., Morgan, D., Cherny, V.V., MacGlashan, D.W., Thomas, L.L., Ríos, E., and Decoursey, T.E. (2008). A pH-stabilizing role of voltage-gated proton channels in IgE-mediated activation of human basophils. Proc. Natl. Acad. Sci. U.S.a. *105*, 11020–11025.

Musset, B., Smith, S.M.E., Rajan, S., Cherny, V.V., Sujai, S., Morgan, D., and Decoursey, T.E.

(2010). Zinc inhibition of monomeric and dimeric proton channels suggests cooperative gating. The Journal of Physiology *588*, 1435–1449.

Musset, B., Smith, S.M.E., Rajan, S., Morgan, D., Cherny, V.V., and Decoursey, T.E. (2011). Aspartate 112 is the selectivity filter of the human voltage-gated proton channel. Nature *480*, 273–277.

Noda, M., Shimizu, S., Tanabe, T., Takai, T., Kayano, T., Ikeda, T., Takahashi, H., Nakayama, H., Kanaoka, Y., and Minamino, N. (1984). Primary structure of Electrophorus electricus sodium channel deduced from cDNA sequence. Nature *312*, 121–127.

Okamura, Y. (2007). Biodiversity of voltage sensor domain proteins. Pflugers Arch. *454*, 361–371.

Okochi, Y., Sasaki, M., Iwasaki, H., and Okamura, Y. (2009). Voltage-gated proton channel is expressed on phagosomes. Biochem. Biophys. Res. Commun. *382*, 274–279.

Papazian, D.M., Timpe, L.C., Jan, Y.N., and Jan, L.Y. (1991). Alteration of voltage-dependence of Shaker potassium channel by mutations in the S4 sequence. Nature *349*, 305–310.

PAULING, L., and COREY, R.B. (1953). Compound Helical Configurations of Polypeptide Chains: Structure of Proteins of the α-Keratin Type. Nature *171*, 59–61.

Payandeh, J., Scheuer, T., Zheng, N., and Catterall, W.A. (2011). The crystal structure of a voltage-gated sodium channel. Nature *475*, 353–358.

Perozo, E., MacKinnon, R., Bezanilla, F., and Stefani, E. (1993). Gating currents from a nonconducting mutant reveal open-closed conformations in Shaker K+ channels. Neuron *11*, 353–358.

Ramsey, I.S., Moran, M.M., Chong, J.A., and Clapham, D.E. (2006). A voltage-gated proton-selective channel lacking the pore domain. Nature *440*, 1213–1216.

Ramsey, I.S., Ruchti, E., Kaczmarek, J.S., and Clapham, D.E. (2009). Hv1 proton channels are required for high-level NADPH oxidase-dependent superoxide production during the phagocyte respiratory burst. Proc. Natl. Acad. Sci. U.S.a. *106*, 7642–7647.

Ray, P.D., Huang, B.-W., and Tsuji, Y. (2012). Reactive oxygen species (ROS) homeostasis and redox regulation in cellular signaling. Cell. Signal. *24*, 981–990.

Rojas, C.V., Wang, J.Z., Schwartz, L.S., Hoffman, E.P., Powell, B.R., and Brown, R.H. (1991). A Met-to-Val mutation in the skeletal muscle Na+ channel alpha-subunit in hyperkalaemic periodic paralysis. Nature *354*, 387–389.

Sasaki, M., Takagi, M., and Okamura, Y. (2006). A voltage sensor-domain protein is a voltage-gated proton channel. Science *312*, 589–592.

Sennoune, S.R., Bakunts, K., Martínez, G.M., Chua-Tuan, J.L., Kebir, Y., Attaya, M.N., and

Martínez-Zaguilán, R. (2004). Vacuolar H+-ATPase in human breast cancer cells with distinct metastatic potential: distribution and functional activity. Am. J. Physiol., Cell Physiol. *286*, C1443–C1452.

Seoh, S.A., Sigg, D., Papazian, D.M., and Bezanilla, F. (1996). Voltage-sensing residues in the S2 and S4 segments of the Shaker K+ channel. Neuron *16*, 1159–1167.

Shao, X.M., and Papazian, D.M. (1993). S4 mutations alter the single-channel gating kinetics of Shaker K+ channels. Neuron *11*, 343–352.

Shroff, S., Overman, M.J., Rashid, A., Shroff, R.T., Wang, H., Chatterjee, D., Katz, M.H., Lee, J.E., Wolff, R.A., Abbruzzese, J.L., et al. (2013). The expression of PTEN is associated with improved prognosis in patients with ampullary adenocarcinoma after pancreaticoduodenectomy. Arch. Pathol. Lab. Med. *137*, 1619–1626.

Sokolov, S., Scheuer, T., and Catterall, W.A. (2007). Gating pore current in an inherited ion channelopathy. Nature *446*, 76–78.

Starace, D.M., and Bezanilla, F. (2004). A proton pore in a potassium channel voltage sensor reveals a focused electric field. Nature *427*, 548–553.

Steck, P.A., Pershouse, M.A., Jasser, S.A., Yung, W.K., Lin, H., Ligon, A.H., Langford, L.A., Baumgard, M.L., Hattier, T., Davis, T., et al. (1997). Identification of a candidate tumour suppressor gene, MMAC1, at chromosome 10q23.3 that is mutated in multiple advanced cancers. Nat. Genet. *15*, 356–362.

Stefani, E., Bezanilla, F., and Papazian, D.M. (1994). S4 mutations alter gating currents of Shaker K channels. Biophys. J.

Takeshita, K., Sakata, S., Yamashita, E., Fujiwara, Y., Kawanabe, A., Kurokawa, T., Okochi, Y., Matsuda, M., Narita, H., Okamura, Y., et al. (2014). X-ray crystal structure of voltage-gated proton channel. Nat. Struct. Mol. Biol.

Tanabe, T., Takeshima, H., Mikami, A., Flockerzi, V., Takahashi, H., Kangawa, K., Kojima, M., Matsuo, H., Hirose, T., and Numa, S. (1987). Primary structure of the receptor for calcium channel blockers from skeletal muscle. Nature *328*, 313–318.

Tao, X., Lee, A., Limapichat, W., Dougherty, D.A., and Mackinnon, R. (2010). A gating charge transfer center in voltage sensors. Science *328*, 67–73.

Tapparel, C., Reymond, A., Girardet, C., Guillou, L., Lyle, R., Lamon, C., Hutter, P., and Antonarakis, S.E. (2003). The TPTE gene family: cellular expression, subcellular localization and alternative splicing. Gene *323*, 189–199.

Tempel, B.L., Papazian, D.M., Schwarz, T.L., Jan, Y.N., and Jan, L.Y. (1987). Sequence of a probable potassium channel component encoded at Shaker locus of Drosophila. Science *237*, 770–775.

Terlau, H., and Stühmer, W. (1998). Structure and function of voltage-gated ion channels. Naturwissenschaften *85*, 437–444.

Thomas, R.C., and Meech, R.W. (1982). Hydrogen ion currents and intracellular pH in depolarized voltage-clamped snail neurones. Nature *299*, 826–828.

Tombola, F., Pathak, M.M., and Isacoff, E.Y. (2005a). How far will you go to sense voltage? Neuron *48*, 719–725.

Tombola, F., Pathak, M.M., and Isacoff, E.Y. (2005b). Voltage-sensing arginines in a potassium channel permeate and occlude cation-selective pores. Neuron *45*, 379–388.

Tombola, F., Pathak, M.M., and Isacoff, E.Y. (2006). How does voltage open an ion channel? Annu. Rev. Cell Dev. Biol. *22*, 23–52.

Tombola, F., Ulbrich, M.H., and Isacoff, E.Y. (2008). The voltage-gated proton channel Hv1 has two pores, each controlled by one voltage sensor. Neuron *58*, 546–556.

Tombola, F., Ulbrich, M.H., Kohout, S.C., and Isacoff, E.Y. (2010). The opening of the two pores of the Hv1 voltage-gated proton channel is tuned by cooperativity. Nat. Struct. Mol. Biol. *17*, 44–50.

Ulbrich, M.H., and Isacoff, E.Y. (2007). Subunit counting in membrane-bound proteins. Nat. Methods *4*, 319–321.

Uzoh, C.C., Perks, C.M., Bahl, A., Holly, J.M.P., Sugiono, M., and Persad, R.A. (2009). PTEN-mediated pathways and their association with treatment-resistant prostate cancer. BJU Int. *104*, 556–561.

Walker, S.M., Downes, C.P., and Leslie, N.R. (2001). TPIP: a novel phosphoinositide 3-phosphatase. Biochem. J. *360*, 277–283.

Wang, Y., Li, S.J., Pan, J., Che, Y., Yin, J., and Zhao, Q. (2011). Specific expression of the human voltage-gated proton channel Hv1 in highly metastatic breast cancer cells, promotes tumor progression and metastasis. Biochem. Biophys. Res. Commun. *412*, 353–359.

Wang, Y., Li, S.J., Wu, X., Che, Y., and Li, Q. (2012). Clinicopathological and biological significance of human voltage-gated proton channel Hv1 protein overexpression in breast cancer. J. Biol. Chem. *287*, 13877–13888.

Wang, Y., Wu, X., Li, Q., Zhang, S., and Li, S.J. (2013). Human voltage-gated proton channel hv1: a new potential biomarker for diagnosis and prognosis of colorectal cancer. PLoS ONE *8*, e70550.

Wu, L.-J., Wu, G., Akhavan Sharif, M.R., Baker, A., Jia, Y., Fahey, F.H., Luo, H.R., Feener, E.P., and Clapham, D.E. (2012). The voltage-gated proton channel Hv1 enhances brain damage from ischemic stroke. Nat. Neurosci. *15*, 565–573.

Wu, Y., Dowbenko, D., Pisabarro, M.T., Dillard-Telm, L., Koeppen, H., and Lasky, L.A. (2001). PTEN 2, a Golgi-associated testis-specific homologue of the PTEN tumor suppressor lipid phosphatase. J. Biol. Chem. *276*, 21745–21753.

Zhang, X., Ren, W., DeCaen, P., Yan, C., Tao, X., Tang, L., Wang, J., Hasegawa, K., Kumasaka, T., He, J., et al. (2012). Crystal structure of an orthologue of the NaChBac voltage-gated sodium channel. Nature *486*, 130–134.

Zhou, Y., Morais-Cabral, J.H., Kaufman, A., and MacKinnon, R. (2001). Chemistry of ion coordination and hydration revealed by a K+ channel-Fab complex at 2.0 A resolution. Nature *414*, 43–48.

Chapter 2: Voltage-sensing domain of voltage-gated proton channel Hv1 shares mechanism of block with pore domains

(Hong, Pathak, Kim, Ta, Tombola)

Abstract

Voltage-gated sodium, potassium, and calcium channels are made of a pore domain (PD) controlled by four voltage-sensing domains (VSDs). The PD contains the ion permeation pathway and the activation gate located on the intracellular side of the membrane. A large number of small molecules are known to inhibit the PD by acting as open channel blockers. The voltage-gated proton channel Hv1 is made of two VSDs and lacks the PD. The location of the activation gate in the VSD is unknown and open channel blockers for VSDs have not yet been identified. Here we describe a class of small molecules which act as open channel blockers on the Hv1 VSD and find that a highly conserved phenylalanine in the charge transfer center of the VSD plays a key role in blocker binding. We then use one of the blockers to show that Hv1 contains two intracellular and allosterically-coupled gates.

2.1 Introduction

The Hv1 voltage-gated proton channel (also known as HVCN1 or VSOP) is a member of the superfamily of proteins containing voltage-sensing domains (VSDs) (Ramsey et al., 2006; Sasaki et al., 2006). These domains are made of four membrane-spanning segments (S1

through S4) and their function is to detect changes in membrane potential in both excitable and non-excitable cells (Fig. 2.1A) (Okamura, 2007; Yu and Catterall, 2004). Voltage-gated sodium, potassium, and calcium channels are also VSD-containing proteins. They are all made of a pore domain (PD) responsible for selective ion permeation, and four VSDs. A gate located on the intracellular side of the PD (known as activation gate) opens and closes as a function of membrane potential due to direct interaction with the VSDs (Hille, 2001) (Fig. 2.1B).

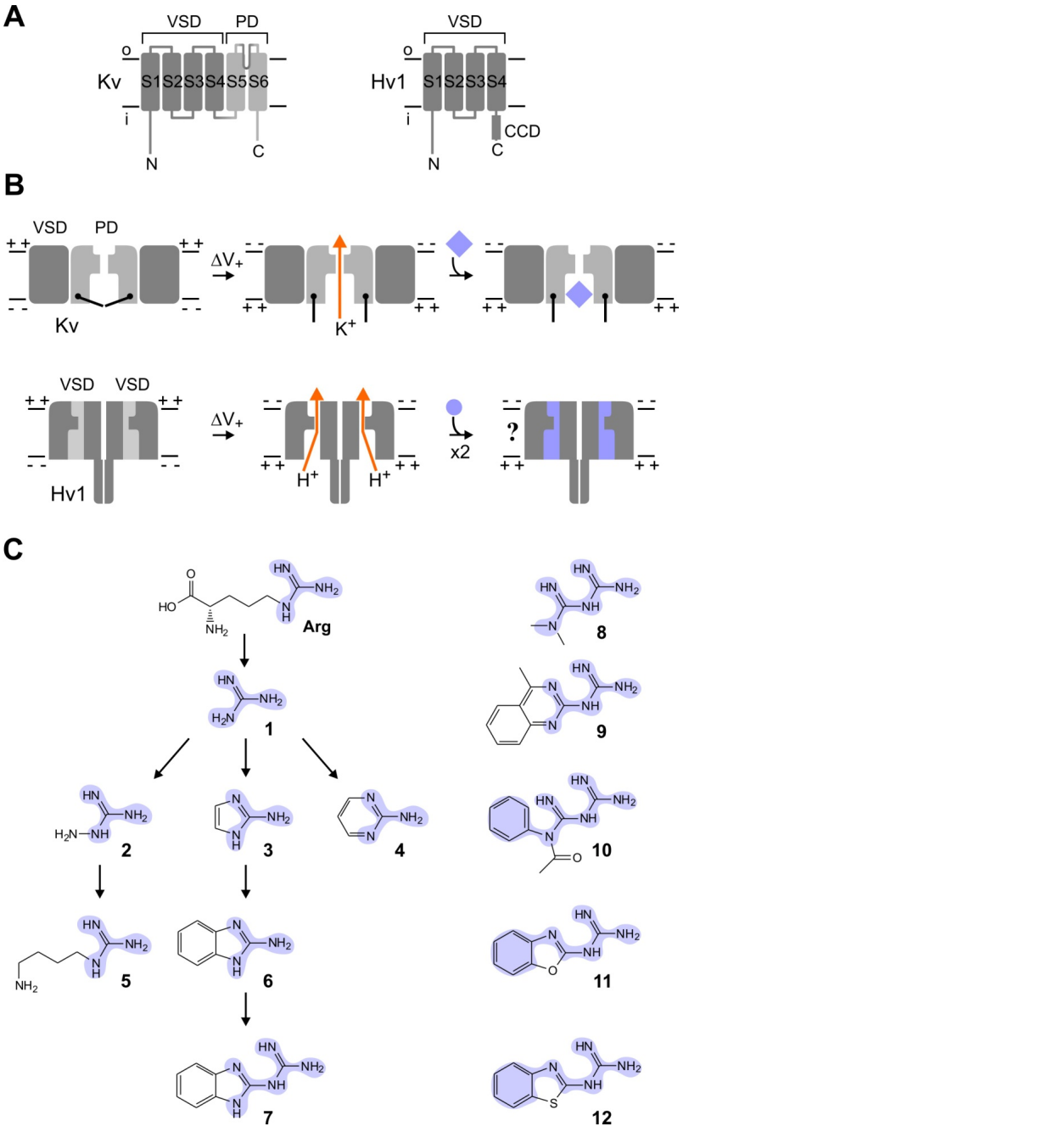

Figure 2.1. Gating of a VSD pore probed with intracellular blockers. (A) Topology of VSD-containing channels with and without a pore domain (PD). CCD: coiled-coil domain. **(B)** Voltage-dependent opening and block of PD (top) and VSD (bottom). The Hv1 channel contains two conducting VSDs. The location of its activation gates is not known, nor is the mechanism of VSD block. Only two of the four Kv VSDs are shown for clarity. **(C)** Guanidine derivatives tested as potential Hv1 intracellular blockers. [1] Guanidine, [2] aminoguanidine, [3] 2-aminoimidazole, [4] 2-aminopyrimidine, [5] agmatine, [6] 2-aminobenzimidazole, [7] 2-guanidinobenzimidazole, [8] metformin, [9] 2-guanidino-4-methylquinazoline, [10] N-(guanidino-imino-methyl)-N-phenylacetamide, [11] 1-(1,3-benzoxazol-2-yl)guanidine, [12] 1-(1,3-benzothiazol-2-yl)guanidine. Guanidine moieties are highlighted in blue in compounds 1-7. The parts of compound 7 that are conserved in compounds 8-12 are also highlighted in blue.

The Hv1 channel does not have a pore domain and its VSD is responsible for proton permeation (Lee et al., 2009; Ramsey et al., 2006; Sasaki et al., 2006). The S4 segment, which contains voltage-sensitive arginines highly conserved in other voltage-gated ion channels, is directly connected to a C-terminal coiled-coil domain (Fig. 2.1A). Hv1 has been shown to form dimers in which two VSD subunits are held together by the coiled-coil domain (Fig. 2.1A – B) (Koch et al., 2008; Lee et al., 2008; Li et al., 2010; Tombola et al., 2008). The deletion of the Hv1 N and C terminal domains, as well as the substitution of these domains with the corresponding parts of the voltage-sensitive phosphatase Ci-VSP (Murata et al., 2005), were found to produce monomeric channels capable of voltage-dependent proton conduction, indicating that the gating machinery is contained in each VSD (Koch et al., 2008; Tombola et al., 2008). The nature of this gating machinery and the location of the activation gate in the VSD are still unknown.

Open channel blockers are inhibitors that bind the ion permeation pathway of a channel only when its gate is open (Hille, 2001). We reasoned that if open channel blockers were available for ion permeable VSDs, they could be used to study the gating mechanism of Hv1 and in particular to locate the activation gate in the VSD. Here we describe guanidine derivatives that bind the Hv1 channel from the intracellular side of the membrane and act as potential channel blockers. We find that the most effective of these compounds, 2-guanidiniumbenzimidazole (2GBI), can access the core of the VSD only when the channel is in the open conformation and that the highly conserved phenylalanine 150 in the S2 transmembrane helix plays a key role in blocker binding. We then use mutations at position 150 to characterize the interaction between the blocker and the VSD gating machinery.

As previously shown for the pore domain, we find that the activation gate of the VSD is located on the intracellular side of the membrane and that when 2GBI is bound to its receptor the gate cannot close (*foot in the door* mechanism of block). By comparing the recovery from block of dimeric and monomeric Hv1 channels, we find that once one of the two subunits releases its blocker, the state of its gate determines the rate of blocker unbinding from the neighboring subunit. We discuss the structural implications of this mechanism of block for the VSD's intracellular vestibule, and for the coupling between the gates in the channel's two subunits.

The Hv1 channel is known to play important roles in proton extrusion, pH homeostasis, and production of reactive oxygen species in a variety of cell types (Capasso et al., 2011). It has been recently implicated in cancer development (Wang et al., 2012) and brain damage during ischemic stroke (Wu et al., 2012). Understanding how compounds like guanidine derivatives interact with the channel's VSD and block proton conduction is an important step toward the development of pharmacological treatments for diseases caused by Hv1 hyperactivity. In addition, it can provide important clues on how to block VSDs of other voltage-gated ion channels when they become ion permeable as a result of naturally occurring mutations (Sokolov et al., 2007).

2.2 Materials and Methods

Channel expression in *Xenopus* oocytes

Constructs containing the sequence of the human Hv1 channel were generated from cDNA kindly provided by David Clapham (Ramsey et al., 2006) and from IMAGE clone 5577070 (Open Biosystems). The cDNAs for Ci-VSP and Ci-VSOP were gifts from Yasushi Okamura (Murata et al., 2005; Sasaki et al., 2006). The cDNA for Eh-HVCN1 codon-optimized for expression in mammalian cells and Xenopus oocytes was kindly provided by Colin Brownlee and Glen Wheeler (Taylor et al., 2011). With the exception of Ci-VSOP, all the constructs were subcloned in the pGEMHE vector (Liman et al., 1992) by the SOEing technique (Horton et al., 1990). In the N_{VSP}-Hv1-C_{VSP} chimera, residues 1-96 and 228-273 of Hv1 were replaced by residues 1-113 and 240-576 of Ci-VSP, respectively. Single point mutations were introduced with standard PCR techniques. In the Hv1 linked dimers, the two consecutive subunits were connected by the sequence GGSGGSGGSGGSGGSGG (Tombola et al., 2008).

Plasmids were linearized with either NheI or SphI restriction enzymes (New England Biolabs) before *in vitro* transcription. RNA synthesis was carried out with a T7 mMessage mMachine transcription kit (Ambion). Ci-VSOP was in the pSD64TF expression vector (Krieg and Melton, 1984). The linearized plasmid was transcribed with SP6 RNA polymerase. cRNAs were injected in Xenopus oocytes (50 nl per cell, 0.3-1.5 µg/µl) 1-3 days before the electrophysiological measurements. Cells were kept at 18 °C in ND96 medium

containing 96 mM NaCl, 2 mM KCl, 1.8 mM $CaCl_2$, 1 mM $MgCl_2$, 10 mM HEPES, 5 mM pyruvate, 100 μg/ml gentamycin, pH 7.2.

Hv1 inhibitors

All the compounds tested were at the highest purity commercially available. Guanidine hydrochloride was from MP Biomedicals. Aminoguanidine hydrochloride was from Acros orgnanics. 2-aminoimidazole sulfate, 2-aminopyrimidine, agmatine sulfate, 2-aminobenzimidazole, 2-guanidinobenzimidazole, 1,1-dimethylbiguanide hydrochloride, 2-guanidino-4-methylquinazoline hydrochloride, and N-(guanidino-imino-methyl)-N-phenylacetamide hydrochloride, were from Sigma-Aldrich. 1-(1,3-benzoxazol-2-yl)guanidine and 1-(1,3-benzothiazol-2-yl)guanidine were from both ChemDiv and Sigma-Aldrich. The compounds were directly dissolved in the recording solutions at the desired final concentrations or prepared as 100X stock solutions in the same medium. To keep 1-(1,3-benzoxazol-2-yl)guanidine (GBOZ) in solution at the highest concentrations tested on wild type Hv1 channels, DMSO was added to a maximal ratio of 5% v/v for the 4 mM solution. We tested recoding solutions with DMSO up to 10 % v/v on inside-out patches containing Hv1 channels, and 5% was the maximal ratio that we were able to use without altering the measured proton currents or compromising the stability of the patch under perfusion.

We estimated the pK_a of the guanidinium group of the tested inhibitors using the pK_a calculation plugin of Marvin (http://www.ChemAxon.com). With the exception of 2-

aminopyrimidine, the compounds were predicted to be primarily in the protonated and positively charged form at pH=6.0. Compounds 7, 11, and 12 were also analyzed as free ligands in PROPKA3.1 (http://propka.ki.ku.dk) (Søndergaard et al., 2011). A charge of +1 was predicted for the three molecules under the pH conditions used for the measurements.

Patch clamp measurements

Electrophysiological measurements on oocytes were performed in inside-out and outside-out patch configurations using an Axopatch 200B amplifier controlled by pClamp10 software through an Axon Digidata 1440A (Molecular Devices). Unless otherwise specified, the bath solution contained 100 mM 2-(N-morpholino)ethanesulphonic acid (MES), 30 mM tetraethylammonium (TEA) methanesulfonate, 5 mM TEA chloride, 5 mM ethyleneglycol-bis(2-aminoethyl)-N,N,N',N'-tetra-acetic acid (EGTA), adjusted to pH 6.0 with TEA hydroxide. For recordings carried out in the absence of pH gradient (pH_i = pH_o = 6.0), the pipette solution had the same composition of the bath solution. Some of the measurements were performed in the presence of a pH gradient (pH_i = 6.0, pH_o = 7.5). In these cases the extracellular solution contained 100 mM 4-(2-hydroxyethyl)-1-piperazineethanesulfonic acid (HEPES), 40 mM TEA methanesulfonate, 5 mM TEA chloride, adjusted to pH 7.5 with TEA hydroxide. All measurements were performed at 22 ± 2 °C. Pipettes had 2–4 MΩ access resistance. Current traces were filtered at 1 kHz, sampled at 5 kHz and analyzed with Clampfit10.2 (Molecular Devices) and Origin8.1 (OriginLab).

Modeling of channel block

The process of channel block in dimeric and monomeric Hv1 was simulated with Berkeley Madonna 8.3 using the Runge-kutta 4 integration method (Macey et al., 2009). The model calculated the proton current in response to different voltage protocols in the absence and presence of 2GBI. The values of the rate constants used to generate the traces in Fig. 2.6B – D and Fig. S2.2 are reported in Fig. S2.3. Dimeric channels were modeled by 6 distinct states (CC, OC, OO, BC, BO, BB), which took into account the fact that states OB, CB and CO are equivalent to states BO, BC and OC respectively. Thus at any point of time the total number of channels was represented by $N = N_{CC} + N_{OO} + N_{BB} + 2N_{OC} + 2N_{BO} + 2N_{BC}$.

2.3 Results

2.3.1 Inhibition of Hv1 channels by the guanidine derivative 2GBI

Guanidinium was previously found to permeate the VSDs of mutated voltage-gated sodium and potassium channels (Sokolov et al., 2010; Tombola et al., 2005), and to inhibit Hv1 without shifting the channel's activation curve (Tombola et al., 2008). Because of its structural similarity to the S4 voltage-sensing arginines, guanidinium appeared to be a good starting compound to develop inhibitors that binds to the core of the VSD. Guanidinium is effective at inhibiting proton currents in the millimolar concentration range. We hypothesized that more complex molecules containing the guanidine moiety could have a higher binding affinity for Hv1. We screened guanidine derivatives with

different steric features (Fig. 2.1C) on inside-out patches from Xenopus oocytes expressing the human Hv1 channel. The proton current elicited by depolarization to +120 mV was measured before and after addition of each compound to the bath solution at the final concentration of 200 μM (Fig. 2.2A – C). Compounds 3, 5, 6, 7, 9, and 12 were found to be more effective at inhibiting Hv1 than guanidinium (compound 1), while the other compounds were equally or less effective than guanidinium. The inhibition was fully reversible for all the compounds. With the exception of compound 4, the protonated and positively charged forms of the tested inhibitors are expected to be the most abundant in solution at the pH used for the measurements (see Fig. S2.1).

We first examined compounds 1 through 7 and found that when the guanidine structure was part of a five-membered aromatic ring, the resulting inhibitors blocked the proton current more effectively than guanidinium alone (e.g., compounds 3 and 6 in Fig. 2.1C and Fig. 2.2C). The presence of a second guanidine group, conjugated with the one on the ring, in compound 7 (2GBI) further increased the affinity for the channel (Fig. 2.1C and Fig. 2.2A – D). We then examined compounds 8 through 12 to gain insight on the molecular features that make 2GBI the most effective inhibitor. Compounds 8, 9, and 10 share with 2GBI the conjugated double guanidine substructure but were not as effective as 2GBI at inhibiting the proton channel. Compounds 11 and 12 differ from 2GBI and from each other only at one position in the five-membered ring. However, compound 12 inhibited the proton current almost as effectively as 2GBI while compound 11 was even less effective than simple guanidinium. These results indicate that the binding site for guanidine derivatives on the proton channel is highly selective.

Transient application of 2GBI on the intracellular side of the membrane while the channels were held open at +120 mV resulted in fast current reduction (Fig. S2.2A). Transient application of the compound before the channels were opened had no effect on the current elicited by subsequent depolarization (Fig. S2.2A). When 2GBI was applied before the depolarization step and maintained throughout the recording, the current reached a steady state level of inhibition with the same kinetics of channel opening. The same steady state level was reached more rapidly when the inhibitor was applied during the depolarization step (Fig. S2.2B).

2GBI failed to inhibit the outward Hv1 current elicited by depolarization at +120 mV and the inward tail current generated during membrane repolarization at -80 mV when added to the bath solution in outside-out patch configuration (Fig. 2.2B and Fig. S2.2C – D). The strong sensitivity of Hv1 to intracellular 2GBI and the lack of sensitivity to extracellular 2GBI (measured over the same time scale and concentration range) imply that the binding site on the channel is directly accessible only from the intracellular side of the membrane. However, slow membrane crossing by guanidine derivatives has been previously observed (Kalia and Swartz, 2011). So, we cannot exclude that longer treatments with extracellular 2GBI than the ones tested here could result in Hv1 inhibition.

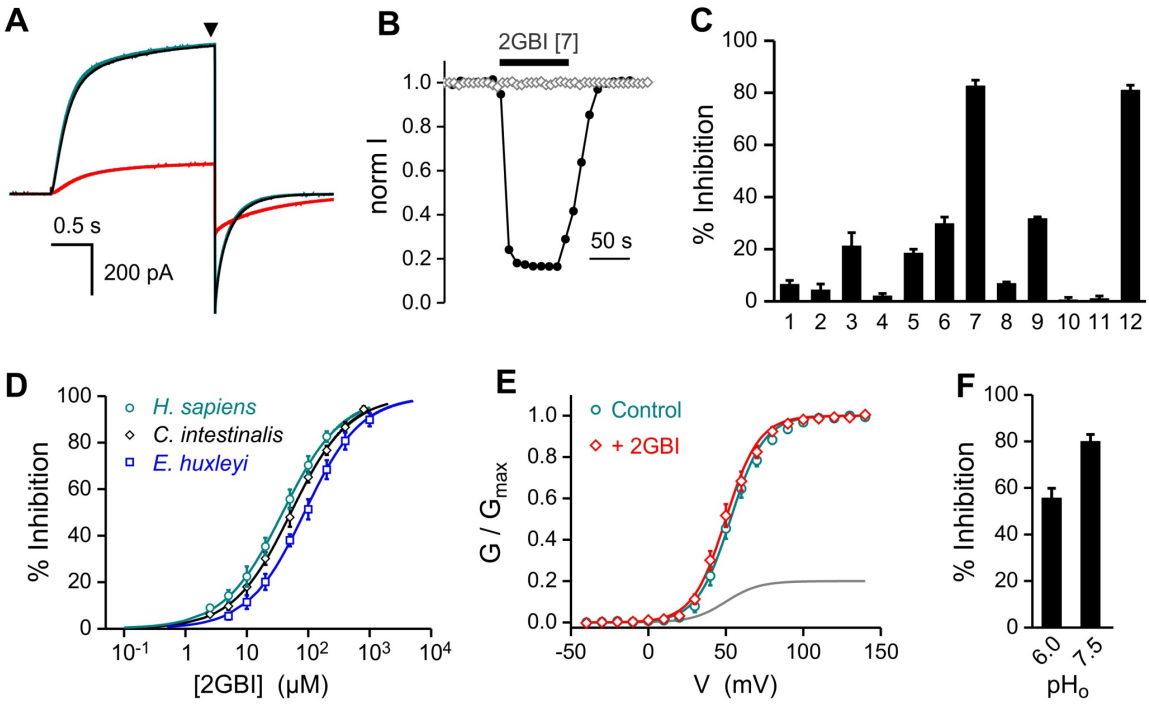

Figure 2.2. Inhibition of proton channel activity by guanidine derivatives. (A) Proton currents measured in an inside-out patch from a Xenopus oocyte expressing wild type human Hv1 before (black trace) and after (red trace) addition 2GBI (compound #7) in the bath solution (200 μM). Teal trace (overlapping black trace) is the current measured after inhibitor washout. Currents were activated by depolarizations to +120 mV from a holding potential of -80 mV. pH_i = pH_o = 6.0. The current measured at the end of the depolarization step (black triangle) was used to produce plots like the one shown in (B). **(B)** Time courses of inhibition produced by 200 μM intracellular 2GBI (black circles), or by 500 μM extracellular 2GBI (gray diamonds). Solid bars indicate the presence of the inhibitor in the bath during measurements performed in inside-out (black), or outside-out (gray) patch configuration. **(C)** Average inhibition produced by the indicated compounds (numbers as in Fig. 1) added intracellularly (200 μM). **(D)** Dose dependence of 2GBI inhibition for proton channels of the indicated species. Curves are Hill fits of the data points (see Table S2.1). **(E)** G-V relationships for human Hv1 in the presence and absence of 200 μM 2GBI (pH_i = pH_o = 6.0.). Teal and red curves are Boltzmann fits (see Table S2). Gray line is the G-V in the presence of the inhibitor normalized to the control maximal conductance (no inhibitor). **(F)** Effect of extracellular pH on proton channel inhibition by 50 μM intracellular 2GBI (pH_i = 6.0). Error bars are ± s.e.m., n ≥ 4.

To determine whether the binding site for 2GBI is located in a structurally conserved part of the protein we compared the dose dependence of inhibition of the human channel to the dose dependences of inhibition of Ci-VSOP, the channel from the tunicate *Ciona intestinalis* (Sasaki et al., 2006), and Eh-HVCN1, the channel from the coccolithophore *Emiliana huxleyi* (Taylor et al., 2011) (Fig. 2.2D and Table S2.1). Ci-VSOP and Eh-HVCN1 conduct protons

through their VSDs like the human Hv1, and they are 27% and 18% identical to the human protein, respectively. Despite some differences in IC_{50} (38 μM for the human Hv1, 52 μM for Ci-VSOP, and 87 μM for Eh-HVCN1), 2GBI was able to completely inhibit the three channels within similar concentration ranges indicating that the binding site has been maintained over evolution. Given the higher sensitivity of the human Hv1 for 2GBI, we continued our study of the mechanism of inhibition with this channel.

2.3.2 2GBI interaction with the open VSD

We then asked whether 2GBI acts as an allosteric modulator like other known Hv1 inhibitors (Alabi et al., 2007; Decoursey and Cherny, 2007), or as a channel blocker. If 2GBI inhibits the Hv1 current by making channel opening more difficult, its binding should alter the channel's voltage dependence of activation. We verified this by comparing the G-V curves of Hv1 in the presence of 200 μM 2GBI and in the absence of the inhibitor. The curves were obtained from tail current measurements as previously described (Musset et al., 2008; Tombola et al., 2010) and were found to be superimposable (Fig. 2.2E and Table S2.2). The finding that 2GBI reduces the channel's maximal conductance without altering its G-V curve and the observation that channels already opened by depolarization can be quickly inhibited by fast application of 2GBI (Fig. S2.2A – B) are consistent with a mechanism of inhibition in which 2GBI blocks open channels. We also found that the efficiency of Hv1 block by intracellular 2GBI increased when the concentration of protons on the extracellular side of the membrane decreased (higher pH_o) (Fig. 2.2F) suggesting that the blocker binds in the channel's pore where it can interact with permeating protons.

To gain more insight on whether 2GBI has access to the proton permeation pathway inside the VSD, we analyzed the effects of the transmembrane electric field and extracellular protons on 2GBI inhibition.

Because of its positive charge, 2GBI is expected to be sensitive to the transmembrane electric field when binding to the channel. This means that its dissociation constant (K_d) should depend on the membrane potential. We determined the voltage dependence of K_d by measuring the proton current carried by maximally open channels in the presence of 50 μM 2GBI at different membrane potentials (Fig. 2.3A – B), and by using as reference the K_d measured from the dose response curve of Fig. 2.2D at +120 mV (see Supplemental Procedures, eqs. S2.4 – S2.5). From the exponential fit of the K_d-voltage relationship the parameter δz_b (effective charge) of 0.35 ± 0.1 was calculated (see Supplemental Procedures, eq. S2.6), which provides an estimate of the maximal fraction of the transmembrane electric field that the blocker must cross in order to reach its binding site inside the channel(Woodhull, 1973). Considering a relative drop in membrane potential from 1 to 0 across the entire Hv1 proton permeation pathway, a δz_b of 0.35 means that the charged 2GBI molecule (z_b = +1) experiences up to 35% of the total electric field when moving in and out of the proton pore.

If 2GBI binds the VSD on the intracellular side of the permeation pathway, protons entering the channel from the extracellular side are expected to facilitate blocker unbinding. Accordingly, an increase in extracellular proton concentration (decrease in pH_o) is expected to cause an increase in the rate of blocker unbinding at negative potentials,

resulting in a faster decay of the tail current. To test the effect of extracellular protons on blocker unbinding, we compared the decays of the tail current at -40 mV measured at two different extracellular pHs (Fig. 2.3C). We first determined the pH_o-dependence of channel closing by measuring the ratio between the time constants of current decays at pH_o 7.5 and 6.0 in the absence of the blocker ($\tau_{7.5}/\tau_{6.0} \sim 1.5$). Then, we determined the pH_o-dependence of channel unblocking by similar measurements carried out in the presence of 200 μM 2GBI in the intracellular solution (see Supplemental Procedures). As expected, we found that increasing the extracellular proton concentration significantly shortens the decay time of the tail current in the presence of the blocker ($\tau_{7.5}/\tau_{6.0} \sim 2.6$) (Fig. 2.3D). This is consistent with blocker unbinding facilitated by extracellular protons in the permeation pathway.

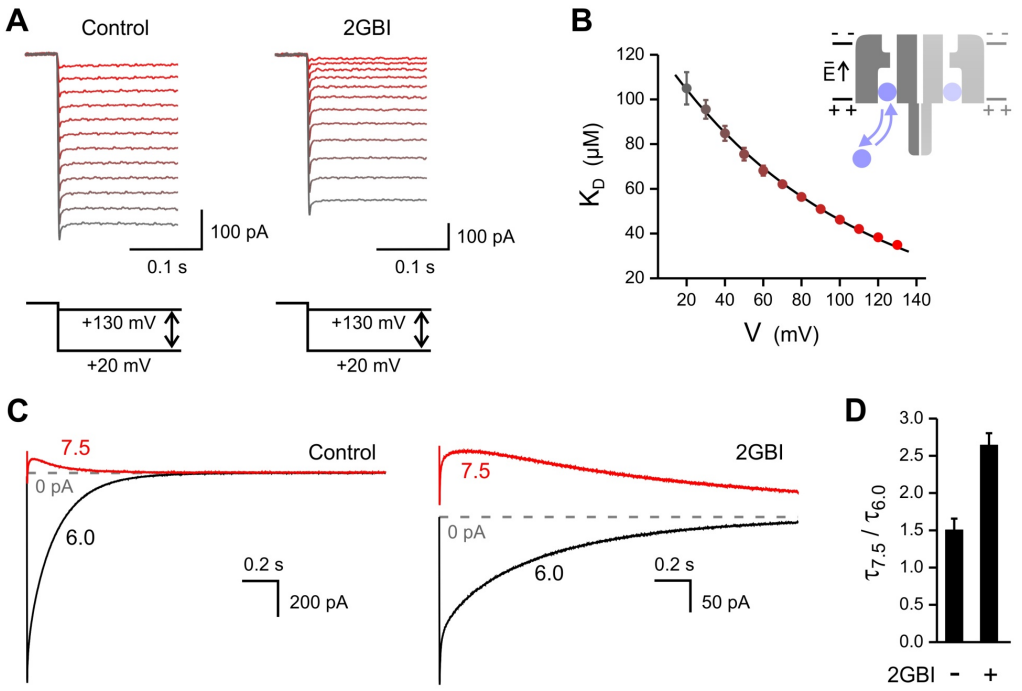

Figure 2.3. 2GBI binding and unbinding depend on membrane potential and extracellular proton concentration. (A) Proton currents from Hv1 channels measured in inside-out patches in the absence of blocker (Control) and in the presence of 50 μM 2GBI in the bath solution (pH_i = pH_o = 6.0). Patches with similar current levels were selected for the comparison and scaled to match the maximal current. A

depolarization to +140 mV was followed by a step to a progressively lower voltage, in 10 mV decrements. Holding potential was -80 mV. The color of the traces transitions from gray to red as the test voltage becomes more positive. **(B)** Dissociation constant of 2GBI block as a function of membrane potential, calculated from proton currents recorded using the voltage protocol described in (A). Error bars are ± s.e.m., n = 6. The exponential fit of the data is shown as black line. **(C)** Hv1 tail-currents measured from two outside-out patches in response to a voltage step to -40 mV from a preceding depolarization at +120 mV (not shown). pH_i was 6.0. For each patch, currents were measured at a pH_o of 6.0 and 7.5. Traces on the right were measured in the presence of 200 μM 2GBI in the intracellular (pipette) solution. **(D)** Average values of the ratio of time constants of current decay measured at pH_o = 7.5 and 6.0, from traces like those reported in (C). Time constants were calculated from multi-exponential fits of current decays. A $\tau_{7.5}/\tau_{6.0} > 1$ means that the decay is faster when the proton concentration is higher on the extracellular side of the pore.

2.3.3 F150 plays a key role in 2GBI binding

Since 2GBI appears to bind the Hv1 channel somewhere along the permeation pathway, we planned to use it to shed light on the location of the pore. We wondered whether we could find residues in the channel that, when mutated, would strongly affect 2GBI binding. We had previously identified a mutant of the Shaker potassium channel that conducts ions - including guanidinium - through its VSD (Tombola et al., 2005) and had found several residues that are likely to line the Shaker VSD pore (Tombola et al., 2007). We hypothesized that among the Hv1 residues homologous to those involved in ion permeation in the Shaker VSD there could be some that face the proton pore and participate in the binding of 2GBI. Of all the Shaker mutations tested for their impact on the ion current (omega current) flowing through the VSD, those at position F290 produced the strongest effect (Tombola et al., 2007). In addition, F290 was proposed to be part of the occlusion (charge transfer center) that prevents ions from flowing through non-conducting VSDs (Tao et al., 2010). The Hv1 residue F150 corresponds to the Shaker F290. The phenylalanine is located deep within the membrane in the S2 helix, and it is highly conserved in the VSDs of voltage-gated ion channels and voltage dependent phosphatases.

We mutated F150 to several other residues and found that the alanine substitution produced a ~360-fold increase in binding affinity for 2GBI (Fig. 2.4, and Table S2.1). The cysteine substitution also increased the affinity for the blocker, but to a lesser extent (Fig. 2.4C). On the other hand, the dose dependence of block of Hv1 F150W was very similar to the wild type channel (Fig. 2.4C). These findings show that the nature of the side chain at position 150 strongly affects the strength of the interaction between the channel and 2GBI.

In Shaker, mutations at position F290 were found to alter the voltage dependence of gating, producing shifts in the conductance versus voltage relationship (G-V curve), and alterations of the gating charge movement in the VSD (Lacroix and Bezanilla, 2011; Tao et al., 2010). We determined the G-V curves of Hv1 F150A, F150C, and F150W and compared them to the G-V of the wild type (WT) channel (Fig. 2.4B, Table S2.2). We found that mutation F150W produced the strongest perturbation of channel gating (largest G-V shift compared to WT), and yet it had almost no effect on 2GBI binding. In contrast, mutations F150A and F150C produced different effects on 2GBI binding, but the same effect on channel gating (very similar G-V curves). We conclude that there is no correlation between the alterations of channel gating and affinity for the blocker produced by F150 substitutions. This suggests that the mechanism by which F150 mutations alter 2GBI binding is distinct from the mechanism by which they alter the movement of the voltage sensor.

2.3.4 Selectivity of the perturbations of F150 substitutions

We examined whether the increase in affinity for 2GBI resulting from mutations at position 150 was dependent on the structure of the inhibitor. We compared the relative block of F150A and wild type channels by 2GBI to the relative block of the same two channels by other two intracellular inhibitors: guanidinium and magnesium. Guanidinium was selected for the comparison because it lacks the 2GBI structural feature provided by the benzimidazole group. Magnesium was selected because it was found to inhibit the Hv1 proton current despite being structurally unrelated to 2GBI and guanidinium. We found that, while there is a large difference in binding affinity for 2GBI between F150A and wild type channels, there is a much smaller difference for guanidinium and no difference for magnesium (Fig. 2.4D).

We also examined the inhibition of F150A, F150C and wild type channels by GBOZ (compound 11 in Fig. 2.1). This inhibitor is very similar to 2GBI in structure, but it is a weak blocker like magnesium (both GBOZ and magnesium have IC_{50}s close to 9 mM). We found that the F150A and F150C mutations altered the affinity of the channel for GBOZ in the same way that they altered the affinity for 2GBI (Fig. 2.4E). This shows that the nature of the side chain of residue 150 affects the interaction between the channel and the inhibitor in a selective manner, with 2GBI and closely related compounds being affected the most.

2.3.5 Opening of an intracellular gate is required for 2GBI binding

When Hv1 wild type is treated with 2GBI, the proton current is inhibited, and the apparent rate of channel deactivation is slowed down, producing a more persistent inward current at negative voltages after depolarization (Fig. 2.2A and Fig. S2.2C). A similar phenomenon is observed with other voltage-gated ion channels when their pore domain interacts with intracellular blockers. When the intracellular activation gate of the pore domain is closed, blockers are prevented from reaching a binding site located in the core of the permeation pathway. If the channel opens and the blocker is allowed to bind, the gate cannot close until the blocker unbinds. This is referred to as *foot in the door* effect (Yeh and Armstrong, 1978), and it is also seen with the inactivation ball of some fast inactivating channels (Hille, 2001). The apparent rate of channel deactivation is slowed down by the *foot in the door* effect because the gate cannot close right away upon membrane repolarization and must instead wait for the blocker (or the inactivation ball) to first vacate the pore.

The *foot in the door* effect of 2GBI on the Hv1 deactivation rate suggests that there is an intracellular gate in the VSD also. However, when channels with intracellular gates are opened in the presence of a blocker, the time course of current activation usually displays a biphasic behavior. Upon depolarization, the current first raises, reaches a maximum, and then falls to a steady state level that depends on the affinity and concentration of the blocker. This is observed, for example, when voltage-gated potassium channels are blocked by intracellular quaternary-ammonium inhibitors (Armstrong, 1968; 1971; Choi et al., 1993), or by the inactivation ball (Armstrong and Bezanilla, 1977; Demo and Yellen, 1991;

Zagotta et al., 1990). The biphasic behavior is a direct result of gate opening. At the beginning of the depolarization, most channels are closed and cannot bind the blocker. Open channels are generated faster than they are blocked and the current increases. Over time, as the pool of closed channels decreases, the production of open channels slows down and the blocking process becomes dominant, with consequent decrease in the current.

When 2GBI inhibits Hv1 wild type, there is no sign of a biphasic behavior in the activation current (Fig. 2.2A). The proton current increases upon depolarization with similar kinetics in the presence and in the absence of the blocker. However, when 2GBI inhibits Hv1 F150A, it produces a strong change in the kinetics of the activation current, which becomes clearly biphasic (Fig. 2.4A). This, in combination with the prominent slowdown of the deactivation current, provides strong evidence for the regulation of 2GBI block by an intracellular gate. (Fig. 2.4G).

The behavior of Hv1 F150A also helps explain why 2GBI does not affect the kinetics of activation in the wild type channel. The slow opening process in Hv1 WT does not allow a transient accumulation of open channels in the presence of 2GBI. The channels simply get blocked as soon as they open, making it impossible for the current to display the biphasic time course. The F150A mutation changes all this, directly, by speeding up the opening process (compare time scales in Fig. 2.2A and Fig. 2.4A), and indirectly, by lowering the concentration of 2GBI required for inhibition (increased affinity), which results in a slower rate of channel block.

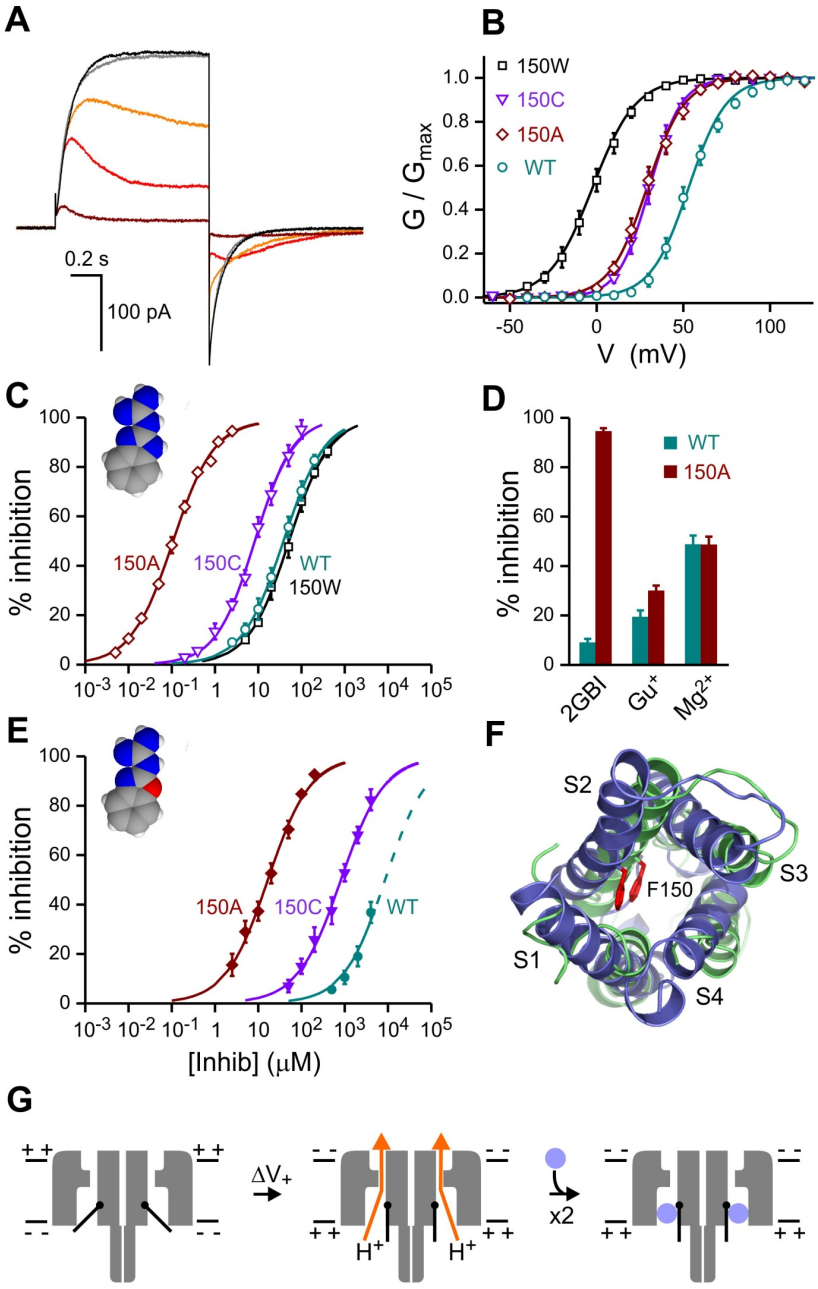

Figure 2.4. Effects of F150 substitutions on Hv1 voltage-dependence and inhibition by intracellular blockers. (A) Proton currents measured from F150A Hv1 channels in response to depolarizations to +120 mV from a holding potential of -80 mV (pHi = pHo = 6.0.). After recording the current from an inside-out patch in the absence of the inhibitor (black trace), 2GBI (2 μM) was added to the bath solution (dark red trace) and then removed by bath perfusion (gray trace). Red and orange traces show partial recovery from block during inhibitor washout. **(B)** Conductance versus voltage relationships for the indicated F150 mutants compared to WT (see Table S2.2). **(C)** Dose dependence of 2GBI inhibition of F150A, F150C, and F150W channels compared to WT. Curves are Hill fits (see Table S2.1). **(D)** Inhibition of Hv1 F150A and WT by 1 μM 2GBI, compared to inhibition by guanidinium (500 μM) and magnesium (7.9 mM). **(E)** Dose dependence of inhibition by 2GBOZ (compound #11) of F150A and F150C channels compared to WT. Curves are Hill fits (see Table S2.1). Extrapolation of the WT inhibition curve at concentrations higher than the solubility limit of 2GBOZ is shown as dashed line. Error bars are ± s.e.m., n ≥ 4 (not shown when smaller than symbols). **(F)** Location of phenylalanine 150 (red side chain) in the two structural models of the Hv1 VSD from Wood et al.

2011 (R1-model in green, and R2-model in blue). The models were superimposed by distance minimization of the alpha carbons of the S1 segments (residue 99 to 123). The VSD is shown from the intracellular side of the membrane plane. **(G)** Interpretation of the result shown in (A) as state dependent block regulated by the opening of an activation gate.

2.3.6 Coupling between gates in the two Hv1 subunits

To further investigate the interaction between 2GBI and the Hv1 intracellular gate, we examined the recovery from block of the F150A mutant with a two-pulse voltage protocol (Fig. 2.5A). The current measurements were performed in inside-out patches and in the presence of 400 nM blocker in the bath solution. The channels were opened and blocked with the first depolarization pulse. They were then unblocked by applying a negative voltage, and the fraction of recovery from block was tested with a second depolarization pulse. The time between the two pulses (t_{IP}) spent at negative voltage was varied to capture the time course of recovery (Fig. 2.5A – C). This was determined by reporting the relative increase in peak current at the test pulse as a function of t_{IP}.

When t_{IP} is short, only a few channels have the time to recover from block before the second depolarization. This is expected to result in a peak current in the second pulse similar in magnitude to the current at the end of the first pulse. When t_{IP} becomes longer, the channels have more time to recover and the peak current in the second pulse should gradually increase until there is no more difference between the first and second peaks (complete recovery). This is the typical behavior of current recovery from block/inactivation observed in voltage-gated channels with pore domains. But, Hv1 F150A recovers from 2GBI block in a significantly different way. As t_{IP} increases, the second peak

increases very fast and reaches a maximum value that is higher than the first peak. Then, at longer t_{IP}, the second peak slowly decays to reach the value of the first peak (Fig. 2.5A & C). In addition, the recovery peak currents measured at short and long t_{IP} display very different kinetics of opening and block (compare peaks 1 and 2 in Fig. 2.5D, and values of τ_{decay} in Fig. 2.5E). If the recovery peaks were produced only by the opening of non-blocked channels, they should only change in size as a function of t_{IP}, but their kinetics should stay the same. The difference in kinetics indicates that different populations of channels are responsible for the recovery peaks at short t_{IP} versus long t_{IP}. The significant delay between the time at which the recovery peaks reach their maximum and the time at which the tail current is maximal (Fig. 2.5A and Fig. S2.5A) suggests that a significant fraction of the recovery current comes from a population of channels that are not able to conduct current at negative potentials but can become conductive very rapidly at positive potentials.

While voltage-gated sodium, potassium, and calcium channels contain one activation gate in the pore domain, Hv1 is made of two subunits which can gate cooperatively (Fujiwara et al., 2012; Gonzalez et al., 2010; Musset et al., 2010; Tombola et al., 2010). We considered that the presence of two coupled gates in Hv1 could be the reason for its peculiar recovery from block. We first tested this hypothesis by examining the recovery from block of monomeric Hv1 F150A. Monomerization was achieved as previously described by replacing Hv1 intracellular N and C termini with the corresponding parts of Ci-VSP (Tombola et al., 2008). We found that the N_{VSP}-Hv1-C_{VSP} F150A chimera recovers from block similarly to channels with pore domains, with the current of the second peak gradually rising to the level of the first peak as t_{IP} increases (Fig. 2.5B – C). Moreover, the

kinetics of opening and block of the recovery peaks measured at short and long t_{IP}s were the same in monomeric channels (Fig. 2.5D – E).

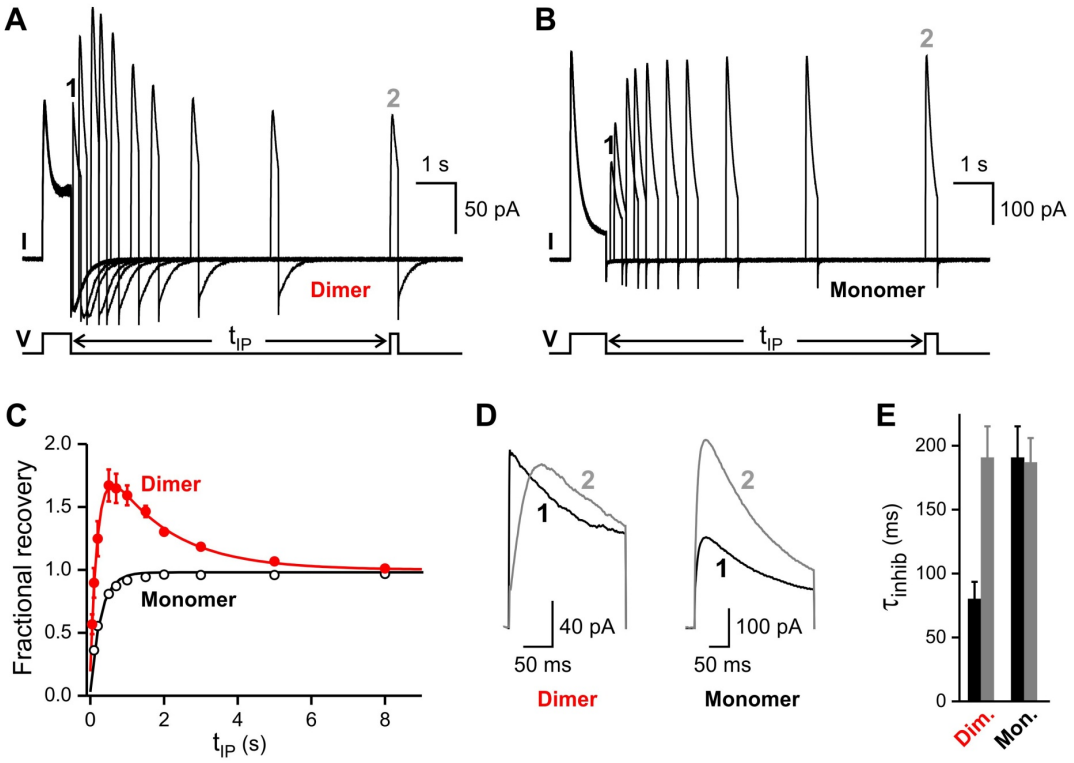

Figure 2.5. Recovery from block of Hv1 F150A: dimer vs. monomer. (A) Proton currents from F150A Hv1 channels in the presence of 400 nM 2GBI measured in response to the indicated two-pulse voltage protocol. The time interval between depolarization pulses (t_{IP}) was progressively increased from 0.05 s to 8 s. The trace recorded with the shortest t_{IP} is not displayed for clarity. The voltage was stepped from -60 mV to +140 mV in both pulses. Holding potential between sweeps was -80 mV. **(B)** Proton currents from monomeric F150A N_{VSP}-Hv1-C_{VSP} chimera, measured under the same conditions as in (A). **(C)** Fractional recovery from block as a function of t_{IP} calculated from peak currents measured as shown in (A) and (B). Red filled circles are for F150A Hv1. Black open circles are for the F150A N_{VSP}-Hv1-C_{VSP} chimera. Red line is a double-exponential fit of the data points for the dimer. Black line is a mono-exponential fit of the data points for the monomer. **(D)** The first and last recovery peaks marked as 1 and 2 in (A) and (B) (t_{IP} = 0.2 s and 8 s, respectively) are compared. The peaks are superimposed and magnified to show their kinetics. **(E)** Apparent time constants of 2GBI block during the second pulse of two-pulse protocols. The constants were measured by mono-exponential fit of the decaying current in recovery peaks 1 (black columns) and 2 (gray columns). Error bars are ± s.e.m., n ≥ 4.

2.3.7 Models of channel block in dimeric and monomeric Hv1

We examined the recovery from block by simulating the gating process in the presence of 2GBI with kinetic schemes involving one gate (monomer) (Fig. 2.S3), or two coupled gates (dimer) (Fig. 2.6). We assumed that each subunit can exist in 3 different states: closed (C), open (O), or blocked (B). This produces a total of 9 states in dimeric channels: CC, OC (equivalent to CO), OO, BO (equivalent to OB), BC (equivalent to CB) and BB (Fig. 2.6A). Since we found that 2GBI must wait for the activation gate to open in order to block the channel, we assumed that the blocked state can only be reached from the open state in each individual subunit.

We had previously established that the opening of one Hv1 subunit strongly facilitates the opening of the other subunit (Tombola et al., 2010). We found that the inclusion of facilitated opening in the kinetic model of dimeric Hv1 was required to reproduce the observed time course of recovery from block. This was accomplished by making opening transitions from states with one gate already open (e.g., OC → OO, and BC → BO) faster than equivalent transitions from states with both gates closed (e.g., CC → OC). In order to reproduce the experimental findings, the model needed to include also the following properties of channel block: 1) when the blocker is bound to one subunit, the gate of that subunit cannot close (*foot in the door*), and 2) if the gate of an unblocked subunit happens to close while the neighboring subunit is still bound to the blocker, it becomes significantly harder for that blocker to unbind. The first property was represented in the model by excluding transitions of the type BX → CX (with X = C, O, or B). The second property was

represented by a slower rate of unblocking in dimers with one closed subunit (e.g., BC → OC) compared to the rate of unblocking in dimers with two open or blocked subunits (e.g., BO → OO, BB → OB).

We found that the kinetic model shown in Fig. 2.6A and Fig. S2.4 can reproduce the major features of channel block and recovery from block of dimeric F150A Hv1. It can also be simplified to reproduce the observed behavior of monomeric channels (Figs. S2.3 & 2.4). The simplified model features only three states (C, O, and B), loses the properties connected to the cooperative gating between subunits, but maintains the general feature of the *foot in the door* mechanism of block.

Using the kinetic model for the F150A dimeric channel, we were also able to reproduce the behavior of 2GBI block in the wild type channel (Fig. 2.6D). Hv1 wild type is characterized by a slower rate of opening and a lower affinity for 2GBI compared to the F150A mutant. To account for these differences, adjustments in the rates of opening and block were necessary (see Fig. S2.4). When we reduced the rates of opening and adjusted the rates of blocking and unblocking to account for the higher concentration of 2GBI required for block, the biphasic time course of the simulated current of F150A channels (Fig. 2.6D, left panel) turned into the simpler time course of the wild type current (Fig. 2.6D, right panel).

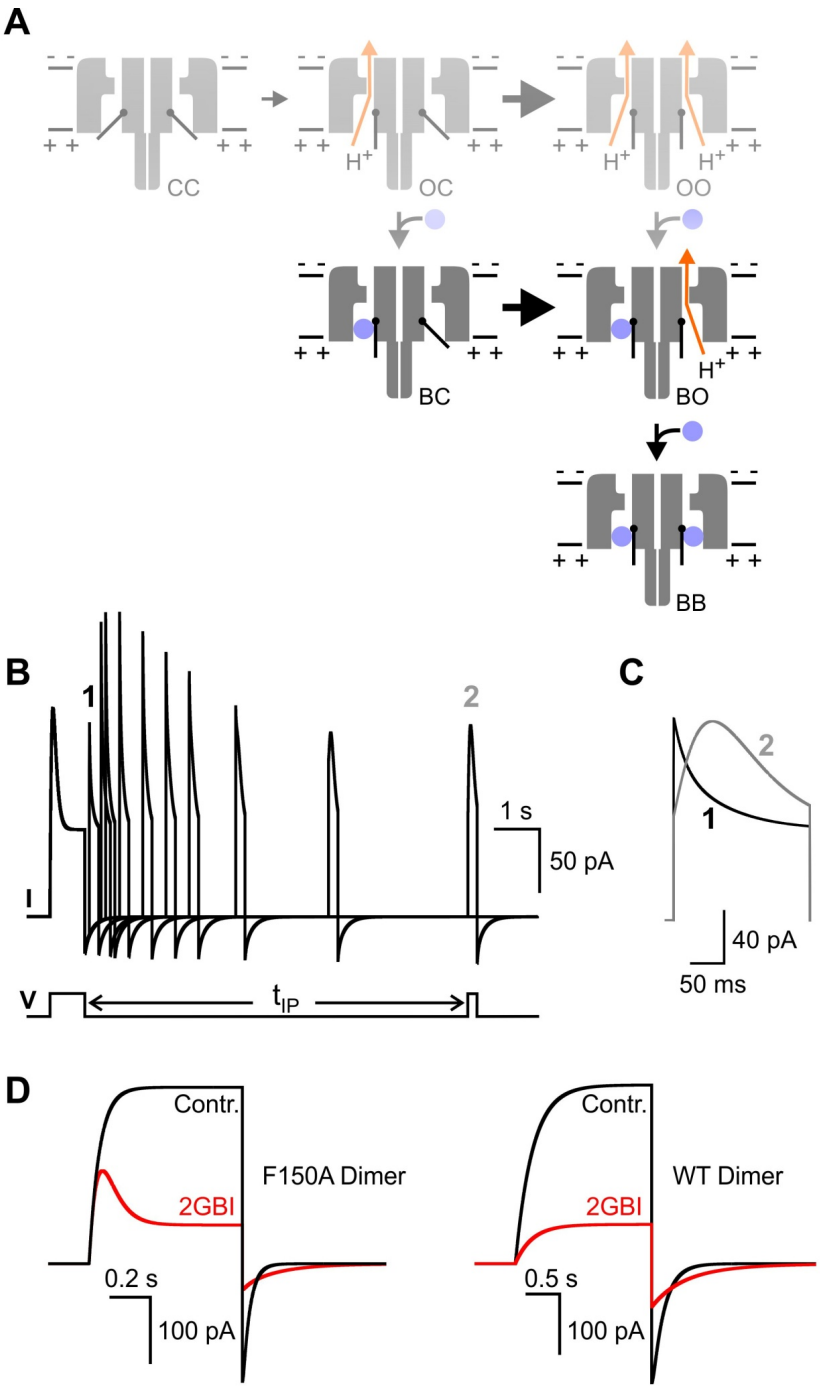

Figure 2.6. Model of Hv1 opening and block mediated by two coupled intracellular gates. (A) States of the two gates of the Hv1 dimer during opening. CC: close-closed, CO: closed-open, CB: closed-blocked, OO: open-open, BO: blocked-open, BB: blocked-blocked. Only forward reactions favored at positive potentials are shown for clarity. **(B)** Simulation of currents from modeled F150A dimeric channels generated under conditions equivalent to those reported in Fig. 2.5A. The currents were generated using the kinetic rates reported in Fig. S2.4. **(C)** Superimposition of the first and last recovery peaks marked as 1 and 2 in (B). For analogous simulations of currents from F150A monomeric channels see Figs. S2.3. **(D)** Simulated currents from the indicated channels in response to a depolarization step to +120 mV from a holding potential of -80

mV before and after the addition of 2GBI (400 nM for Hv1 F150A and 200 μM for Hv1 WT). The currents were generated with the same kinetic model but with different rate constants to account for the slower gating, lower 2GBI binding affinity, and faster blocking and unblocking of the WT channel compared to the F150A mutant (see Fig. S2.4).

2.3.8 State-dependent release of 2GBI from dimeric Hv1

An important feature of 2GBI block highlighted by the modeling of Hv1 dimers is that, once a subunit releases its blocker, the state of its gate determines the fate of the blocker in the neighboring subunit. If the gate is open, the blocker in the other subunit is released quickly. If the gate is closed, the blocker is release slowly. We call this phenomenon *hemichannel blocker trapping* because the closing of one subunit (hemichannel formation) "traps" the blocker in the neighboring subunit. The trapping of the blocker was critically important for the simulation of the recovery from block of F150A dimers (Fig. S2.4). We found that only models in which the BC → OC transition was much slower than the BO → OO transition (blocker trapping in BC dimers) were able to describe the experimental data. The rate of the BC → OC transition at negative potential was the parameter with the largest effect on the heights and shapes of the recovery peaks as a function of t_{IP}.

2GBI slows down the tail currents of Hv1 channels by causing a delay in gate closure. The contribution of hemichannel blocker trapping to this delay depends on the fraction of BC dimers generated. Our model indicates that the fraction of BC dimers formed at negative potentials is higher in F150A channels compared to wild type channels because of the higher rate of blocker unbinding from wild type subunits. Fast unblocking means that both subunits can release their blockers before the gate in either subunit can close (Fig. S2.4).

This transiently produces dimers with two open subunits and limits the formation of BC dimers in wild type. The model also predicts that blockers with lower unbinding rate (higher binding affinity) than 2GBI will produce larger fractions of wild type BC dimers.

The features of the interactions between 2GBI and the VSD of Hv1 are similar to those previously described for open-channel blockers of pore domains. But, the trapping of the blocker in one subunit caused by gate closing in the neighboring subunit seems to be a unique feature of Hv1, due to the existence of two distinct activation gates on two allosterically coupled ion-permeable VSDs.

2.3.9 Blocker trapping tested in heteromeric F150A-WT channels

We tested the conclusion that the recovery from block of Hv1 channels is delayed by 2GBI trapping in BC dimers under experimental conditions in which the formation of BC dimers is maximized. To do this we maximized the fraction of BO dimers from which BC dimers are formed during the recovery from block at negative potentials. Generating large fractions of BO channels in wild type or F150A homodimers is difficult because, even at 2GBI concentrations that produce 50 % of channel block, significant fractions of dimers are in the OO and BB states at the end of the depolarization step. So, we generated linked heterodimers made of one F150A subunit and one wild type subunit, and exploited the large difference in 2GBI affinity between the two subunits to generate BO dimers. Based on the dissociation constants of 2GBI from F150A and wild type homodimers, we estimated that 2 μM 2GBI should block about 94% of the F150A subunits and 6% of the wild type

subunits at +120 mV, producing a ~50% total inhibition of the initial current (Fig. 2.7A). After the depolarization step to +120 mV, the membrane was repolarized with a voltage ramp from 0 to -80 mV, and the time course of the tail current was recorded before and after addition of 2GBI (Fig. 2.7B).

The number of open subunits decreases over time after the end of the depolarization step due to gate closing. However, the current flowing through each individual open subunit increases during the ramp, due to the increased electrical driving force for proton movement. These two opposing factors determine the position and size of the negative peak of the tail current. We reasoned that if the blocker was trapped in BC dimers, its slow release would delay the formation of open hemichannels (OC) during the voltage ramp. These hemichannels would conduct more current than those formed at the beginning of the ramp and would cause the peak of the tail current to increase in size and to shift its position to more negative voltages. We indeed observed an increase in the tail current produced by 2GBI in the F150A-WT dimers and a right shift in the position of the peak (Fig. 2.7B).

We then repeated the same kind of measurements in WT-WT linked dimers using a 2GBI concentration of 40 μM to inhibit 50 % of the current at +120 mV (Fig. 2.7C –D). We observed a small reduction in the tail current during the repolarization ramp induced by the blocker and a small shift of the peak toward more negative potentials (Fig. 2.7D). This is in agreement with the idea that the fraction of BC dimers produced from BO dimers in WT-

WT channels is reduced due to the competition of the process that converts BO dimers into OO dimers (Fig. 2.7C).

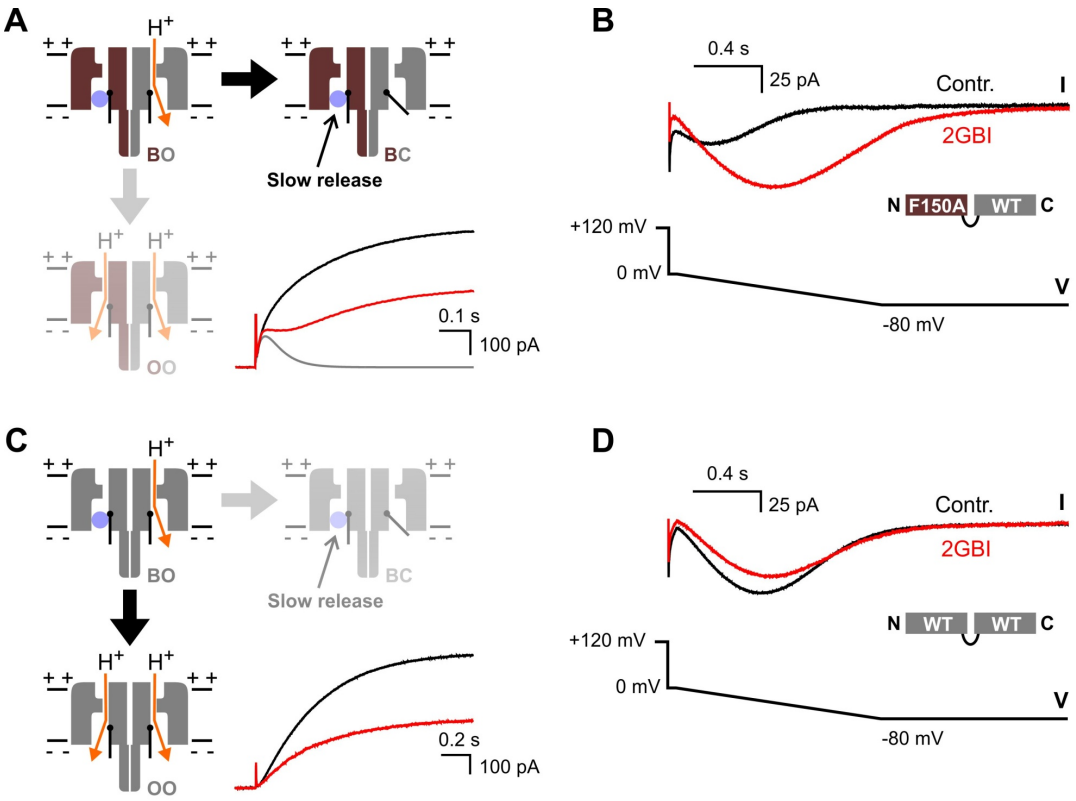

Figure 2.7. ***Hemichannel blocker trapping*** **for 2GBI tested in a heterodimeric Hv1 channel. (A)** Partial 2GBI block of linked heterodimers made of one F150A subunit (dark red) and one WT subunit (gray). Currents traces from an inside-out patch containing F150A-WT dimers. Channels were opened by depolarization to +120 mV (from -80 mV holding potential) in the absence of the inhibitor (black trace), and in the presence of 2 μM 2GBI (red trace) in the intracellular solution (pH_i = pH_o = 6.0). Gray line is the predicted current contributed by the F150A subunit after 2GBI addition, obtained by multi-exponential fitting of the total current measured in the presence of blocker (red trace). At the end of the depolarization the large majority of channels are in the BO state when 2GBI is present. Upon membrane repolarization BO channels can be converted to either BC or OO channels. Black arrow indicates favored conversion. **(B)** Tail currents from linked dimers measured in response to the indicated voltage ramp after the depolarization step described in (A). **(C)** Partial 2GBI block of linked WT-WT homodimers. Currents traces were measured under the conditions described in (A) but using 40 μM 2GBI. At the end of the depolarization step the channels are distributed among the BB, OO, and BO/OB states. Upon membrane repolarization the conversion from BO channels to OO channels is favored (black arrow). **(D)** Tail currents from linked WT-WT dimers measured in response to the indicated voltage ramp after a depolarization step to +120 mV (same conditions described in C).

2.4 Discussion

Compounds that act as inhibitors of pore domains have been used for decades to investigate the permeation and gating mechanism of voltage-gated sodium, potassium, and calcium channels (Hille, 2001). For example, the use of open channel blockers such as quaternary ammonium ions and cationic derivatives of local anesthetics led to the discovery that the activation gate of these channels faces the inner side of the membrane e.g., (Armstrong, 1971; Holmgren et al., 1997; Narahashi et al., 1969). Here we find that some heteroaromatic guanidine derivatives are effective inhibitors of the Hv1 proton channel, and show that one of these compounds, 2GBI, acts as an open channel blocker of the VSD.

The voltage dependence of VSD block by intracellular 2GBI and the effect of extracellular protons on the rate of blocker unbinding indicate that the binding site for 2GBI is located in the channel's permeation pathway. The finding that the channel's affinity for the blocker depends on the nature of the side chain at position 150 in the core of the VSD supports this conclusion, which is also in agreement with the recent finding that non-derivatized guanidinium ions can permeate the Hv1 channel when one of its S4 arginines (R211) is mutated to a different amino acid (Berger and Isacoff, 2011). From the analysis of channel block in Hv1 WT and F150A we found that 2GBI needs to wait for the opening of an intracellular gate in order to gain access to the permeation pathway in the VSD, and that as long as the blocker is bound to its receptor, the gate cannot close. The increased affinity of the F150A channel for 2GBI and its faster kinetic of activation allowed us to investigate the

recovery from block of dimeric and monomeric forms of Hv1. We found that when the open subunit of BO dimers closes, producing BC dimers, the release of 2GBI from the blocked subunit becomes substantially slower, as if the blocker was trapped inside the channel (*hemichannel blocker trapping*). We then analyzed the effect of 2GBI on the tail currents of F150A-WT linked dimers to confirm the delayed release of the trapped blocker.

Relative stability of Hv1 conformations and blocker trapping

The results of our simulations of Hv1 block support the idea that conformations in which the gates of the two subunits are out of sync (e.g., OC, and BC) are less stable than the conformations in which the gates are in sync (e.g., OO, CC, and BB). The energetic bias toward in-sync conformations could be due to mechanical stress between the two gates when one is open and the other is closed, and can provide an explanation for the observed cooperativity between subunits during gating of Hv1 dimers (Fujiwara et al., 2012; Gonzalez et al., 2010; Musset et al., 2010; Tombola et al., 2010). The phenomenon of *hemichannel blocker trapping* can then be interpreted as a result of block-induced stabilization of BC dimers. In these dimers, the gate in the blocked subunit cannot close, forcing the two subunits to be out of sync. But, the blocked subunit can change conformation to increase the affinity for the blocker (~8 fold), and the stabilization of the channel associated with the tighter block can compensate for the destabilization caused by the stress between gates. This suggests that blockers capable of producing a strong stabilization of the hemichannel would be able to stay bound for a long time after channel activation, causing use-dependent cumulative block.

Relationship between F150 the Hv1 selectivity filter and the gate

Unlike other ions, protons can move in aqueous solutions and within channel proteins via proton-hoping mechanism (Decoursey et al., 2003). The exact role played in proton-hopping by water inside the VSD (Ramsey et al., 2010; Wood et al., 2012) and by charged residues lining its pore is not well understood. But, recent studies have identified an aspartate in the middle of the S1 segment and the third S4 arginine (residues D112 and R211 in the human Hv1) as two key players in the ion selection mechanism (Berger and Isacoff, 2011; Musset et al., 2011). The region containing these two residues is likely to be the narrowest part of the permeation pathway.

Here we find strong evidence that 2GBI binds in proximity of phenylalanine 150 in the S2 segment when blocking the proton pore. Different structural models of the Hv1 channel suggest that F150 is located just below D112 and R211 (or R3) in the core of the VSD (Ramsey et al., 2010; Wood et al., 2012), in other words, below the narrowest part of the permeation pathway. F150 corresponds to residue F233 in the Kv1.2-2.1 paddle chimera (Long et al., 2007). In the crystal structure of the potassium channel, F233 is located right on top of a cluster of tightly packed residues in which the fifth S4 charge (K5) interacts with two acidic residues in S2 and S3. Our findings suggest that in the Hv1 open conformation the corresponding cluster of tightly packed residues below the conserved phenylalanine is replaced by a vestibule large enough to accommodate the 2GBI blocker. This structural feature may be due to the lack of the fourth and fifth S4 charges in Hv1 and it is consistent

with the idea that the narrowest part of the permeation pathway of the Hv1 channel –the selectivity filter– is located above F150, toward the extracellular side of the membrane.

In the pore domain, the activation gate and the selectivity filter are located on opposite sides of the membrane and so they are separated by a relatively large distance. In the VSD, selectivity filter and gate are likely to be much closer in space given the smaller size of the domain and the proximity of F150 to D112 and R211. In this context, the state dependence of 2GBI block could derive from the widening of the edges of the intracellular vestibule in the open state, which would allow the blocker to interact with a deeper binding site. Alternatively, it could derive from the formation of the intracellular binding site in the open state by the gating machinery.

Conclusion

The intracellular cavity of the pore domain can accommodate blockers of large size, including bulky quaternary ammonium ions. The intracellular vestibule of Hv1 on the other hand seems to fit guanidine derivatives like a tight glove. Even small differences in the structure of the blocker result in large variations in binding affinity (e.g., 2GBI vs GBOZ). Intracellular quaternary ammonium ions like TMA^+ and TEA^+ do not inhibit the Hv1 channel (Musset et al., 2011; Ramsey et al., 2006), either because they cannot penetrate deep enough into the vestibule or because they lack the proper chemical properties for a tight binding. Exploring the specific interactions between guanidine derivatives and the

intracellular vestibule of the Hv1 VSD will help develop inhibitors with higher affinity and selectivity for the channel.

Recently, Hv1 was found to be highly expressed in breast cancer cells, and its knockdown by RNA interference was shown to strongly reduce cell proliferation and invasiveness (Wang et al., 2012; 2011). Hv1 was also found to be involved in NOX-mediated neuronal death during cerebral ischemia, and mice lacking Hv1 activity were shown to be protected from brain damage after stroke (Wu et al., 2012). These findings highlight the importance of understanding how Hv1 works at the molecular level and how it can be modulated or blocked by small molecules like guanidine derivatives. The development of high affinity inhibitors for Hv1 could lead to new chemotherapeutics, and treatments for ischemic stroke.

The VSDs of voltage-gated sodium and potassium channels do not conduct ions under physiological conditions, but they can become ion permeable as a result of mutations in the voltage sensor (Sokolov et al., 2005; Starace and Bezanilla, 2004; Tombola et al., 2005). Ion/proton currents flowing through one of the VSDs of mutated Nav1.4 channels have been found to be the cause of some periodic paralyses (Sokolov et al., 2007; Struyk and Cannon, 2007). Mutations of voltage-gated ion channels associated with other genetic diseases have been proposed to result in ion conducting VSDs (Sokolov et al., 2007). Determining how the Hv1 channel is gated and how it interacts with small molecules could help design drugs able to block “leaky” VSDs.

2.5 Supplementary Information

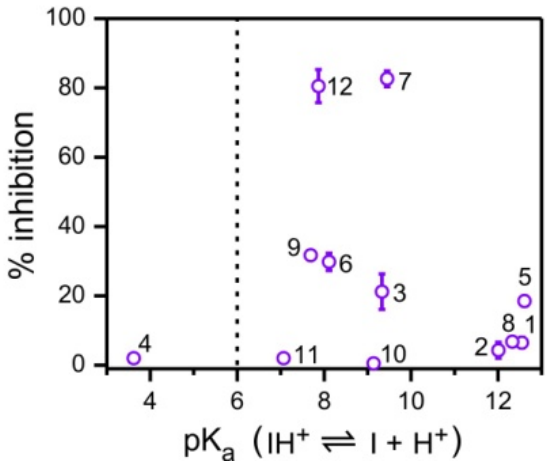

Figure S2.1. Inhibitions of tested compounds versus calculated pK_a values, related to Figure 2.2. Plot shows lack of correlation between inhibitor potency and pK_a. Dotted line indicates experimental pH value. Error bars are ± s.e.m. Compounds with pK_a > 6.0, are expected to be for the most part protonated.

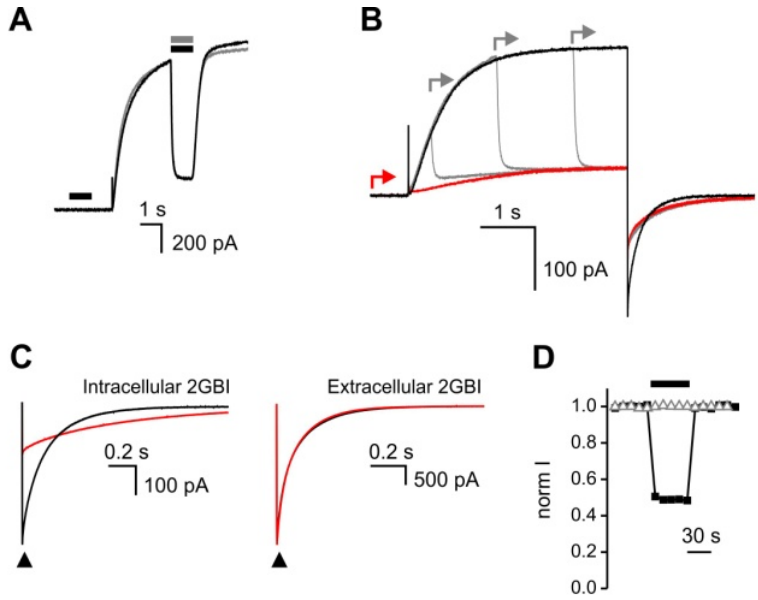

Figure S2.2. Effects of intra- and extracellular 2GBI on inward and outward Hv1 currents, related to Figure 2.2. (A) Inhibition of open Hv1 channels by transient application of 200 μM 2GBI to the intracellular side of the membrane. Filled bars indicate the presence of the inhibitor. Current traces were recorded from an inside-out patch at pH_i = pH_o = 6.0 during a voltage step from -80 mV to +120 mV. 2GBI was initially applied during the depolarization at +120 mV when most channels are open (gray trace and gray bar). Then, it was applied at -80 mV and at +120 mV (black trace and black bars). **(B)** Fast application of 2GBI during measurements similar to those shown in (A) but maintaining the perfusion of the inhibitor throughout the remaining part of each recording. Arrows indicate the start of 2GBI application (200 μM). The inhibitor was washed out between consecutive recordings. The black trace is the control without inhibitor. **(C)** Hv1 inward

tail currents measured at -80 mV after a depolarization step to +120 mV to open the channels. pH_i = pH_o = 6.0. Currents were recorded in the absence of the inhibitor (black) and in the presence of 200 μM 2GBI (red) applied to the indicated sides of the membrane. Traces displayed on the left panel are from an inside-out patch, currents displayed on the right panel are from an outside-out patch. Currents measured at the positions indicated by the black triangles (~30% decay of the initial control current) were reported over time to produce plots like the one shown in (D). **(D)** Inhibition of normalized Hv1 tail currents by 200 μM intracellular (black square) or extracellular (gray triangles) 2GBI. Solid bar indicates the presence of the inhibitor.

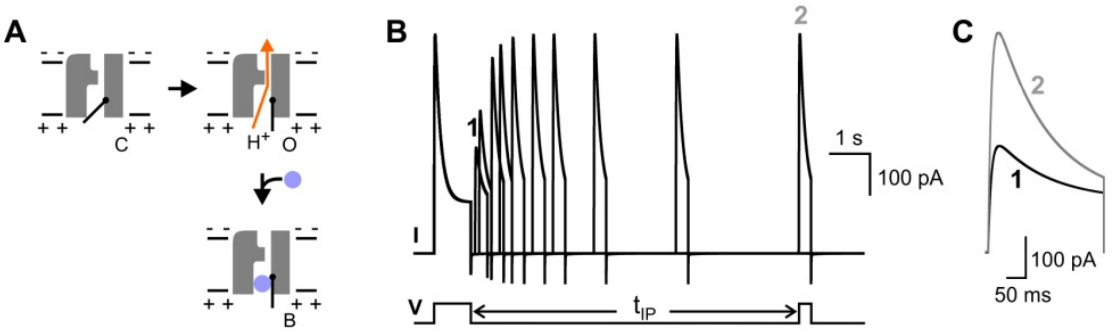

Figure S2.3. Simulations of block and recovery from block of the monomeric Hv1 channel, related to Figure 2.5. (A) Representation of the voltage-dependent opening of the monomeric F150A N_{VSP}-Hv1-C_{VSP} chimera channel in the presence of the intracellular blocker. C: closed, O: open, B: blocked. Only forward reactions favored at positive potentials are shown for clarity. **(B)** Simulation of currents from modeled monomeric channels generated under conditions equivalent to those reported in Fig. 2.5B, with Berkeley Madonna using the kinetic rates reported in Fig. S2.4. **(C)** Superimposition of the first and last recovery peaks marked as 1 and 2 in (B). Both peaks rise and decay with similar time course, consistent with experimental data in Fig. 2.5D.

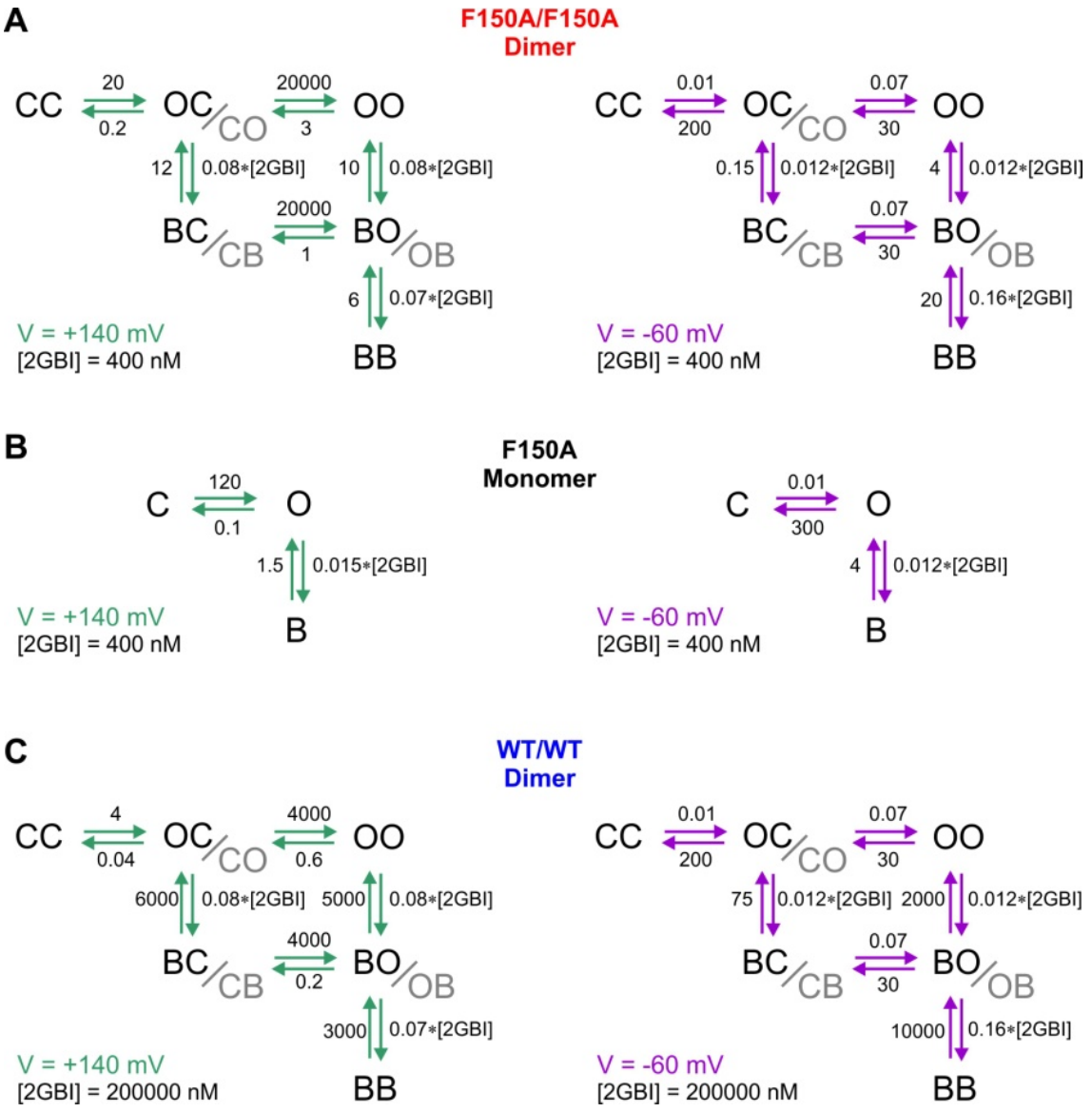

Figure S2.4. Rate constants used in modeling channel block, related to Figure 2.6. Parameters used in modeling of F150A/F150A hHv1 dimers **(A)**, F150A monomers i.e. F150A N_{VSP}-Hv1-C_{VSP} chimera **(B)** and WT/WT hHv1 dimers **(C)**. In each case left panels represent parameters at +140 mV and right panels represent parameters at -60 mV. Numbers next to arrows represent rate constants. For reactions involving 2GBI (vertical reactions) the concentrations of 2GBI are explicitly indicated. Rate constant units are s^{-1} for all horizontal reactions and $nM^{-1}\,s^{-1}$ for the vertical reactions.

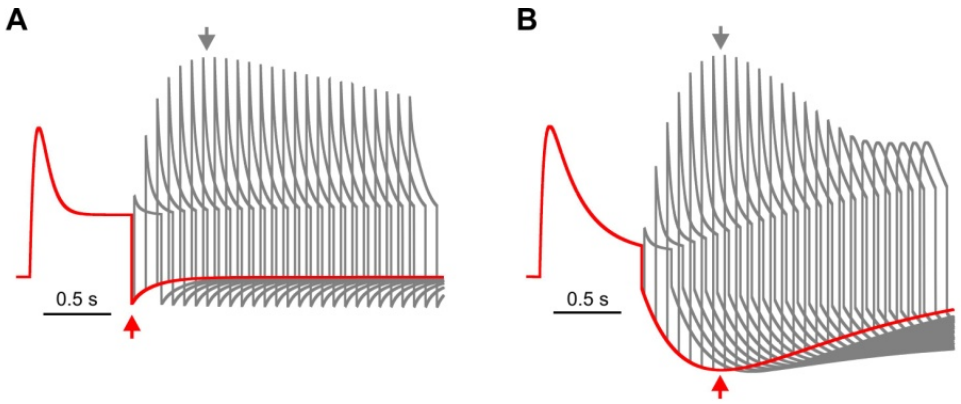

Figure S2.5. Simulations of recovery from block of Hv1 F150A generated with two alternative models, related to Figure 2.6. Control peaks and tail currents are shown in red, recovery peaks are shown in gray. The voltage was changed following the two-pulse protocol of Fig. 2.5A. t_{IP} was increased in 85ms-long increments. Currents were normalized at the level of the control peak. **(A)** Recovery from block generated by our current model of channel gating with hemichannel blocker trapping (same model used to generate Fig. 2.6B). In the simulation shown here the time scale and the interval between recovery pulses were chosen to highlight the delay between the maximal tail current (red arrow) and the highest recovery peak (gray arrow) generated by this model. The calculated delay of ~0.60 s is close to the experimental value of 0.52 s. The predicted cause of the delay is the formation of long-lived blocked hemi-channels (BC) that can quickly form conducting BO channels at positive potentials. **(B)** Simulation of recovery from block in an alternative model of channels with uncoupled gates. The rates of opening, closing, blocking, and unblocking were fine-tuned to generate recovery peaks higher than the control peak to resemble the phenomenon seen in (A). Although the extent to which the recovery peaks "overshoot" the control and the time to reach the highest peak are the same in (A) and (B), the size and kinetics of the tail current generated by model (B) are not in agreement with the experimental data. In addition, model (B) fails to reproduce the experimentally observed delay between the maximal tail current and the highest recovery peak because the same channel species are responsible for both maxima (channels with at least one open and unblocked subunit).

Table S2.1. Dose dependence of inhibition

Channel	*Inhibitor*	K_d *(μM)*	*h*	*n*
Hv1 WT	2GBI	38.3 ± 0.7	0.90 ± 0.02	7
Eh-Hv1/HVCN1 WT	2GBI	86.7 ± 4.9	0.94 ± 0.03	7
Ci-Hv1/VSOP WT	2GBI	52.3 ± 1.2	0.92 ± 0.02	6
Hv1 F150C	2GBI	8.32 ± 0.35	0.97 ± 0.04	5
Hv1 F150A	2GBI	0.105 ± 0.007	0.91 ± 0.04	6
Hv1 F150W	2GBI	52.6 ± 1.6	0.92 ± 0.03	4
Hv1 WT	2GBOZ	8600 ± 900	0.90*	5
Hv1 F150C	2GBOZ	815 ± 43	0.87 ± 0.04	6
Hv1 F150A	2GBOZ	16.7 ± 1.0	0.88 ± 0.04	7

*This value was used as fixed parameter in the Hill fit

Table S2.2. G-V relationships in presence and absence of 2GBI

Channel	$V_{1/2}$ *(mV)*	RT/z_gF *(mV)*	*n*
Hv1 WT	53.1 ± 2.3	10.9 ± 0.8	6
Hv1 WT +200μM 2GBI	50.0 ± 2.4	10.8 ± 0.5	6
Hv1 F150W	-2.3 ± 2.9	12.5 ± 1.1	5
Hv1 F150C	30.6 ± 2.8	9.1 ± 0.4	4
Hv1 F150A	29.0 ± 2.8	10.7 ± 0.3	6

Supplementary Experimental Procedures

Dose responses of channel inhibition in Fig. 2.2D and Fig. 2.4C & E were fitted by the Hill equation:

$$\%_i = \%_{i,max}[B]^h/\left(K_d^h + [B]^h\right) \quad \text{(S1)}$$

where $\%_{i,max}$ is the maximal percentage of channel inhibition by compound B, h is the Hill coefficient and K_d is the dissociation constant. Fit parameters are reported in Table S1.

G-V measurements were performed in inside-out patches at pH_i=pH_o=6.0 in constant perfusion of the bath compartment to increase buffer turnover by convection. The conductance was determined from tail currents as previously described (Musset et al., 2008; Tombola et al., 2010) using the following equation:

$$G(V_{test}) = (I_{test} - I_{tail})/(V_{test} - V_{tail}) \quad \text{(S2)}$$

where I_{test} is the current at V_{test} , measured at the end of the depolarization step of the voltage protocol, and I_{tail} is the current at V_{tail} , measured at the beginning of the repolarization step. A reference pulse preceding the test pulse was used to correct for current rundown (Tombola et al., 2010). G-V plots were fitted by the Boltzmann equation:

$$G/G_{max} = 1/\left(1 + \exp\left(-\frac{z_g F}{RT}(V - V_{1/2})\right)\right) \quad \text{(S3)}$$

where z_g is the apparent gating charge, T is the absolute temperature, $V_{1/2}$ is the potential of half activation, and F and R are the Faraday and gas constants, respectively. Fit parameters are reported in Table S2.

Fast perfusion of 2GBI on excised patches was carried out with a multi-barrel perfusion pencil (AutoMate Sci.) positioned in front of the patch pipette. Solutions were perfused under gravity via delivery tips either 250 μm or 360 μm in diameter. The pencil was connected to a VC-6 perfusion valve system (Warner Instr.) controlled by the pClamp software via TTL signal.

Voltage and pH_o dependence of 2GBI block

We determined the voltage dependence of the dissociation constant of 2GBI as follows: we first recorded Hv1 currents in the presence of 50 μM 2GBI using a voltage protocol in which a depolarization to +140 mV was followed by a step at progressively lower voltages, from +130 mV to +20 mV in 10-mV negative increments (Fig. 2.3A). We then measured the current levels ($I(V)$) at the beginning of each voltage step and calculated the fractions of unblocked-open channels ($f_o(V)$) relative to the reference potential (V_{ref}) of +120 mV using equation S4.

$$f_o(V) = f_o(V_{ref})\frac{I(V)}{I(V_{ref})}\frac{V_{ref}}{V} \tag{S4}$$

Since the K_d at V_{ref} is known from equation S1, we derived $f_o(V_{ref})$ from equation S5.

$$f_o(V_{ref}) = \frac{K_d(V_{ref})}{[B] + K_d(V_{ref})} \tag{S5}$$

Finally, we calculated the dissociation constants at other voltages ($K_d(V)$) by using a rearranged form of equation S4 (Fig. 2.3B). The data were then fitted with equation S6 to obtain the value of the maximal apparent fraction of electric field experienced by the blocker bound to the VSD pore (δ) (Hille, 2001; Woodhull, 1973).

$$K_d(V) = K_d(0)\exp\left(-\frac{\delta z_b F}{RT}V\right) \quad \text{(S6)}$$

$K_d(0)$ is the dissociation constant in the absence of membrane potential, and z_b is the charge of the blocker (+1).

To determine the effect of the extracellular proton concentration on the rates of closing and unblocking, tail currents were recorded at -40 mV in outside-out patches while perfusing the bath with buffer solutions at pH 6.0 or 7.5 (Fig. 2.3C). Tails measured in the absence of the blocker were fitted with equation:

$$I(V,t) = c_{fast}\exp\left(-t/\tau_{fast}\right) + c_c\exp(-t/\tau_c) \quad \text{(S7)}$$

where τ_c is the time constant of channel closing, and τ_{fast} is the time constant of a fast component of the tail current, which includes the capacitive transient. τ_c values were obtained at the two different extracellular proton concentrations, and the control ratio $\tau_{7.5}/\tau_{6.0}$ in the first column of Fig. 3D reports on the pH_o dependence of τ_c. A similar set of measurements were then conducted in the presence of 200 μM 2GBI in the pipette. Under these conditions, the decays of the tail currents display a third exponential component that depends on the unbinding of the blocker. To fit these tail currents the term $c_{2GBI}\exp\left(-t/\tau_{2GBI}\right)$ was added to equation S7. The values of the time constants measured in the absence of the blocker were used as fixed parameters to obtain the τ_{2GBI} at the two different pH_o values. The ratio $\tau_{7.5}/\tau_{6.0}$ in the second column of Fig. 2.3D reports on the pH_o dependence of τ_{2GBI}.

Alternative model of Hv1 recovery from block

It is important to note that the mechanism of recovery from block shown in Figures 2.6 and S2.4 does not explain just the appearance of recovery peaks higher than the control peak in the F150A dimer, but also the time course of the recovery and the relative position of the highest recovery peak compared to the maximal tail current. As shown in Fig. S2.5, recovery peaks higher than the control peak can be generated also by a model in which unblocked-open channels are quickly produced during the repolarization step between consecutive depolarizations. Because these channels are already open at the beginning of the second pulse, they can make the recovery peak overshoot the control peak. The assumption of coupling between gates is not necessary for this model to work. Although this simple mechanism can generate overshooting recovery current, it fails to reproduce other important aspects of the experimental data (e.g., position of the maximum recovery peak compared to the maximal tail current, see Fig. S2.4).

2.6 References

Alabi, A.A., Bahamonde, M.I., Jung, H.J., Kim, J.I., and Swartz, K.J. (2007). Portability of paddle motif function and pharmacology in voltage sensors. Nature *450*, 370–375.

Armstrong, C.M. (1968). Induced inactivation of the potassium permeability of squid axon membranes. Nature *219*, 1262–1263.

Armstrong, C.M. (1971). Interaction of tetraethylammonium ion derivatives with the potassium channels of giant axons. J. Gen. Physiol. *58*, 413–437.

Berger, T.K., and Isacoff, E.Y. (2011). The pore of the voltage-gated proton channel. Neuron *72*, 991–1000.

Capasso, M., Decoursey, T.E., and Dyer, M.J.S. (2011). pH regulation and beyond: unanticipated functions for the voltage-gated proton channel, HVCN1. Trends Cell Biol. *21*, 20–28.

Choi, K.L., Mossman, C., Aubé, J., and Yellen, G. (1993). The internal quaternary ammonium receptor site of Shaker potassium channels. Neuron *10*, 533–541.

Decoursey, T.E., and Cherny, V.V. (2007). Pharmacology of voltage-gated proton channels. Curr. Pharm. Des. *13*, 2400–2420.

Decoursey, T.E., Morgan, D., and Cherny, V.V. (2003). The voltage dependence of NADPH oxidase reveals why phagocytes need proton channels. Nature *422*, 531–534.

Fujiwara, Y., Kurokawa, T., Takeshita, K., Kobayashi, M., Okochi, Y., Nakagawa, A., and Okamura, Y. (2012). The cytoplasmic coiled-coil mediates cooperative gating temperature sensitivity in the voltage-gated H(+) channel Hv1. Nat Commun *3*, 816.

Gonzalez, C., Koch, H.P., Drum, B.M., and Larsson, H.P. (2010). Strong cooperativity between subunits in voltage-gated proton channels. Nat. Struct. Mol. Biol. *17*, 51–56.

Hille, B. (2001). Ion Channels of Excitable Membranes (Sunderland: Sinauer Associates Inc).

Holmgren, M., Smith, P.L., and Yellen, G. (1997). Trapping of organic blockers by closing of voltage-dependent K+ channels: evidence for a trap door mechanism of activation gating. J. Gen. Physiol. *109*, 527–535.

Horton, R.M., Cai, Z.L., Ho, S.N., and Pease, L.R. (1990). Gene splicing by overlap extension: tailor-made genes using the polymerase chain reaction. BioTechniques *8*, 528–535.

Kalia, J., and Swartz, K.J. (2011). Elucidating the molecular basis of action of a classic drug: guanidine compounds as inhibitors of voltage-gated potassium channels. Mol. Pharmacol. *80*, 1085–1095.

Koch, H.P., Kurokawa, T., Okochi, Y., Sasaki, M., Okamura, Y., and Larsson, H.P. (2008).

Multimeric nature of voltage-gated proton channels. Proc. Natl. Acad. Sci. U.S.a. *105*, 9111–9116.

Krieg, P.A., and Melton, D.A. (1984). Functional messenger RNAs are produced by SP6 in vitro transcription of cloned cDNAs. Nucleic Acids Res. *12*, 7057–7070.

Lacroix, J.J., and Bezanilla, F. (2011). Control of a final gating charge transition by a hydrophobic residue in the S2 segment of a K+ channel voltage sensor. Proc. Natl. Acad. Sci. U.S.a. *108*, 6444–6449.

Lee, S.-Y., Letts, J.A., and Mackinnon, R. (2008). Dimeric subunit stoichiometry of the human voltage-dependent proton channel Hv1. Proc. Natl. Acad. Sci. U.S.a. *105*, 7692–7695.

Lee, S.-Y., Letts, J.A., and Mackinnon, R. (2009). Functional reconstitution of purified human Hv1 H+ channels. J. Mol. Biol. *387*, 1055–1060.

Li, S.J., Zhao, Q., Zhou, Q., Unno, H., Zhai, Y., and Sun, F. (2010). The role and structure of the carboxyl-terminal domain of the human voltage-gated proton channel Hv1. J. Biol. Chem. *285*, 12047–12054.

Liman, E.R., Tytgat, J., and Hess, P. (1992). Subunit stoichiometry of a mammalian K+ channel determined by construction of multimeric cDNAs. Neuron *9*, 861–871.

Long, S.B., Tao, X., Campbell, E.B., and Mackinnon, R. (2007). Atomic structure of a voltage-dependent K+ channel in a lipid membrane-like environment. Nature *450*, 376–382.

Macey, R., Oster, G., and Zahley, T. (2009). Berkeley Madonna User's Guide. Berkely.

Murata, Y., Iwasaki, H., Sasaki, M., Inaba, K., and Okamura, Y. (2005). Phosphoinositide phosphatase activity coupled to an intrinsic voltage sensor. Nature *435*, 1239–1243.

Musset, B., Morgan, D., Cherny, V.V., MacGlashan, D.W., Thomas, L.L., Ríos, E., and Decoursey, T.E. (2008). A pH-stabilizing role of voltage-gated proton channels in IgE-mediated activation of human basophils. Proc. Natl. Acad. Sci. U.S.a. *105*, 11020–11025.

Musset, B., Smith, S.M.E., Rajan, S., Cherny, V.V., Sujai, S., Morgan, D., and Decoursey, T.E. (2010). Zinc inhibition of monomeric and dimeric proton channels suggests cooperative gating. The Journal of Physiology *588*, 1435–1449.

Musset, B., Smith, S.M.E., Rajan, S., Morgan, D., Cherny, V.V., and Decoursey, T.E. (2011). Aspartate 112 is the selectivity filter of the human voltage-gated proton channel. Nature *480*, 273–277.

Narahashi, T., Yamada, M., and FRAZIER, D.T. (1969). Cationic forms of local anaesthetics block action potentials from inside the nerve membrane.

Okamura, Y. (2007). Biodiversity of voltage sensor domain proteins. Pflugers Arch. *454*, 361–371.

Ramsey, I.S., Mokrab, Y., Carvacho, I., Sands, Z.A., Sansom, M.S.P., and Clapham, D.E. (2010). An aqueous H+ permeation pathway in the voltage-gated proton channel Hv1. Nat. Struct. Mol. Biol. *17*, 869–875.

Ramsey, I.S., Moran, M.M., Chong, J.A., and Clapham, D.E. (2006). A voltage-gated proton-selective channel lacking the pore domain. Nature *440*, 1213–1216.

Sasaki, M., Takagi, M., and Okamura, Y. (2006). A voltage sensor-domain protein is a voltage-gated proton channel. Science *312*, 589–592.

Sokolov, S., Scheuer, T., and Catterall, W.A. (2005). Ion permeation through a voltage-sensitive gating pore in brain sodium channels having voltage sensor mutations. Neuron *47*, 183–189.

Sokolov, S., Scheuer, T., and Catterall, W.A. (2007). Gating pore current in an inherited ion channelopathy. Nature *446*, 76–78.

Sokolov, S., Scheuer, T., and Catterall, W.A. (2010). Ion permeation and block of the gating pore in the voltage sensor of NaV1.4 channels with hypokalemic periodic paralysis mutations. J. Gen. Physiol. *136*, 225–236.

Starace, D.M., and Bezanilla, F. (2004). A proton pore in a potassium channel voltage sensor reveals a focused electric field. Nature *427*, 548–553.

Struyk, A.F., and Cannon, S.C. (2007). A Na+ channel mutation linked to hypokalemic periodic paralysis exposes a proton-selective gating pore. J. Gen. Physiol. *130*, 11–20.

Søndergaard, C.R., Olsson, M.H., Rostkowski, M., and Jensen, J.H. (2011). Improved treatment of ligands and coupling effects in empirical calculation and rationalization of p K a values. Journal of Chemical Theory and Computation *7*, 2284–2295.

Tao, X., Lee, A., Limapichat, W., Dougherty, D.A., and Mackinnon, R. (2010). A gating charge transfer center in voltage sensors. Science *328*, 67–73.

Taylor, A.R., Chrachri, A., Wheeler, G., Goddard, H., and Brownlee, C. (2011). A voltage-gated H+ channel underlying pH homeostasis in calcifying coccolithophores. PLoS Biol. *9*, e1001085.

Tombola, F., Pathak, M.M., and Isacoff, E.Y. (2005). Voltage-sensing arginines in a potassium channel permeate and occlude cation-selective pores. Neuron *45*, 379–388.

Tombola, F., Pathak, M.M., Gorostiza, P., and Isacoff, E.Y. (2007). The twisted ion-permeation pathway of a resting voltage-sensing domain. Nature *445*, 546–549.

Tombola, F., Ulbrich, M.H., and Isacoff, E.Y. (2008). The voltage-gated proton channel Hv1 has two pores, each controlled by one voltage sensor. Neuron *58*, 546–556.

Tombola, F., Ulbrich, M.H., Kohout, S.C., and Isacoff, E.Y. (2010). The opening of the two

pores of the Hv1 voltage-gated proton channel is tuned by cooperativity. Nat. Struct. Mol. Biol. *17*, 44–50.

Wang, Y., Li, S.J., Pan, J., Che, Y., Yin, J., and Zhao, Q. (2011). Specific expression of the human voltage-gated proton channel Hv1 in highly metastatic breast cancer cells, promotes tumor progression and metastasis. Biochem. Biophys. Res. Commun. *412*, 353–359.

Wang, Y., Li, S.J., Wu, X., Che, Y., and Li, Q. (2012). Clinicopathological and biological significance of human voltage-gated proton channel Hv1 protein overexpression in breast cancer. J. Biol. Chem. *287*, 13877–13888.

Wood, M.L., Schow, E.V., Freites, J.A., White, S.H., Tombola, F., and Tobias, D.J. (2012). Water wires in atomistic models of the Hv1 proton channel. Biochim. Biophys. Acta *1818*, 286–293.

Woodhull, A.M. (1973). Ionic blockage of sodium channels in nerve. J. Gen. Physiol. *61*, 687–708.

Wu, L.-J., Wu, G., Akhavan Sharif, M.R., Baker, A., Jia, Y., Fahey, F.H., Luo, H.R., Feener, E.P., and Clapham, D.E. (2012). The voltage-gated proton channel Hv1 enhances brain damage from ischemic stroke. Nat. Neurosci. *15*, 565–573.

Yeh, J.Z., and Armstrong, C.M. (1978). Immobilisation of gating charge by a substance that simulates inactivation. Nature *273*, 387–389.

Yu, F.H., and Catterall, W.A. (2004). The VGL-chanome: a protein superfamily specialized for electrical signaling and ionic homeostasis. Sci. STKE *2004*, re15.

Chapter 3: Molecular determinants of Hv1 proton channel inhibition by guanidine derivatives

(Hong, Kim, Tombola)

Abstract

The voltage-gated proton channel Hv1 plays important roles in proton extrusion, pH homeostasis, and production of reactive oxygen species in a variety of cell types. Excessive Hv1 activity increases proliferation and invasiveness in cancer cells, and worsens brain damage in ischemic stroke. The channel is composed of two subunits, each containing a proton-permeable voltage-sensing domain (VSD) and lacking the pore domain typical of other voltage-gated ion channels. We have previously shown that the compound 2-guanidinobenzimidazole (2GBI) inhibits Hv1 proton conduction by binding to the VSD from its intracellular side (Hong et al., 2013). Here, we examine the binding affinities of a series of 2GBI derivatives on human Hv1 channels mutated at positions located in the core of the VSD and apply mutant cycle analysis to determine how the inhibitor interacts with the channel. We identify four Hv1 residues involved in the binding: aspartate 112, phenylalanine 150, serine 181, and arginine 211. 2GBI appears to be oriented in the binding site with its benzo-ring pointing toward F150, with its imidazole ring inserted between residue D112 and residues S181 and R211, and with the guanidine group positioned in the proximity of R211. We also identify a modified version of 2GBI that is able to reach the binding site on Hv1 from the extracellular side of the membrane.

Understanding how compounds like 2GBI interact with the Hv1 channel is an important step toward the development of pharmacological treatments for diseases caused by Hv1 hyperactivity.

The activity of the Hv1 proton channel has been shown to exacerbate neuronal death following cerebral hypoxia and to promote tumor formation by highly metastatic breast cancer cells. Compounds able to inhibit excessive Hv1 activity could find applications as neuroprotective agents in ischemic stroke or as anticancer drugs. In this paper, we investigate how guanidine derivatives like 2-guanidinobenzimidazole (2GBI) interact with Hv1 and inhibit proton conduction. We identify the binding site for 2GBI and determine the most likely orientation of the inhibitor inside the channel. We also show that a simple modification of 2GBI eliminates the requirement for the inhibitor to have direct access to the intracellular side of the channel in order to block the proton current.

3.1 Introduction

The Hv1 voltage-gated proton channel (also known as HVCN1 or VSOP) regulates the production of superoxide and other reactive oxygen species (ROS) by NADPH oxidase (NOX) enzymes in a variety of cell types, including microglial cells (Wu et al., 2012), and leukocytes (Decoursey, 2013). NOX activity causes membrane depolarization and intracellular accumulation of protons. Hv1 allows sustained NOX activity by re-polarizing the membrane and by extruding excess protons from the cell (Chemaly et al., 2010; Decoursey et al., 2003; Ramsey et al., 2009).

Hv1 has been shown to enhance brain damage in a mouse model of ischemic stroke through its NOX-modulating activity (Wu et al., 2012). The channel was also found over-expressed in many B-cell malignancies (Capasso et al., 2010), and in breast and colorectal cancer tissues (Wang et al., 2012; 2013). High Hv1 activity was shown to increase invasiveness of breast cancer cells and to be associated with shorter overall and recurrence-free survival in breast cancer patients (Hong et al., 2013; Wang et al., 2012). These findings highlight the fact that excessive activity of the Hv1 channel can have serious pathological consequences in ischemic stroke and cancer, and that small-molecule inhibitors targeting Hv1 could lead to the development of new neuroprotective or anticancer drugs.

The Hv1 protein is made of four membrane-spanning segments, (S1 through S4) (Ramsey et al., 2006; Sasaki et al., 2006; Wu et al., 2012), and it is related to the voltage-sensing domains (VSDs) of other voltage-gated ion channels (Decoursey, 2013; Yu and Catterall, 2004) and voltage-sensitive phosphatases (VSPs) (Chemaly et al., 2010; Decoursey et al., 2003; Murata et al., 2005; Ramsey et al., 2009). The inner end of the S4 segment is connected to a coiled-coil domain responsible for protein dimerization (Fujiwara et al., 2012; Li et al., 2010; Wu et al., 2012). As a result, the channel is made of two VSD subunits each containing a gated proton pore (Capasso et al., 2010; Koch et al., 2008; Lee et al., 2008; Tombola et al., 2008).

The block of voltage-gated sodium, potassium, and calcium channels by small molecules has been studied for decades. Its mechanism has been elucidated for many drugs and in the majority of cases the inhibitors were found to bind to different regions of the pore domain (Hille, 2001; Wang et al., 2012; 2013; Wulff et al., 2009). With the exception of peptide toxins [e.g., (Swartz and MacKinnon, 1995; Wang et al., 2011)], not much is known about compounds interacting with VSDs (Börjesson and Elinder, 2011), and only recently have there been successful attempts to produce small molecule drugs that target specifically these domains in voltage-gated ion channels (Li et al., 2013; Peretz et al., 2010).

We have recently shown that some guanidine derivatives have the ability to inhibit Hv1 activity and that one of these compounds, 2-guanidinobenzimidazole (2GBI) binds the channel's VSD only in the open conformation (Hong et al., 2013). We have also found that the binding site lies within the proton permeation pathway and faces the cytoplasm.

Here we explore the chemical space available to guanidine derivatives for Hv1 binding. We then use a mutation cycle analysis approach to identify the residues in the channel that contribute to the binding environment of 2GBI and to establish the overall orientation of the blocker within the VSD in the open conformation. Our results suggest that residues D112, F150, S181, and R211 are located close to each other deep within the membrane and in the proximity of the VSD's intracellular vestibule where they can interact with the blocker. We discuss our binding model in the context of a recent crystal structure of the channel (Takeshita et al., 2014).

3.2 Materials and Methods

Hv1 expression

Recombinant human Hv1 channel was subcloned in the pGEMHE vector (Liman et al., 1992) as previously described (Hong et al., 2013). Single point mutations were introduced with standard PCR techniques. Plasmids were linearized with NheI restriction enzyme (New England Biolabs) before *in vitro* transcription. RNA synthesis was carried out with a T7 mMessage mMachine transcription kit (Ambion). cRNAs were injected in *Xenopus* oocytes (50 nl per cell, 0.3-1.5 μg/μl) 1-3 days before the electrophysiological measurements.

Cultured cells

Stage V and VI oocytes were either prepared from *Xenopus laevis* (NASCO) using well-established methods, or purchased from Ecocyte Bioscience. Cells were kept at 18 °C in ND96 medium containing 96 mM NaCl, 2 mM KCl, 1.8 mM $CaCl_2$, 1 mM $MgCl_2$, 10 mM HEPES, 5 mM pyruvate, 100 μg/ml gentamycin, pH 7.2. BV-2 and THP-1 cells were gifts from Dr. H. Wulff (UC Davis) and Dr. A. Zlotnik (UC Irvine), respectively. RAW264.7 cells were from ATCC (TIB-71). BV-2 and RAW264.7 cells were maintained in Dulbecco's Modified Eagle's Medium supplemented with 10% FBS. THP-1 cells were maintained in RPMI-1640 medium supplemented with 10% FBS and 50 μM 2-mercaptoethanol. Cells were kept at 37 °C in a 5% CO_2 incubator.

Tested compounds

2-guanidinobenzimidazole, 2-(2-benzimidazolylamino)-imidazole-4,5-dione, 5-chloro-2-guanidino-benzimidazole, 5-nitro-2-guanidinobenzimidazole, N-(4-chlorophenyl)-4H-1,2,4-triazole-3,5-diamine, 1-(benzimidazol-2-yl)urea, N-(4-chlorophenyl)-1,3,5-triazine-2,4-diamine hydrochloride, amiloride hydrochloride, isoproyl 6-(guanidinoimino)-6-phenylhexanoate nitrate, and 1-[2-(5-methoxy-1H-indol-3-yl)ethyl]guanidine hydroiodide were from Sigma-Aldrich. 1-[5-(morpholin-4-ylsulfonyl)-1H-benzimidazol-2-yl]guanidine was from Enamine. 4-phenyl-1,4-dihydro[1,3,5]triazino[1,2-a]benzimidazol-2-amine, S-1H-benzimidazol-2-yl-carbamothioate, 2-guanidinobenzoxazole, 1-(benzimidazol-2-yl)-3-(2-phenylethyl) guanidine, and 3a,8a-dihydroxy-2-imino-2,3,3a,8a-tetrahydroindeno[1,2-d]imidazol-8(1H)-one were from Vitas-M Lab. Creatinine was from Acros Organics, and leonurine was from Combi-Blocks. All the guanidine derivatives used were at the highest purity commercially available. The compounds were directly dissolved in the recording solutions at the desired final concentrations or prepared as 100 mM stock solutions in DMSO. The bath chamber was perfused under gravity via manifold connected to a VC-6 perfusion valve system (Warner Instr.) controlled by the pClamp software via TTL signal. Predicted logP values were calculated with ALOGPS (Virtual Computational Chemistry Laboratory, http://www.vcclab.org) (Tetko et al., 2005).

Electrophysiological measurements

Hv1 proton currents were measured in inside-out or outside-out patches from oocytes, using an Axopatch 200B amplifier controlled by pClamp10 software through an Axon Digidata 1440A (Molecular Devices). The intracellular solution contained 100 mM 2-(N-morpholino)ethanesulphonic acid (MES), 30 mM tetraethylammonium (TEA) methanesulfonate, 5 mM TEA chloride, 5 mM ethyleneglycol-bis(2-aminoethyl)-N,N,N',N'-tetra-acetic acid (EGTA), adjusted to pH 6.0 with TEA hydroxide. For recordings carried out in the absence of pH gradient, extracellular and intracellular solutions had the same composition. For measurements performed in the presence of a pH gradient (pH_i = 6.0, pH_o = 7.5) the extracellular solution contained 100 mM 4-(2-hydroxyethyl)-1-piperazineethanesulfonic acid (HEPES), 40 mM TEA methanesulfonate, 5 mM TEA chloride, adjusted to pH 7.5 with TEA hydroxide.

Channel inhibition was determined by isochronal current measurements at the end of a depolarization pulse at +120mV. The duration of the pulse was different for different channels (Fig. 3.2B) to account for the difference in time required to reach steady state activation. An example of time course of inhibition is reported in Fig. 3.1C. At +120mV (and pH_i = pH_o = 6.0), wild type and mutant channels are maximally open, with the exception of R211S (Fig. S3.2). For this mutant under the experimental conditions used, only ~50% of channels are open at +120mV. Since the inhibitor binds Hv1 only in the open state, and it does not change the channel's voltage dependence of activation (Hong et al., 2013), the assessment of inhibition is not affected by the presence of closed channels. We interpret

the change in G-V produced by the R211S mutation as the direct result of a missing gating charge, as previously shown (Gonzalez et al., 2013).

Native proton currents in BV-2, RAW264.7, and THP-1 were measured in whole-cell configuration with an intracellular solution containing: 90 mM TEA methanesulfonate, 100 mM MES, 2 mM $MgCl_2$, 2 mM EGTA, adjusted to pH 6.0 with TEA hydroxide. The extracellular solution contained: 85 mM TEA methanesulfonate, 100 mM HEPES, 3 mM $CaCl_2$, 1 mM EGTA, adjusted to pH 7.5 with TEA hydroxide. All measurements were performed at 22 ± 2 °C. Pipettes had 1.5–4 MΩ access resistance. Current traces were filtered at 1 kHz, sampled at 5 kHz and analyzed with Clampfit10.2 (Molecular Devices) and Origin8.1 (OriginLab).

Mutant cycle analysis

Dose responses of channel inhibition in Figs. 3.3A, S3.3, S3.4, and S3.5B were fitted by the Hill equation:

$$\%_i = 100[B]^h/(K_d^h + [B]^h)$$

where [B] is the concentration of inhibitor B, K_d is the apparent dissociation constant, and h is the Hill coefficient. Fit parameters are reported in Table S1 and text. In some dose responses curves, due to limits in solubility of inhibitors 9 and 11, we could test maximal concentrations that produced less than 80% inhibition. In these cases, the Hill coefficient

was constrained between 0.80 and 1.00 for the fitting, and the curves were extrapolated to 100% inhibition as dotted lines (Fig. 3.3A).

$\Delta\Delta G^o(ij)$ values relative to position *i* in the channel and part *j* of the inhibitor were calculated according to the equation:

$$\Delta\Delta G^o(ij) = \Delta G^o(ij \to 0j) - \Delta G^o(i0 \to 00) = \Delta G^o(ij \to i0) - \Delta G^o(0j \to 00)$$
$$= -RTln\frac{K_d^{0j}K_d^{i0}}{K_d^{ij}K_d^{00}}$$

where *0* stands for either a mutation in the channel at position *i* or a change in structural feature in the inhibitor at position *j*. For instance, the mutation ($i \to 0$) in Hv1 can be F150A, and the change in the inhibitor ($j \to 0$) can be a chlorine atom replacing the hydrogen at position 5 in the benzo-ring of 2GBI (compound 4).

Mapping tested residues on the Hv1-CiVSP chimera

In the chimera's VSD, residues E149 through F171 of mouse Hv1/VSOP are replaced with residues D164 through L188 of CiVSP. Tested residues in human Hv1: V109, D112, F150, E153, V178, S181, F182, R208, and R211 correspond to residues V105, D108, F146, D149, V174, S177, F178, R204, and R207 of the chimera, respectively. Representation of the structure shown in Fig. 3.4B was made in PyMOL (Schrödinger).

3.3 Results

3.3.1 Molecular features of guanidine derivatives regulating Hv1 inhibition

To understand what makes 2GBI (Fig. 3.1A, compound 1) an effective Hv1 inhibitor, we tested analogs 2 to 12 (Fig. 3.1A) for their ability to inhibit proton currents measured in inside-out patches from *Xenopus* oocytes expressing the human Hv1 channel. The analogs differed from 2GBI in selected molecular features, such as nature of heteroatoms, substituents, or ring connectivity. We also examined compounds 13 to 18 (Fig. 3.1A) to determine whether structures of guanidine derivatives unrelated to 2GBI could be compatible with tight binding.

Since 2GBI binds an intracellular receptor on the Hv1 channel (Hong et al., 2013), we added the guanidine derivatives to the intracellular side of the membrane patches (Fig. 3.1B – C). The activity of different derivatives was compared at the final concentration of 200 μM (Fig. 3.1D, black columns), with the exception of compounds 4, 5, and 15, which were tested at the concentration of 10 μM (Fig. 3.1D, gray columns). The inhibition induced by compound 1 is reported in Fig. 3.1D at both concentrations for reference.

We found that among the 2GBI analogs, two compounds with substitutions in the benzo-ring (4 and 5) were more effective than the reference compound when used at the same concentration. Three other analogs (2, 6, and 8) showed activity similar to 2GBI, while the rest of the compounds were less effective. Among the guanidine derivatives unrelated to

2GBI, only compound 15 showed activity higher than 2GBI. Adding bulky hydrophobic groups to the guanidine moiety (compounds 3 and 12) impaired binding to the channel, as did opening of the imidazole ring (compounds 7 and 10). Reducing the ability of the inhibitor to bind protons had different effects depending on the nature of the modification. Some of these modifications did not significantly affect the efficiency of binding (compounds 2 and 8), while others had quite a disruptive effect (compounds 9 and 11). Overall, these findings show that the activity of 2GBI can be increased by modifications of its benzo-group, and that the neutralization of its charge to increase membrane permeability is compatible with strong binding. In addition, the fact that compound 15 produced strong Hv1 inhibition suggests that the chemical space available for binding is not limited to molecules containing the benzimidazole group.

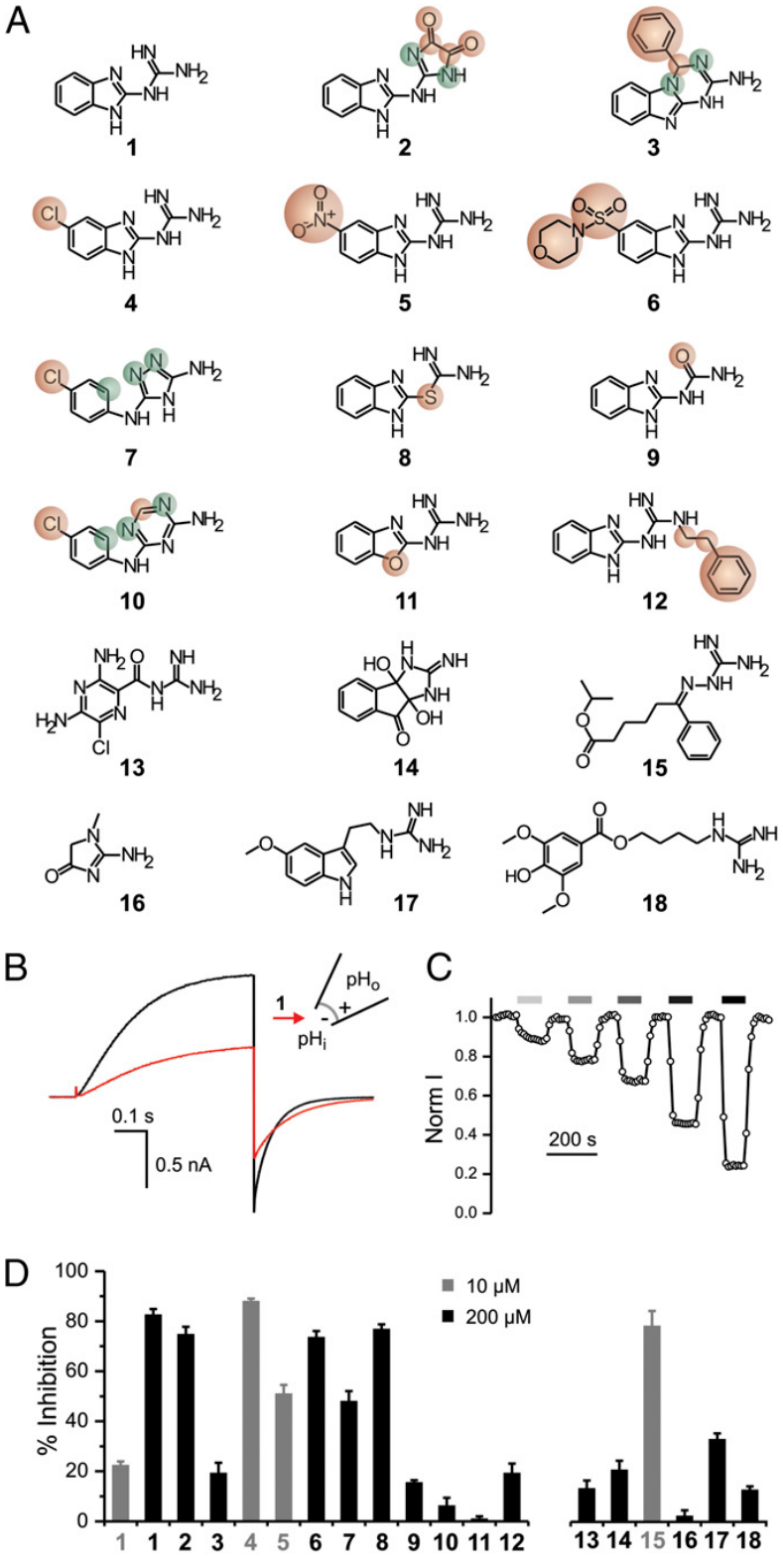

Fig. 3.1. Exploring Hv1 inhibition by guanidine derivatives. (A) Tested compounds: (1) 2GBI, (2) 2-(2-benzimidazolylamino)-imidazole-4,5-dione, (3) 4-phenyl-1,4-dihydro[1,3,5]triazino[1,2-a]benzimidazol-2-amine, (4) 5-chloro-2-guanidinobenzimidazole, (5) 5-nitro-2-guanidinobenzimidazole, (6) 1-[5-(morpholin-4-ylsulfonyl)-1H-benzimidazol-2-yl]guanidine, (7) N-(4-chlorophenyl)-4H-1,2,4-triazole-3,5-diamine, (8) S-

1H-benzimidazol-2-yl-carbamothioate, (9) 1-(benzimidazol-2-yl)urea, (10) N-(4-chlorophenyl)-1,3,5-triazine-2,4-diamine, (11) 2-guanidino-benzoxazole, (12) 1-(benzimidazol-2-yl)-3-(2-phenylethyl)guanidine, (13) amiloride, (14) 3a,8a-dihydroxy-2-imino-2,3,3a,8a-tetrahydroindeno[1,2-d]imidazol-8(1H)-one, (15) isopropyl 6-(guanidinoimino)-6-phenylhexanoate, (16) creatinine, (17) 1-[2-(5-methoxy-1Hindol-3-yl)ethyl] guanidine, and (18) leonurine. Compounds 2–12 are structurally related to compound 1. Atoms or substituents differing from compound 1 are highlighted in red. Different connectivity from compound 1 is highlighted in green. **(B)** Proton currents measured in an inside-out patch from a Xenopus oocyte expressing human Hv1 WT in response to a depolarization to +120 mV from a holding potential of −80 mV. The black trace was recorded in the absence of inhibitor, and the red trace was recorded after the addition of 50 μM compound 1 (2GBI) in the bath solution. pHi = pHo = 6.0. **(C)** Example of a time course of inhibition of Hv1 channels exposed to increasing concentrations of 2GBI. Current was normalized to the value measured under bath perfusion in the absence of inhibitor. Horizontal bars of increasingly darker gray color indicate the presence of 5, 10, 20, 50, and 100 μM inhibitor in the bath. **(D)** Inhibition of Hv1 proton currents by the indicated compounds at 10 μM (gray) or 200 μM (black) concentration. Data are means ± SEMs (n ≥ 3). Currents were measured as in B.

3.3.2 Binding environment of benzimidazole-guanidine compounds within the Hv1 VSD

We have previously shown that 2GBI inhibits the Hv1 channel by blocking its proton conduction pathway when the activation gate is open (Hong et al., 2013). But, how does 2GBI block the channel? What parts of the VSD make up the binding site, and how is the inhibitor molecule oriented inside it? Similar questions were previously addressed in a study of the Shaker potassium channel, where a mutant cycle analysis approach was used to map the binding site of the inhibitor agitoxin (Hidalgo and MacKinnon, 1995). Here, we use a similar approach to identify Hv1 residues interacting with 2GBI and to investigate specific parts of the inhibitor that contribute to channel-blocker interactions.

The interaction between a specific residue (i) in a channel and a specific part (j) of a bound inhibitor can be detected by modifying i and j, either by mutagenesis or by chemical synthesis, and then by measuring the dissociation constants (K_ds) for the four different combinations of modified and unmodified i and j (Fig. S3.1). The free energy of coupling

between *i* and *j* ($\Delta\Delta G^o(ij)$) can be then calculated from the measured K_ds (see Methods, (Horovitz and Fersht, 1990)). The size of the $\Delta\Delta G^o(ij)$ quantifies the strength of the *i* - *j* interaction, whereas its sign can indicate whether the interaction is stabilizing or destabilizing.

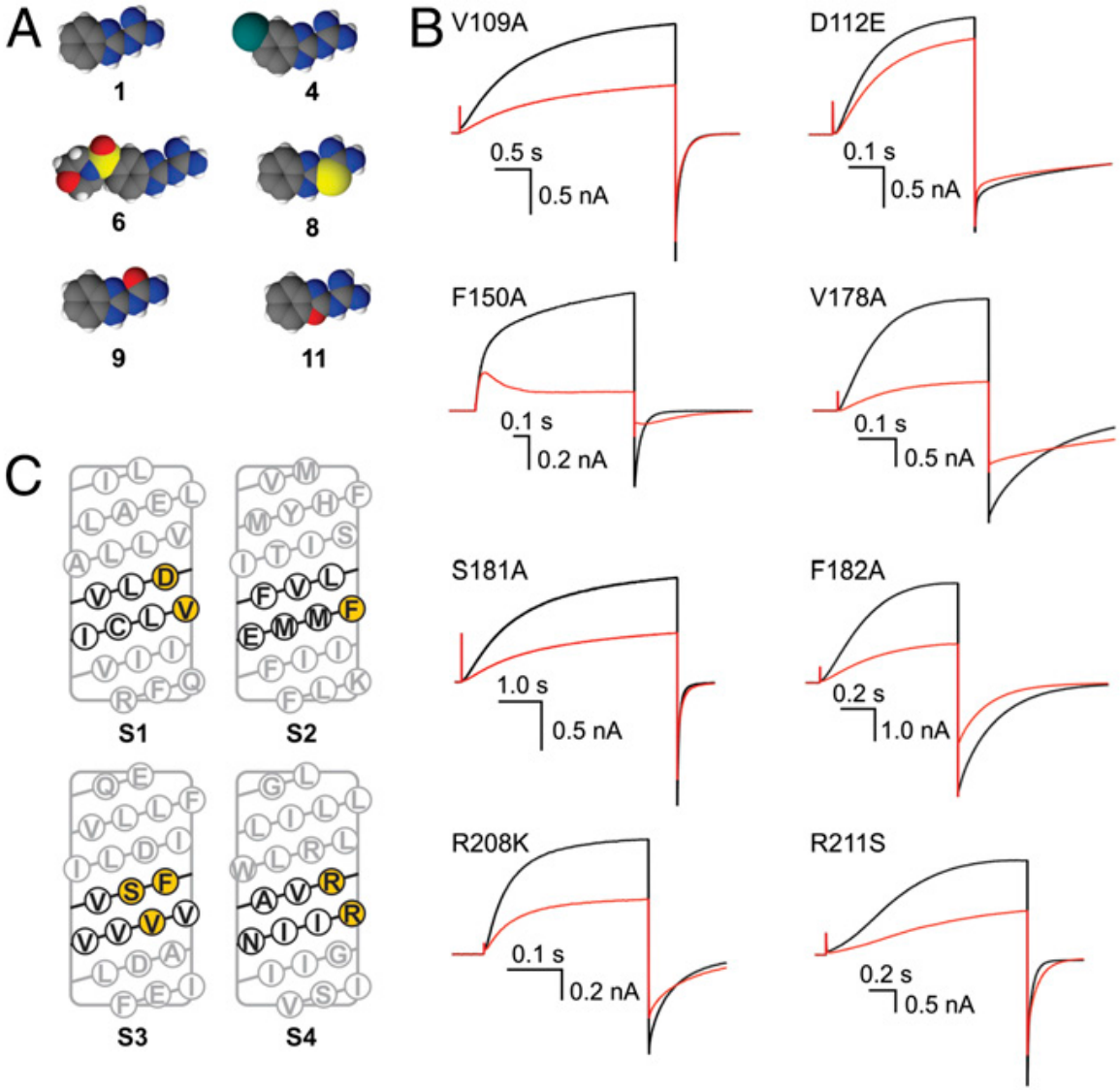

Fig. 3.2. Selection of molecular features to be analyzed in channel and inhibitor. (A) Compounds selected for the mutant cycle analysis (space-filling representation). **(B)** Examples of current inhibitions observed with the indicated Hv1 mutants in the presence of 2GBI (red traces) in the bath solution (1 μM for the F150A mutant and 50 μM for the other channels). pHi = pHo = 6.0. Currents were measured in inside-out patches on depolarization to +120 mV from a holding potential of −80 mV like in Fig. 3.1B. **(C)** Sequence of Hv1 transmembrane segments S1–S4. Residues expected to be at the same transmembrane depth as F150 are shown in black. Black residues predicted to face the core of the VSD are highlighted in yellow.

Among the 2GBI analogs shown in Fig. 3.1A, we chose for the mutant cycle analysis five compounds that differ from the reference for individual substitutions at distinct locations within the 2GBI molecule (Fig. 3.2A). On the channel, we investigated mutations of the 8 residues shown in Fig. 3.2C. In the S2 helix, we chose position 150 because we found earlier that the nature of its side chain strongly modulates the binding efficiency of both 2GBI and compound 11 (Hong et al., 2013). Residues V109 and D112 in S1 and residue R211 in S4 have been previously proposed to face the proton conduction pathway (Berger and Isacoff, 2011; Morgan et al., 2013; Musset et al., 2011), and in our structural models of Hv1 they are predicted to be in the vicinity of F150 (Wood et al., 2012). Another study recently proposed that R208 faces D112 in the core of the VSD in the open state (Kulleperuma et al., 2013). Therefore, we included positions 109, 112, 208, and 211 in our analysis. Since there is not clear experimental evidence as to whether specific S3 positions participate in proton conduction, we also included residues V178, S181, F182 in the analysis. In our Hv1 models these residues are predicted to be on the side of the S3 helix facing the center of the VSD and to be located in the middle of the transmembrane plane (Wood et al., 2012). Individual amino acid substitutions were selected as explained in the Methods section.

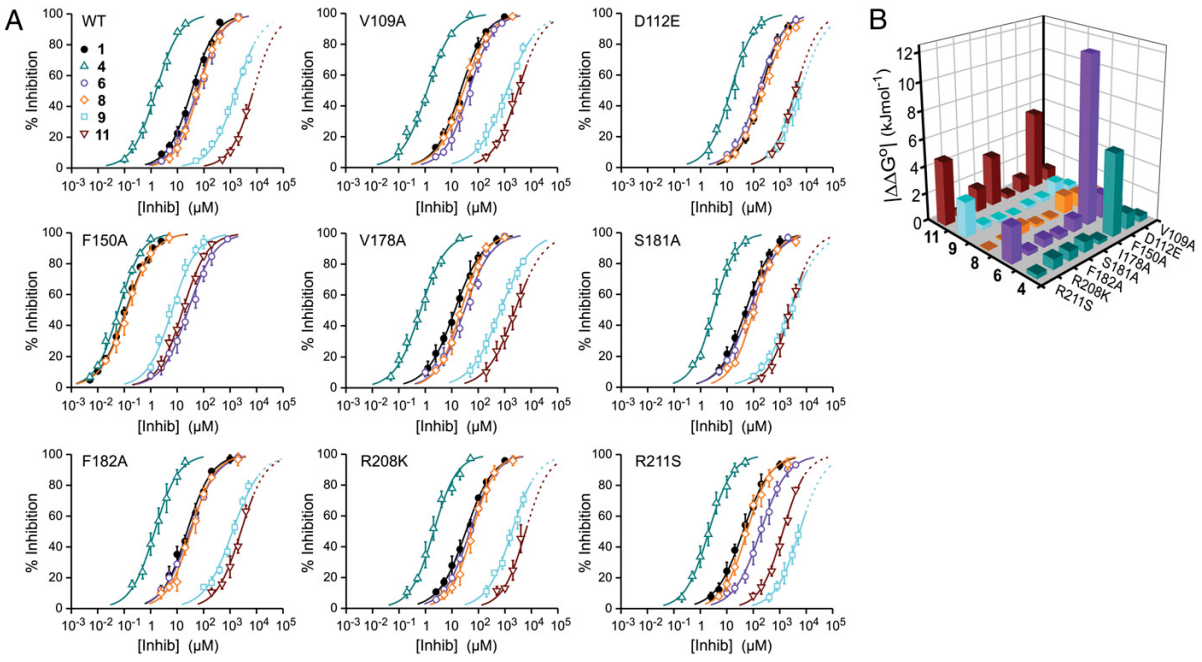

Fig. 3.3. Mutant cycle analysis. (A) Dose–response curves for the inhibition of WT and mutant channels produced by the indicated compounds (Fig. 3.2A). Reductions in proton current produced by increasing concentrations of inhibitor were measured like in Fig. 3.1C. Each point represents the average inhibition from three to six measurements ± SD. Curved lines are Hill fits. Fit parameters are reported in Table S3.1. Dotted lines for compounds 9 and 11 represent extrapolations into a concentration range where the drugs have low solubility (Methods). Inhibition of Hv1 WT and F150A by compounds 1 and 11 was reported in a previous study (Hong et al., 2013); in that study, the inhibitors were referred to as 2GBI and GBOZ, respectively (Hong et al., 2013). **(B)** Coupling free energy values for the indicated combinations of channel mutations and inhibitor modifications. Hv1 WT and compound 1 are the references. The absolute values of ΔΔGo were calculated from the apparent dissociation constants reported in Table S1 (Methods and Fig. S3.1).

We tested 2GBI and its five analogs on inside-out patches from oocytes expressing either the wild type channel or one of its eight mutants. Figure 3.1B shows an example of current traces from Hv1 wild type in the absence of 2GBI and in the presence of 50 μm intracellular inhibitor. Figure 3.2B shows equivalent traces for the individual mutants. The effects of the mutations on the channel's voltage dependence of activation (represented as conductance vs. voltage relationship (G-V)) are shown in Fig. S3.2.

From measurements like that shown in Fig. 3.1C, we determined the dose response of inhibition for a total of fifty-four channel-inhibitor combinations (symbols in Fig. 3.3A). Each dose response was fitted with the Hill equation (curves in Fig. 3.3A), and the apparent dissociation constants and Hill coefficients were determined, as reported in the Methods section (Table S3.1). The K_d values for the wild type channel and the mutants where then used to calculate the $\Delta\Delta G^o$ of coupling for each combination of residue substitution and inhibitor modification. Figure S3.1 shows two examples of individual mutant cycle analysis. In one case the mutant channel F150A, is paired to compound 6 and the combination produces a large $\Delta\Delta G^o$. In the other case, F150A is paired with compound 9 and the combination produces a $\Delta\Delta G^o \approx 0$. This indicates that phenylalanine 150 interacts with the part of 2GBI molecule modified in compound 6 but not with the part modified in compound 9.

The absolute values of the $\Delta\Delta G^o$ are reported in Fig. 3.3B and their relative values, expressed as percentages of the total binding energy for 2GBI to Hv1 wild type (-25 kJ/mole) are reported in Table S2. The combinations D112E-11, F150A-4, F150A-6, S181A-11, R211S-6, R211S-9 and R211S-11 had relative $|\Delta\Delta G^o|$s $\geq$ 10% of the 2GBI binding energy. The other forty-seven combinations had relative $|\Delta\Delta G^o|$s < 10%. The combinations showing large coupling energy were all consistent with the binding environment shown in Fig. 3.4A in which the bound inhibitor is surrounded by D112, F150, S181, and R211 (shown as spheres with different colors).

When the interaction between a channel mutant and a modified 2GBI molecule is different from the interaction between the wild type channel and 2GBI (high $\Delta\Delta G^o$), the mutated position is indicated with the same color of the modified inhibitor (Fig. 3.4A). Otherwise it is represented in yellow (small $\Delta\Delta G^o$). Binding of compounds 4 and 6 were differentially perturbed in the F150A mutant. This is consistent with an interaction between F150 and the benzo-ring of 2GBI. For compound 6, the binding to R211S was also perturbed, possibly due to the large size of the substituent (Fig. 3.4A, upper right panel).

Binding of compound 9 was differentially perturbed in the R211S mutant, indicating that the guanidine moiety of 2GBI is close to R211. We probed this association also by analyzing the binding of wild type and R211S channels with compound 2. In this 2GBI derivative, the guanidine moiety is modified by cyclization rather than heteroatom substitution as in compound 9 (Fig. S3.3). Both these modifications are expected to reduce the ability of the guanidine moiety to become protonated and to donate hydrogen bonds. Accordingly, we found that the $\Delta\Delta G^o$ value for combinations R211S-2 and R211S-9 were very similar (Table S3.2 and Fig. S3.3).

For compound 11, differential perturbations were measured in the D112E, S181A, and R211S mutants. This finding can be explained by assuming that compound 11 sits in the binding site with the orientation of the oxazole ring shown in Fig. 3.4A (lower right panel) with the ring oxygen facing R211 and S181 and the ring nitrogen facing D112.

To further constrain the possible orientations of 2GBI, we tested whether its guanidine moiety could interact with glutamate 153, the only negatively charged residue beside D112 located in the neighborhood of F150. We examined the binding of 2GBI and compound 9 to wild type and E153C channels and found a $\Delta\Delta G^{o} \approx 0$ (Fig. S3.4). This excludes orientations of the inhibitor that bring the guanidine group in contact with E153.

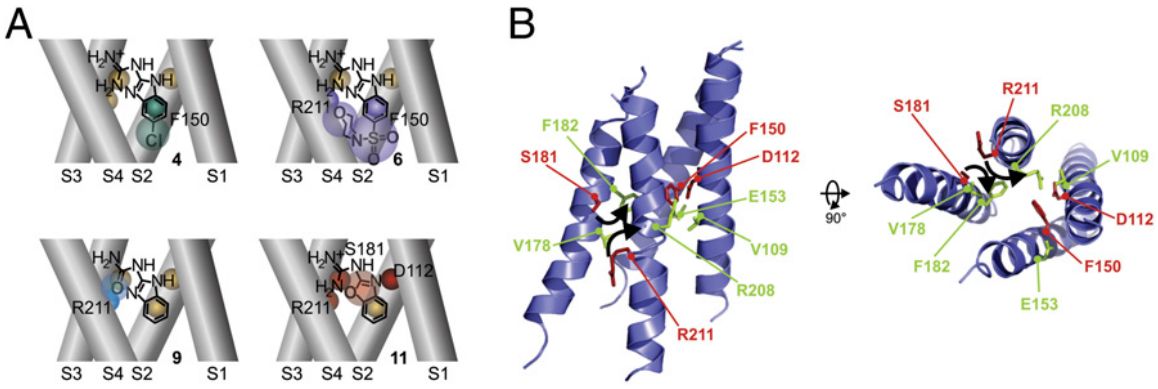

Fig. 3.4. Interpretation of channel–inhibitor interactions. (A) Interpretation of the thermodynamic couplings calculated in Fig. 3B. Simple coupling occur between F150A and compound 4 and between R211S and compound 9 (Left). Simultaneous perturbation of multiple interactions must be invoked to explain the coupling between compounds 6 and 11 with the binding environment (Right). **(B)** Investigated Hv1 residues mapped on the structure of the Hv1-CiVSP chimera (Takeshita et al., 2014). Helix S0 and cytoplasmic coiled-coil domain are not shown for clarity. In *Right*, the VSD is viewed from the intracellular side of the membrane. Amino acid identity refers to human Hv1. Residues involved in 2GBI binding are shown in red. The other residues are shown in green. Black arrows indicate the rearrangements proposed to occur during activation to bring residues S181 and R211 in a position compatible with 2GBI binding (close to F150 and D112).

3.3.3 Enabling Hv1 inhibition by extracellular benzimidazole-guanidine compounds

We have previously found that 2GBI does not produce a reduction in proton current when present in the extracellular medium (Hong et al., 2013). Since the binding site on the channel is intracellular, the compound must partition into the membrane in order to reach it from outside the cell. 2GBI is too polar to do this effectively (predicted logP for non-protonated 2GBI: 0.52). We reasoned that modifications that make 2GBI less polar should

improve membrane partitioning. The modification in compound 4 seemed particularly promising, since it reduces the overall polarity of the molecule (predicted logP non-protonated 4: 1.12), increasing at the same time the apparent affinity for the channel. Other modifications that resulted in more pronounced reductions in polarity (e.g., 9, 11, 12) negatively affected binding affinity.

We tested compound 4 (ClGBI) in outside-out patches from oocytes expressing Hv1 WT and found that the inhibitor can block the channel from the extracellular side of the membrane (Fig. S3.5A, B). The apparent K_d and Hill coefficient for ClGBI extracellular binding were 26.3 ± 2.2 μM and 1.0 ± 0.12, respectively.

We then measured inhibition by ClGBI of native proton currents in microglial BV2 cells, as well as in monocyte/macrophage cells RAW264.7, and THP-1 (Fig. S3.5C – E). These cells were previously shown to express high levels of proton channels (DeCoursey and Cherny, 1996; Sakai et al., 2013; Song et al., 2012). We found that the effect of the inhibitor was very similar in the native channels compared to recombinant Hv1 expressed in oocytes (Fig. S3.5F). These findings suggest that optimization of guanidine derivatives based on the 2GBI scaffold can lead to useful Hv1 inhibitors.

3.4 Discussion

2GBI was previously shown to act as an open channel blocker of Hv1 (Hong et al., 2013). Based on the results of the mutant cycle analysis, we can conclude that when the VSD of

Hv1 opens, 2GBI gets access to the innermost part of the intracellular vestibule and is surrounded by residues D112 in S1, F150 in S2, S181 in S3, and R211 in S4 (Fig. 3.4A). We propose a model of binding in which one of the nitrogen atoms of the imidazole ring interacts with D112 (stabilizing interaction), while the other points toward S181 and R211. The benzo-ring of 2GBI interacts with F150 (destabilizing interaction), and its guanidine moiety points toward R211. The insertion of the imidazole ring between D112 and R211/S181, combined with the non-equivalent interactions between the two nitrogen atoms of the ring and the surrounding protein, provides a simple explanation for why a single heteroatom replacement in compound 11 is coupled to three different positions in the channel located on opposite sides of the binding site (Fig. 3.4A, lower right panel). Previous studies have proposed the existence of water wires inside the open Hv1 channel (Ramsey et al., 2010; Wood et al., 2012). Therefore, some of the observed interactions between 2GBI and the channel may be mediated by water molecules in the VSD. Aspartate at position 112 has been shown to be the selectivity filter of Hv1 (Musset et al., 2011). By interacting directly with this residue, 2GBI could change its pK_a to values incompatible with effective proton permeation. Alternatively, the inhibitor could physically break the hydrogen bonded chain required to deliver protons from the VSD's intracellular vestibule to D112. An earlier study proposed that, in the open state, D112 and R211 are close enough to interact electrostatically (Berger and Isacoff, 2011).

Our results are consistent with this conclusion. Other studies on the VSDs of voltage-gated potassium channels have concluded that the conserved phenylalanine corresponding to F150 interacts with different S4 arginines in different conformations (Lacroix and

Bezanilla, 2011; Tao et al., 2010). Our findings indicate that R211 is close to F150 in the open state, which is consistent with other studies in which the accessibility of the S4 arginine to the intracellular solution was assessed in the closed and open conformations (Gonzalez et al., 2010; Kulleperuma et al., 2013).

Recently, the crystal structure of a chimera between Hv1 and the voltage-sensitive phosphatase CiVSP has been solved (Takeshita et al., 2014). Even though the channel appears to be in a non-conducting closed conformation, a relatively wide intracellular vestibule extends deep inside the VSD and contacts F150. The existence of a similar intracellular vestibule was recently reported in an Hv1 model based on the crystal structure of the CiVSP's VSD (Li et al., 2014). This vestibule is likely to be the pathway that 2GBI follows to reach its binding site from the intracellular medium. The crystallized channel also shows a small cavity on top of F150 and D112 followed by an extracellular constriction (Takeshita et al., 2014). If this constriction is maintained in the open state, it can explain why 2GBI is not able to reach its binding site from the extracellular medium.

We mapped the residues involved in 2GBI binding on the crystal structure of the Hv1-CiVSP chimera and show them in red in Fig. 3.4B. F150 and D112 are located close to each other and in the proximity of the intracellular vestibule, a position consistent with our 2GBI binding model. On the other hand, the residues in S3 and S4 facing F150 and D112 are F182 and R208, two of the positions tested that do not participate in 2GBI binding (shown in green in Fig. 3.4B). This suggests that when the channel transitions from the closed conformation, represented in the structure, to the open conformation capable of binding

2GBI, residues F182 and R208 change their positions with respect to F150 and D112. If in the open conformation, S181 takes the place of F182, and R211 takes the place of R208 (black arrows in Fig. 3.4B), all four residues involved in 2GBI binding can face the center of the VSD and interact with the inhibitor. This structural rearrangement is compatible with the mechanism of voltage-driven activation of CiVSP proposed by Li et al. (Li et al., 2014).

The high polarity of 2GBI limits its potential as an Hv1 inhibitor due to its inefficient partitioning into the membrane. Appending a hydrophobic group to the guanidine moiety could be a way to increase the lipophilic nature of the molecule. However, our results indicate that there is no space in the binding site to accommodate such a group. Accordingly, a 2GBI analog with this kind of modification proved to be a poor Hv1 blocker (compound 12, Fig. 3.1A & D). On the other hand, substituents at the benzo-ring of 2GBI seem to be much better tolerated (compounds 4 – 6, Fig 3.1A & D) and the 5-chloro-substitution resulted in an increase in apparent binding affinity. In our binding model, the benzo-ring is located in a region of the intracellular vestibule that is wide enough to accommodate large groups. The walls of the vestibule could provide an interacting surface for larger 2GBI analogs, resulting in stronger binding.

The ability of ClGBI to inhibit both recombinant and native proton channels from the extracellular medium (Fig. S3.5) suggests that guanidine derivatives based on the 2GBI scaffold could be optimized to reduce the pathological effects of excessive Hv1 activity in ischemic stroke and cancer.

3.5 Supplementary Information

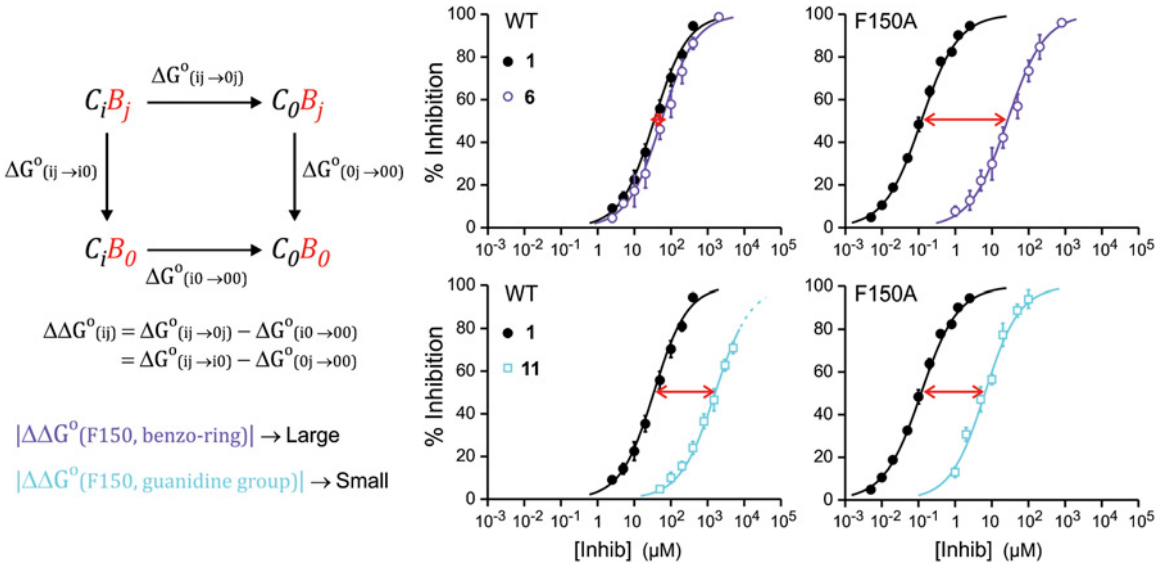

Fig. S3.1. Examples of mutant cycle analysis applied to position F150. Red arrows indicate the separations between the inhibition curves for modified and unmodified inhibitor. When the separation in the mutant channel is different from the separation in the WT channel, jΔΔGoj is larger than zero. In the case of compound 6, the difference in separation is large, and therefore, jΔΔGoj is large. This result is considered indicative of an interaction between F150 and the benzo ring of the inhibitor (modified in compound 6). In the case of compound 11, the difference in separation is negligible, and therefore, jΔΔGoj is negligible. This result indicates that F150 does not interact with the guanidine group of the inhibitor (modified in compound 11). Bj, inhibitor with unmodified benzo ring or guanidine group; B0, inhibitor with modified benzo ring (compound 6) or modified guanidine group (compound 11); Ci, Hv1 F150; C0, Hv1 F150A. Fig. 3.3A has additional details.

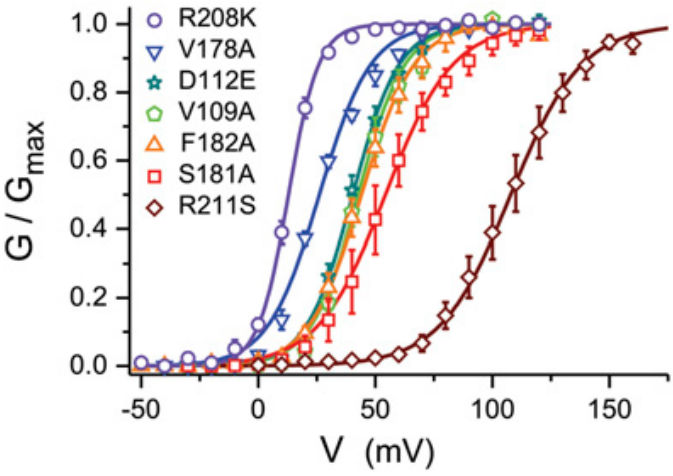

	$V_{1/2}$ (mV)	Slope (mV)
V109A	42.6 ± 1.7	10.0 ± 1.0
D112E	40.4 ± 1.9	9.9 ± 0.3
F150A	29.0 ± 2.8	10.7 ± 0.3
E153C	-1.6 ± 3.6	11.4 ± 1.3
V178A	26.1 ± 0.8	11.2 ± 1.1
S181A	52.7 ± 4.8	12.5 ± 1.7
F182A	44.0 ± 2.8	11.2 ± 1.0
R208K	12.9 ± 0.9	6.5 ± 0.4
R211S	107.9 ± 4.6	15.1 ± 2.2
WT	53.1 ± 2.3	10.9 ± 0.8

Fig. S3.2. Voltage dependence of activation of Hv1 channels tested for inhibition by guanidine derivatives. Conductance vs. voltage relationships were determined as previously described (1) from proton currents recorded in inside-out patches. pHo = pHi = 6.0. Error bars are SEM (n ≥ 4). Curved lines are

Boltzmann fits of the data. Fit parameters are reported in Right. V1/2 and slope values for mutants F150A and E153C and Hv1 WT are from previously published works {Tombola:2010kb, Hong:2013bv} and provided here as reference (gray).

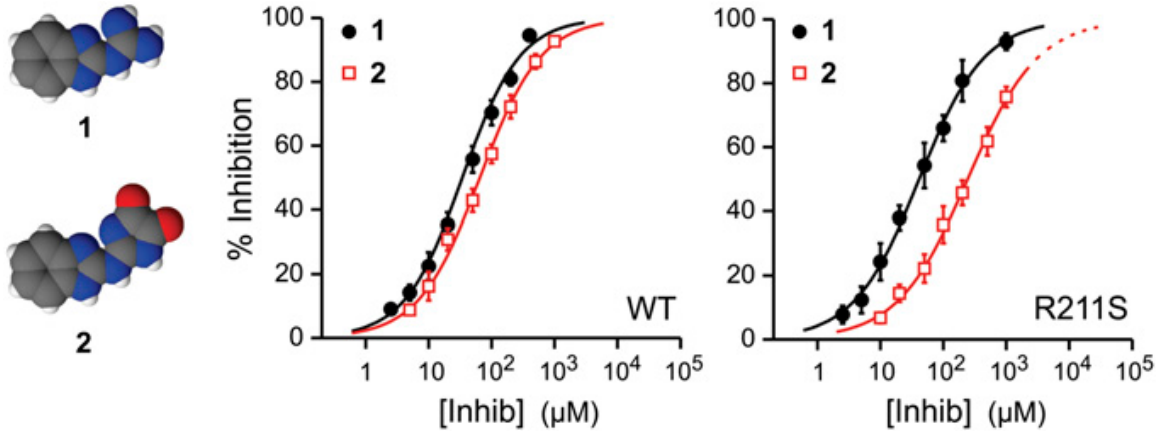

Fig. S3.3. Interaction between the guanidine group of 2-guanidinobenzimidazole (2GBI) and R211 probed with compound 2. Dose–response curves for the inhibition of Hv1 WT and R211S produced by the indicated compounds. Each point represents the average inhibition from three to six measurements ± SD. Curved lines are Hill fits. Fit parameters for compound 1 are reported in Table S1. Fit parameters for compound 2 are Kd = 65.1 ± 3.2 μM and h = 0.89 ± 0.03 for WT and Kd = 244 ± 12 μM and h = 0.78 ± 0.03 for R211S. The dotted line in *Right* represents extrapolation into a concentration range where compound 2 has low solubility. The coupling free energy value for R211 and the guanidine group of the inhibitor was 2.79 ± 0.28 kJ/mol (ΔΔGo/ΔGo b = −11.0 ± 1.1%).

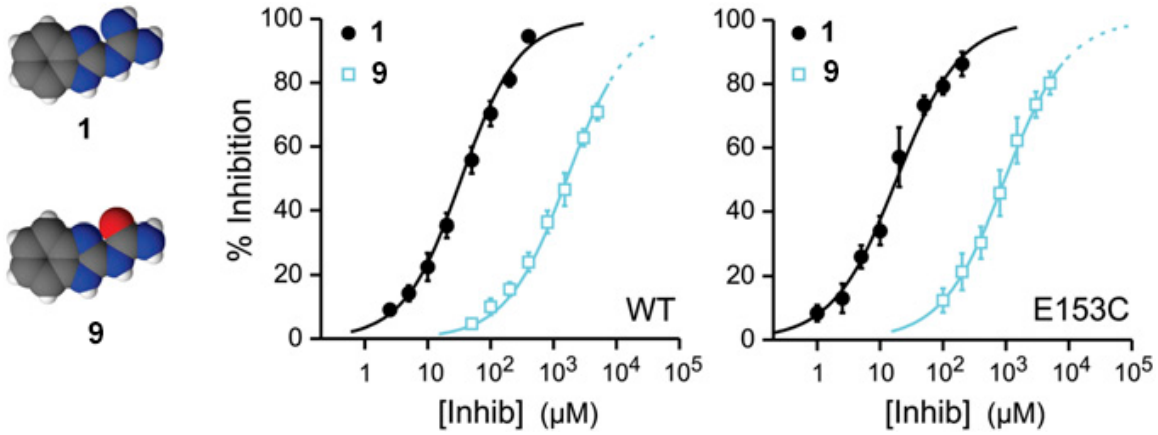

Fig. S3.4. Lack of interaction between the guanidine group of 2GBI and E153 probed with compound 9. Dose–response curves for the inhibition of Hv1 WT and E153C produced by the indicated compounds. Each point represents the average inhibition from three to eight measurements ± SD. Curved lines are Hill fits. Fit parameters for Hv1 WT are reported in Table S1. Fit parameters for E153C are Kd = 18.2 ± 1.2 μM and h = 0.85 ± 0.04 for compound 1 and Kd = 955 ± 26 μM and h = 0.87 ± 0.02 for compound 9. Dotted lines represent extrapolation into a concentration range where compound 9 has low solubility. The coupling free energy value for E153 and the guanidine group of the inhibitor was 0.23 ± 0.29 kJ/mol (ΔΔGo/ΔGo b = −0.9 ± 1.1%).

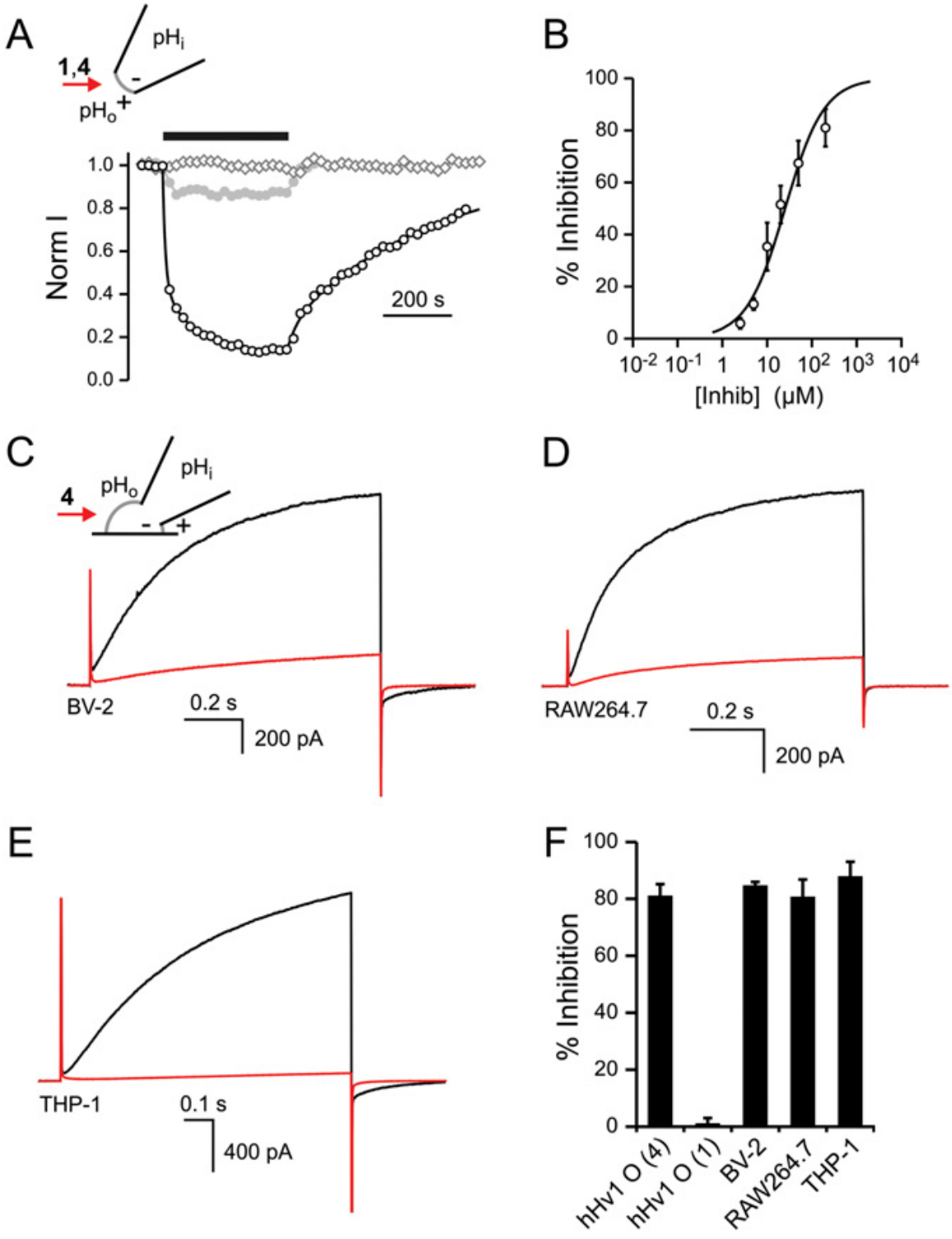

Fig. S3.5. Inhibition of recombinant and native proton channels by a membrane-permeant 2GBI analog. (A) Time courses of Hv1 inhibition by compounds 1 (2GBI) and 4 (ClGBI) added to the extracellular side of the membrane. Proton currents were measured in outside-out patches from oocytes expressing human Hv1 on depolarization to +120 mV from a holding potential of −80 mV. pH_i was 6.0, and pH_o was 7.5. Horizontal black bar indicates the presence of 200 μM inhibitor in the bath solution (gray open diamonds, 200 μM 2GBI; gray filled circles, 5 μM ClGBI; black open circles, 200 μM ClGBI). Points were fitted by

exponential functions for inhibition and recovery (black curves; in the text). **(B)** Dose–response curve of Hv1 inhibition by extracellular ClGBI. Reductions in proton current were measured as a function of inhibitor concentration in outside-out patches as in A. Each point represents the average inhibition from three to four measurements ± SD. Black curve is the Hill fit. Parameters are in the text. **(C–E)** Effect of extracellular ClGBI on native proton currents measured in microglial BV-2 cells and monocyte/macrophage cells RAW264.7 and THP-1. Whole-cell currents were recorded in the absence (black) and presence (red) of 200 μM ClGBI in the bath under the same conditions used in A. **(F)** Quantification of proton channel inhibition by extracellular ClGBI (200 μM). The effect of the same concentration of extracellular 2GBI on Hv1 currents measured in oocytes (O) is provided for comparison. Bars are averages ± SEM (n ≥ 3).

Table S3.1. Fit parameters for dose-response curves shown in Fig. 3A

	1		4		6		8		9		11	
Channel	K_d (μM)	*h*	K_d (μM)	*h*	K_d (μM)	*h*	K_d (μM)	*h*	K_d (μM)	*h*	K_d (μM)	*h*
WT	34.3±2.5	0.95±0.05	1.55±0.07	0.96±0.04	54.3±3.7	0.93±0.04	62.3±2.4	1.02±0.03	1630±99	0.90±0.03	7400±1200	1.00±0.13
V109A	22.1±1.6	0.90±0.03	1.20±0.10	0.90±0.06	46.1±1.9	0.93±0.02	28.5±1.7	0.87±0.03	1230±82	0.77±0.05	3280±230	0.93±0.04
D112E	191±8	1.03±0.03	13.9±0.9	0.99±0.05	148±5	0.92±0.02	230±9	0.89±0.03	5800±290	0.90±0.04	3900±650	1.00±0.19
F150A	0.118±0.007	0.86±0.03	0.061±0.003	1.00±0.03	26.3±2.2	0.86±0.04	0.126±0.005	0.87±0.02	6.5±0.6	0.92±0.07	16.5±1.1	0.94±0.04
V178A	13.14±0.39	0.81±0.02	0.660±0.046	0.90±0.04	30.2±4.2	0.84±0.07	22.5±0.6	0.95±0.02	694 ±16	0.76±0.01	2500±150	0.80±0.04
S181A	51.9±2.4	0.87±0.03	3.16±0.24	1.04±0.06	71±5	0.80±0.03	104±8	0.98±0.05	2500±120	0.77±0.02	2520±200	1.00±0.07
F182A	23.8±1.9	0.93±0.04	1.41±0.11	0.96±0.05	29.8±1.4	0.85±0.03	33.5±1.7	0.96±0.03	1240±130	0.82±0.06	2580±290	0.94±0.09
R208K	33.6±1.3	0.84±0.02	2.05±0.16	0.99±0.05	47.2±0.9	0.90±0.01	59.2±2.6	1.02±0.03	1900±310	0.90±0.11	6100 ±2700	1.00±0.25
R211S	41.3±2.1	0.84±0.03	2.09±0.11	0.97±0.03	188±12	0.85±0.03	57.8±3.9	0.96±0.04	5600±260	0.94±0.03	1330±80	1.00±0.06

Table S3.2. Coupling free energy values for the indicated combinations of channel mutations and inhibitor modifications expressed as percentage of the apparent free energy of binding of 2GBI to Hv1 WT.

	4	6	8	9	11
Channel	$\Delta\Delta G^o/\Delta G^o_b$ (%)				
V109A	-1.7±1.2	-2.6±1.3	3.4±1.2	-1.5±1.3	3.6±1.9
D112E	-4.6±1.1	6.9±1.1	4.0±1.0	4.3±1.1	**22.9±2.4**
F150A	**-23.7±1.1**	**-48.1±1.4**	5.2±1.0	-1.4±1.4	4.2±1.9
V178A	-1.0±1.1	-3.6±1.7	0.6±0.9	-1.0±1.0	1.2±1.8
S181A	-2.9±1.2	1.5±1.3	-0.9±1.2	-0.1±1.1	**14.5±1.9**
F182A	-2.7±1.4	2.3±1.3	2.5±1.2	-0.9±1.6	6.7±2.1
R208K	-2.9±1.2	1.2±1.0	0.3±1.0	-1.5±1.9	1.7±4.6
R211S	-1.1±1.1	**-10.3±1.2**	2.6±1.1	**-10.2±1.1**	**18.5±1.9**

Table S3. Highest tested concentrations for the indicated compounds and relative percentages of channel inhibition.

Channel	**[1]**$_{max}$ (mM)	$\%_{inhib}$	**[4]**$_{max}$ (mM)	$\%_{inhib}$	**[6]**$_{max}$ (mM)	$\%_{inhib}$	**[8]**$_{max}$ (mM)	$\%_{inhib}$	**[9]**$_{max}$ (mM)	$\%_{inhib}$	**[11]**$_{max}$ (mM)	$\%_{inhib}$
WT	0.4	94.5±1.4	0.02	93.6±1.1	2	98.7±0.6	2	97.3±1.2	5	70.8±2.6	4	36.6±4.4
V109A	1	97.7±0.6	0.05	98.7±0.6	0.8	93.7±1.5	2	98.0±1.0	5	77.7±2.8	4	54±6
D112E	2	91.2±2.6	0.2	94.0±3.6	4	95.7±2.5	4	90.7±0.6	5	46±8	4	50.7±4.8
F150A	0.0025	94.5±1.3	0.001	96.0±1.1	0.8	96.0±1.0	0.005	96.7±3.2	0.1	94.0±4.2	0.2	92.7±1.7
V178A	0.5	95.7±2.5	0.02	96.7±1.5	1	98.0±1.7	1	97.3±2.1	5	81.7±2.1	4	59.±7
S181A	1	94.5±3.1	0.05	94.5±3.1	2	96.8±2.1	4	94.0±2.6	5	64±6	4	62.3±4.2
F182A	1	97.0±2.6	0.02	95.0±2.9	2	98.0±1.0	2	96.7±4.0	5	79.5±3.3	4	63.1±3.9
R208K	1	95.8±1.7	0.05	97.3±1.5	2	96.3±1.0	2	95.8±3.2	5	70.6±4.6	4	45±9
R211S	1	93.0±2.6	0.05	95.0±2.6	4	93.3±1.2	2	93.7±3.8	5	48±6	4	77±1.6

Supplementary Methods

Channel Mutants

Expression of Hv1 mutants with alanine substitutions at positions 109, 150, 178, 181, and 182 provided strong proton currents similar in size to the WT channel (Fig. 3.2B). We

mutated R211 to serine, because the substitution was previously shown to be well-tolerated by the protein {Berger:2011dz}. Neutralizing mutation of charged residues D112 and R208 proved to be highly perturbative, which was previously reported {Musset:2011bf, Kulleperuma:2013hb}. Currents measured from any of the alanine-, asparagine-, or glutamine substituted channels at these positions were too small for reliable measurement of inhibition. However, conservative substitutions D112E, and R208K produced functioning channels, with current levels comparable with WT.

Mutant Cycle Analysis

In mutant cycle analysis, mutations that cause large changes in Kd of related compounds do not necessarily produce large ΔΔGo values. Only mutations that cause different changes in channel affinity for related compounds can produce large ΔΔGo values (Fig. S3.1). Mutations that alter binding affinity by long-range perturbations, such as overall backbone structure of a helix, are more likely to produce generalized effects on binding rather than selective effects on individual inhibitors. If a mutation produces the same change in Kd for all of the related compounds, all of the ΔΔGo values associated with it will be ~0. As a result, the mutated residue cannot be confirmed to be part of the binding site. This reduces the occurrence of false positives. However, it does not completely eliminate the possibility.

3.6 References

Berger, T.K., and Isacoff, E.Y. (2011). The pore of the voltage-gated proton channel. Neuron *72*, 991–1000.

Börjesson, S.I., and Elinder, F. (2011). An electrostatic potassium channel opener targeting the final voltage sensor transition. J. Gen. Physiol. *137*, 563–577.

Capasso, M., Bhamrah, M.K., Henley, T., Boyd, R.S., Langlais, C., Cain, K., Dinsdale, D., Pulford, K., Khan, M., Musset, B., et al. (2010). HVCN1 modulates BCR signal strength via regulation of BCR-dependent generation of reactive oxygen species. Nat. Immunol. *11*, 265–272.

Chemaly, El, A., Okochi, Y., Sasaki, M., Arnaudeau, S., Okamura, Y., and Demaurex, N. (2010). VSOP/Hv1 proton channels sustain calcium entry, neutrophil migration, and superoxide production by limiting cell depolarization and acidification. Journal of Experimental Medicine *207*, 129–139.

DeCoursey, T.E., and Cherny, V.V. (1996). Voltage-activated proton currents in human THP-1 monocytes. J Membrane Biol *152*, 131–140.

Decoursey, T.E. (2013). Voltage-gated proton channels: molecular biology, physiology, and pathophysiology of the H(V) family. Physiol. Rev. *93*, 599–652.

Decoursey, T.E., Morgan, D., and Cherny, V.V. (2003). The voltage dependence of NADPH oxidase reveals why phagocytes need proton channels. Nature *422*, 531–534.

Fujiwara, Y., Kurokawa, T., Takeshita, K., Kobayashi, M., Okochi, Y., Nakagawa, A., and Okamura, Y. (2012). The cytoplasmic coiled-coil mediates cooperative gating temperature sensitivity in the voltage-gated H(+) channel Hv1. Nat Commun *3*, 816.

Gonzalez, C., Koch, H.P., Drum, B.M., and Larsson, H.P. (2010). Strong cooperativity between subunits in voltage-gated proton channels. Nat. Struct. Mol. Biol. *17*, 51–56.

Gonzalez, C., Rebolledo, S., Perez, M.E., and Larsson, H.P. (2013). Molecular mechanism of voltage sensing in voltage-gated proton channels. J. Gen. Physiol. *141*, 275–285.

Hidalgo, P., and MacKinnon, R. (1995). Revealing the architecture of a K+ channel pore through mutant cycles with a peptide inhibitor. Science *268*, 307–310.

Hille, B. (2001). Ion Channels of Excitable Membranes (Sunderland: Sinauer Associates Inc).

Hong, L., Pathak, M.M., Kim, I.H., Ta, D., and Tombola, F. (2013). Voltage-sensing domain of voltage-gated proton channel Hv1 shares mechanism of block with pore domains. Neuron *77*, 274–287.

Horovitz, A., and Fersht, A.R. (1990). Strategy for analysing the co-operativity of intramolecular interactions in peptides and proteins. J. Mol. Biol. *214*, 613–617.

Koch, H.P., Kurokawa, T., Okochi, Y., Sasaki, M., Okamura, Y., and Larsson, H.P. (2008). Multimeric nature of voltage-gated proton channels. Proc. Natl. Acad. Sci. U.S.a. *105*, 9111–9116.

Kulleperuma, K., Smith, S.M.E., Morgan, D., Musset, B., Holyoake, J., Chakrabarti, N., Cherny, V.V., Decoursey, T.E., and Pomès, R. (2013). Construction and validation of a homology model of the human voltage-gated proton channel hHV1. J. Gen. Physiol. *141*, 445–465.

Lacroix, J.J., and Bezanilla, F. (2011). Control of a final gating charge transition by a hydrophobic residue in the S2 segment of a K+ channel voltage sensor. Proc. Natl. Acad. Sci. U.S.a. *108*, 6444–6449.

Lee, S.-Y., Letts, J.A., and Mackinnon, R. (2008). Dimeric subunit stoichiometry of the human voltage-dependent proton channel Hv1. Proc. Natl. Acad. Sci. U.S.a. *105*, 7692–7695.

Li, P., Chen, Z., Xu, H., Sun, H., Li, H., Liu, H., Yang, H., Gao, Z., Jiang, H., and Li, M. (2013). The gating charge pathway of an epilepsy-associated potassium channel accommodates chemical ligands. Cell Res. *23*, 1106–1118.

Li, Q., Wanderling, S., Paduch, M., Medovoy, D., Singharoy, A., McGreevy, R., Villalba-Galea, C.A., Hulse, R.E., Roux, B., Schulten, K., et al. (2014). Structural mechanism of voltage-dependent gating in an isolated voltage-sensing domain. Nat. Struct. Mol. Biol. *21*, 244–252.

Li, S.J., Zhao, Q., Zhou, Q., Unno, H., Zhai, Y., and Sun, F. (2010). The role and structure of the carboxyl-terminal domain of the human voltage-gated proton channel Hv1. J. Biol. Chem. *285*, 12047–12054.

Liman, E.R., Tytgat, J., and Hess, P. (1992). Subunit stoichiometry of a mammalian K+ channel determined by construction of multimeric cDNAs. Neuron *9*, 861–871.

Morgan, D., Musset, B., Kulleperuma, K., Smith, S.M.E., Rajan, S., Cherny, V.V., Pomès, R., and Decoursey, T.E. (2013). Peregrination of the selectivity filter delineates the pore of the human voltage-gated proton channel hHV1. J. Gen. Physiol. *142*, 625–640.

Murata, Y., Iwasaki, H., Sasaki, M., Inaba, K., and Okamura, Y. (2005). Phosphoinositide phosphatase activity coupled to an intrinsic voltage sensor. Nature *435*, 1239–1243.

Musset, B., Smith, S.M.E., Rajan, S., Morgan, D., Cherny, V.V., and Decoursey, T.E. (2011). Aspartate 112 is the selectivity filter of the human voltage-gated proton channel. Nature *480*, 273–277.

Peretz, A., Pell, L., Gofman, Y., Haitin, Y., Shamgar, L., Patrich, E., Kornilov, P., Gourgy-Hacohen, O., Ben-Tal, N., and Attali, B. (2010). Targeting the voltage sensor of Kv7.2 voltage-gated K+ channels with a new gating-modifier. Proc. Natl. Acad. Sci. U.S.a. *107*, 15637–15642.

Ramsey, I.S., Mokrab, Y., Carvacho, I., Sands, Z.A., Sansom, M.S.P., and Clapham, D.E. (2010).

An aqueous H+ permeation pathway in the voltage-gated proton channel Hv1. Nat. Struct. Mol. Biol. *17*, 869–875.

Ramsey, I.S., Moran, M.M., Chong, J.A., and Clapham, D.E. (2006). A voltage-gated proton-selective channel lacking the pore domain. Nature *440*, 1213–1216.

Ramsey, I.S., Ruchti, E., Kaczmarek, J.S., and Clapham, D.E. (2009). Hv1 proton channels are required for high-level NADPH oxidase-dependent superoxide production during the phagocyte respiratory burst. Proc. Natl. Acad. Sci. U.S.a. *106*, 7642–7647.

Sakai, H., Li, G., Hino, Y., Moriura, Y., Kawawaki, J., Sawada, M., and Kuno, M. (2013). Increases in intracellular pH facilitate endocytosis and decrease availability of voltage-gated proton channels in osteoclasts and microglia. The Journal of Physiology *591*, 5851–5866.

Sasaki, M., Takagi, M., and Okamura, Y. (2006). A voltage sensor-domain protein is a voltage-gated proton channel. Science *312*, 589–592.

Song, J.-H., Marszalec, W., Kai, L., Yeh, J.Z., and Narahashi, T. (2012). Antidepressants inhibit proton currents and tumor necrosis factor-α production in BV2 microglial cells. Brain Res. *1435*, 15–23.

Swartz, K.J., and MacKinnon, R. (1995). An inhibitor of the Kv2.1 potassium channel isolated from the venom of a Chilean tarantula. Neuron *15*, 941–949.

Takeshita, K., Sakata, S., Yamashita, E., Fujiwara, Y., Kawanabe, A., Kurokawa, T., Okochi, Y., Matsuda, M., Narita, H., Okamura, Y., et al. (2014). X-ray crystal structure of voltage-gated proton channel. Nat. Struct. Mol. Biol.

Tao, X., Lee, A., Limapichat, W., Dougherty, D.A., and Mackinnon, R. (2010). A gating charge transfer center in voltage sensors. Science *328*, 67–73.

Tetko, I.V., Gasteiger, J., Todeschini, R., Mauri, A., Livingstone, D., Ertl, P., Palyulin, V.A., Radchenko, E.V., Zefirov, N.S., Makarenko, A.S., et al. (2005). Virtual computational chemistry laboratory--design and description. J. Comput. Aided Mol. Des. *19*, 453–463.

Tombola, F., Ulbrich, M.H., and Isacoff, E.Y. (2008). The voltage-gated proton channel Hv1 has two pores, each controlled by one voltage sensor. Neuron *58*, 546–556.

Wang, J., Yarov-Yarovoy, V., Kahn, R., Gordon, D., Gurevitz, M., Scheuer, T., and Catterall, W.A. (2011). Mapping the receptor site for alpha-scorpion toxins on a Na+ channel voltage sensor. Proc. Natl. Acad. Sci. U.S.a. *108*, 15426–15431.

Wang, Y., Li, S.J., Wu, X., Che, Y., and Li, Q. (2012). Clinicopathological and biological significance of human voltage-gated proton channel Hv1 protein overexpression in breast cancer. J. Biol. Chem. *287*, 13877–13888.

Wang, Y., Wu, X., Li, Q., Zhang, S., and Li, S.J. (2013). Human voltage-gated proton channel hv1: a new potential biomarker for diagnosis and prognosis of colorectal cancer. PLoS ONE *8*, e70550.

Wood, M.L., Schow, E.V., Freites, J.A., White, S.H., Tombola, F., and Tobias, D.J. (2012). Water wires in atomistic models of the Hv1 proton channel. Biochim. Biophys. Acta *1818*, 286–293.

Wu, L.-J., Wu, G., Akhavan Sharif, M.R., Baker, A., Jia, Y., Fahey, F.H., Luo, H.R., Feener, E.P., and Clapham, D.E. (2012). The voltage-gated proton channel Hv1 enhances brain damage from ischemic stroke. Nat. Neurosci. *15*, 565–573.

Wulff, H., Castle, N.A., and Pardo, L.A. (2009). Voltage-gated potassium channels as therapeutic targets. Nat Rev Drug Discov *8*, 982–1001.

Yu, F.H., and Catterall, W.A. (2004). The VGL-chanome: a protein superfamily specialized for electrical signaling and ionic homeostasis. Sci. STKE *2004*, re15.

Chapter 4: Functional diversity between the voltage-gated proton channel Hv1 and its closest related protein HVRP1

(Kim, Hevezi, Varga, Pathak, Hong, Ta, Zlotnik, Soltesz, Tombola)

Abstract

The Hv1 channel and voltage-sensitive phosphatases share with voltage-gated sodium, potassium, and calcium channels the ability to detect changes in membrane potential through voltage-sensing domains (VSDs). However, they lack the pore domain typical of these other channels. Na_V, K_V, and Ca_V proteins can be found in neurons and muscles, where they play important roles in electrical excitability. In contrast, VSD-containing proteins lacking a pore domain are found in non-excitable cells and are not involved in neuronal signaling. Here, we report the identification of HVRP1, a protein related to the Hv1 channel (from which the name Hv1 Related Protein 1 is derived), which we find to be expressed primarily in the central nervous system, and particularly in the cerebellum. Within the cerebellar tissue, HVRP1 is specifically expressed in granule neurons, as determined by in situ hybridization and immunohistochemistry. Analysis of subcellular distribution via electron microscopy and immunogold labeling reveals that the protein localizes on the post-synaptic side of contacts between glutamatergic mossy fibers and the granule cells. We also find that, despite the similarities in amino acid sequence and structural organization between Hv1 and HVRP1, the two proteins have distinct functional properties.

The high conservation of HVRP1 in vertebrates and its cellular and subcellular localizations suggest an important function in the nervous system.

4.1 Introduction

The molecular devices responsible for the generation and propagation of electrical signals in excitable tissues are proteins containing voltage-sensing domains (VSDs) (Yu and Catterall, 2004). Malfunction of such proteins is the cause of several neurological and cardiovascular diseases, such as epilepsy, episodic ataxia, migraine, periodic paralysis, and cardiac arrhythmia (Ashcroft, 1999). VSDs are four-transmembrane-segment structural units whose function is to turn on and off biological processes in response to changes in cell membrane potential. In most VSD-containing proteins, such as voltage-gated sodium, potassium, and calcium channels, the voltage sensor controls the opening and closing of an ion-conducting pore domain (Fig. 4.1A). Only recently have VSDs been recognized to perform other functions besides controlling pore domains. Two classes of proteins have been identified so far, which contain VSDs but do not possess pore domains: voltage-sensitive phosphatases (VSPs) (Murata et al., 2005) and voltage-gated proton (Hvs) channels (Ramsey et al., 2006; Sasaki et al., 2006).

In the first class, the VSD is connected to a cytoplasmic enzymatic domain that turns on when the membrane is depolarized and dephosphorylates phosphatidylinositol (PI) lipids (Kohout et al., 2010; Murata et al., 2005) (Fig. 4.1A). CiVSP from *Ciona intestinalis* has been characterized in detail (Li et al., 2014) and proven to be a useful tool to change PI-4,5-bisphosphate concentration in cells in a voltage dependent manner, e.g. (Suh et al., 2010;

Yudin et al., 2011). Its human homologs (TPTE and TPTE2/TPIP (Tapparel et al., 2003; Walker et al., 2001; Wu et al., 2001)) have been reported to be associated with intracellular compartments (Walker et al., 2001; Wu et al., 2001). Based on their catalytic activity and tissue distribution, voltage-sensitive phosphatases have been proposed to play a role in linking changes in membrane potential to phosphoinositide signaling pathways in non-excitable cells (Neuhaus and Hollemann, 2009; Okamura, 2007; Ratzan et al., 2011).

In the second class, represented by the voltage-gated proton channel Hv1 (Ramsey et al., 2006; Sasaki et al., 2006) (a.k.a. HVCN1 or VSOP), the VSD acts both as a sensor of membrane potential and as an ion conducting unit, allowing protons to permeate the membrane upon depolarization (Fig. 4.1A). Hv1 forms dimers in which each VSD subunit has its own proton pore and gate (Koch et al., 2008; Lee et al., 2008; Tombola et al., 2008). Its cytoplasmic C-terminal coiled-coil domain (Fujiwara et al., 2012; Li et al., 2010) is responsible for dimerization, and the two Hv1 subunits open cooperatively (Gonzalez et al., 2010; Musset et al., 2010; Tombola et al., 2010). Hv1 is known to play important roles in various non-excitable tissues, where it counteracts intracellular proton accumulation and regulates the production of reactive oxygen species (ROS) by NOX enzymes (Decoursey, 2013). In the brain, the channel is expressed in the microglia (Okochi et al., 2009; Wu et al., 2012), and its excessive activity has been shown to worsen recovery from ischemic (Wu et al., 2012) stroke.

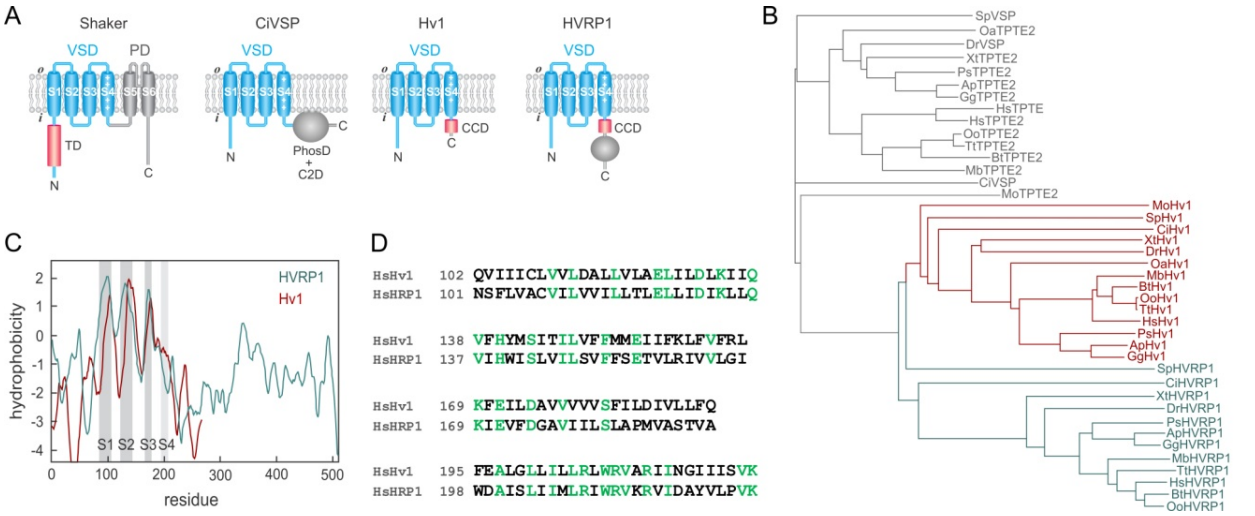

Figure 4.1. Relationship between HVRP1 and other VSD-containing proteins. (A) Modular organization of HVRP1 compared to known voltage sensing proteins. The Shaker potassium channel was chosen as an example of protein containing both a VSD and a pore domain. C2D: C2 domain, CCD: coiled-coil domain, PhosD: phosphatase domain, PD: pore domain, TD: tetramerization domain. **(B)** Phylogram showing amino acid sequence relationship between VSP/TPTE/TPTE2 phosphatases (gray), Hv1 channels (red), and HVRP1 proteins (teal). See Methods for details. Ap: *Anas platyrhynchos*, Bt: *Bos taurus*, Ci: *Ciona intestinalis*, Dr: *Danio rerio*, Gg: *Gallus gallus*, Hs: *Homo sapiens*, Mb: *Myotis brandtii*, Mo: *Metaseiulus occidentalis*, Oa: *Ornithorhynchus anatinus*, Oo: *Orcinus orca*, Ps: *Pelodiscus sinensis*, Sp: *Strongylocentrotus purpuratus*, Tt: *Tursiops truncates*, Xt: *Xenopus tropicalis*. **(C)** Hydrophobicity plot (generated with TopPred, Institute Pasteur, (Heijne, 1992)), comparing human Hv1 and HVRP1 and showing relative positions of transmembrane helices S1-S4 (identified with SOSUI, Nagoya University, (Hirokawa et al., 1998)). **(D)** Sequence alignment of human Hv1 and HVRP1. Only regions containing segments S1 through S4 are shown.

Proton currents from molecularly unidentified voltage-gated channels were first recorded in snail neurons more than thirty years ago (Thomas and Meech, 1982). These currents resemble those produced by vertebrate Hv1 channels. However, there is strong evidence that Hv1 is not a neuronal protein in vertebrates (Okochi et al., 2009; Ramsey et al., 2009; Wu et al., 2012). We wondered whether VSD-containing proteins similar to Hv1 could exist in vertebrate neurons and play a role in cell electrical excitability.

Using a combination of bioinformatics, gene expression profiling, *in situ* hybridization, immunohistochemistry, electron microscopy, and electrophysiology we identified the

product of the gene *C15ORF27* as a neuronal VSD-containing protein lacking the pore domain related to the Hv1 channel. We refer to this protein as HVRP1 (*HV*1 *R*elated *P*rotein 1). Based on the cellular and subcellular localization of the protein, and the functional comparison between Hv1, HVRP1, and chimeras made of parts of the two proteins, we propose that HVRP1 plays a role in the modulation of postsynaptic excitability in cerebellar granule neurons, and that despite its sequence similarity to the Hv1 channel, its function does not involve VSD-mediated ion permeation.

A major function of the cerebellum has been well established since the 1800s as coordinating movement. Though it alone does not control muscle movement, the cerebellum functions by associating with other systems of motor control. It has long been known that removal of or damage to the cerebellum causes partial or total incoordination even though the muscles are not paralyzed in any way. Without proper cerebellum function, patients can still perform certain slow movements, but rapid coordination is not possible (Hall and Guyton, 2010). In more recent years it has been shown that the cerebellum is also important for some types of cognitive functions, such as thought, behavior, and emotion (Schmahmann and Sherman, 1998). The cerebellum's most studied function, however, is in helping provide rapid signals for agonist muscles to turn on and simultaneous signals for antagonist muscles to turn off at the initiation of movement, allowing rapid and smooth transitions between movements (Hall and Guyton, 2010). It is a plausible hypothesis therefore that the novel protein HVRP1, as it is specifically expressed in the cerebellum, may be involved in these cerebellar functions such as the coordination of movement.

The composition of the cerebellum is in three regions, the cerebellar cortex, the inner white matter, and the deep cerebellar nuclei. The cerebellar cortex is further divided into three major layers. Outside is the molecular layer, with basket and stellate interneurons. This layer also contains the most distal regions of the cerebellar granule neurons and Purkinje cell dendrites. The cell bodies of these neurons are in the layer below, the Purkinje neuron layer. Then, the deepest layer of the cerebellar cortex is the granule cell layer, where the cerebellar granule neurons are located.

The neuronal circuit of the cerebellum is repeated some 30 million times over, with little variation. The output from this functional unit is to a deep nuclear cell, which is constantly under excitatory and inhibitory influence. The excitatory influences are created by direct connections with afferent (carrying nerve impulses *to* the CNS) fibers, while the primary inhibitory influence to the deep nuclear cell are from Purkinje cells in the cerebellar cortex (Hall and Guyton, 2010).

There are two types of afferent fibers in the cerebellar cortex, the climbing fibers, and mossy fibers. One climbing fiber makes many synaptic contacts with the dendritic tree of one Purkinje cell, having a powerfully excitatory effect. The Purkinje cells' axons, as the only cortical output, lead out of the cortex to synapse with cerebellar nuclei. These cells are driven by a direct input, the climbing fibers, and an indirect, the mossy fibers via parallel fibers (Marr, 1969).

Mossy fibers refers to all other fibers entering the cerebellum from several different places – they come from the higher brain, the brain stem, and the spinal cord (Hall and Guyton, 2010). Here the term refers only to the mossy fibers of the cerebellum, not to be confused with hippocampal mossy fibers. Mossy fibers excite the deep nuclear cells and from there extend to the granule layer of the cerebellar cortex, where they synapse with cerebellar granule cells in the cerebellar glomeruli. In every glomerulus, there is one mossy fiber terminal, termed a rosette, and dendritic claws from multiple granule cells. The glomerulus is thus able to diverge, since every mossy fiber has multiple rosettes. Therefore, the mossy fibers end up synapsing with hundreds to thousands of granule cells. There, the granule cell axons become parallel nerve fibers, and synapse with Purkinje cells (Marr, 1969). Millions of parallel nerve fibers exist, making about 500 – 1000 granule cells for each Purkinje cell. The dendrites of the Purkinje cells from here extend into the molecular layer of the cerebellar cortex, where these synapses occur (Hall and Guyton, 2010).

Cerebellar granule cells make up the most numerous neurons in the brain, averaging about 50 billion per person, which is about three-fourths of the total neurons in the entire brain. All inputs are received from the mossy fibers, and each granule cell receives input from 3 – 5 mossy fibers. It is postulated that the reason for this is that the granule cell will not activate and initiate an action potential from a single source, but does so when receiving multiple inputs. This would allow for precise distinctions between input patterns and thus participate in the fine motor coordination that the cerebellum allows for the body. Within the cerebellum, in the deepest layer of the trilaminar cerebellar cortex, over 90% of the neurons are granule neurons. Neurogenesis of granule neurons occurs postnatally. The

development of the granule neurons consists of their proliferation in the external granular layer, then a downward migration, and then phenotypical and connectional differentiation (Marr, 1969).

The specific localization of proteins such as HVRP1 is likely to be related to their function, as the localization of the types of cells within the cerebellum determine input and output signals, and certain functions according to this circuitry. We now show in this work that HVRP1 does have a very specific localization, and that this may provide clues as to the function of HVRP1.

4.2 Materials and Methods

All animal procedures were carried out in accordance with the guidelines of the Institutional Animal Care and Use Committees at the University of California, Irvine.

DNA constructs for HVRP1 and Hv1-HVRP1 chimeras

Complementary DNA (cDNA) for human HVRP1/*C15ORF27* was custom synthesized by Epoch Biolabs. Mouse HVRP1/*AI118078* was cloned from mouse cerebellum cDNA (Zyagen). HVRP1 cDNAs were inserted in pGEMHE and pNICE vectors (Liman et al., 1992; Scheiffele et al., 2000), with or without C-terminal eGFP tag. In the resulting fluorescent constructs, HVRP1 and eGFP are connected by the flexible linker: SRGTSGGSGGSRGSGGSGG. Single point mutations were introduced with standard PCR techniques. Chimeras between

human Hv1 (IMAGE clone 5577070, Open Biosystems) and human HVRP1 were generated using the SOEing method (Horton et al., 1990). Constructs were verified by full sequencing. In the $Hv1NC_{HVRP1}$ chimera, residues 97-233 of HVRP1 were replaced by residues 98-230 of Hv1. In the $HVRP1NC_{Hv1}$ chimera, residues 103-218 of Hv1 were replaced by residues 102-221 of HVRP1. The generation of chimera $Hv1NC_{CiVSP}$ was previously described (Tombola et al., 2008).

Expression of recombinant HVRP1

For expression in oocytes, plasmids were linearized with NheI or SphI restriction enzymes (New England Biolabs) before *in vitro* transcription. RNA synthesis was carried out with a T7 mMessage mMachine transcription kit (Ambion). The correct sizes of the transcripts were confirmed by gel electrophoresis. mRNAs were injected in *Xenopus* oocytes (Ecocyte Bioscience) 1-3 days before the electrophysiological measurements (50 nl per cell, 0.3-1.5 µg/µl). Cells were maintained at 18°C in medium (ND96) containing 96 mM NaCl, 2 mM KCl, 1.8 mM $CaCl_2$, 1 mM $MgCl_2$, 10 mM HEPES, 5 mM pyruvate, 100 mg/L gentamycin, pH 7.2. HEK293A cells were cultured in DMEM (Life Technologies), supplemented with 10% fetal bovine serum (Gemini Bio-Products) and 1% Penstrep, at 37°C, under 5% CO_2. Cells were transfected with pNICE constructs using Lipofectamine 2000 (Life Technologies).

Culture of cerebellar granule neurons

Cerebellar granule cells were prepared from 7-day-old post-natal C57BL/6 mice (Charles River) as previously described (Lee et al., 2009). Cells were cultured in Neurobasal A media supplemented with GlutaMAX (Life Technologies), penicillin, 250 μM KCl, and 2% B-27 (Life Technologies). To prevent the growth of non-neuronal cells, 10 μM of cytosine-β-D-arabinofuranoside was added 24 hours after the initial plating and with each subsequent media change. Cells were plated onto poly-D-lysine-treated 6-well plastic plates for Western blotting and onto poly-D-lysine coated coverslips for immunohistochemistry.

Microarray analysis

The body index of gene expression (BIGE) database was developed as previously described (Hevezi et al., 2009; Roth et al., 2006). This database was generated using total RNA from 4 male and 4 female human donors. The genome-wide gene expression data was obtained with Affymetrix Human Genome U133 Plus 2.0 gene arrays. Analysis of microarray data for genes *C15Orf27*/HVRP1, *HVCN1*, and *TPTE*, was performed with ArrayAssist software (Stratagene) and OriginPro 8.1 (Origin Lab).

Quantitative real-time PCR

Total RNA from human donors (Ambion & Clontech) was used to synthesize complementary DNA (cDNA) with a QuantiTect® Reverse Transcription kit (Qiagen). The

cDNA was then assayed with a Roche LightCycler 480 Real-Time PCR system, using the following HVRP1/*C15Orf27* primers: AGGGTGAAGAGGGTCATTGAT, and TCGTACTGCTGGATAACCATCTC. Data was collected using the LightCycler 480 software and analyzed by comparative C_T method using β-actin to normalize C_T values.

Dendrogram

Genome databases were accessed at National Center for Biotechnology Information (NCBI) (http://www.ncbi.nlm.nih.gov/). The sequence of human HVRP1 was initially identified using the sequence of the voltage-sensing domain and C-terminus of human Hv1 as a search query on the BLASTP platform. To identify HVRP1 orthologs, the amino acid sequence of the human HVRP1 protein was used as a search query, using the default parameters of the BLASTP platform. Analysis of the resulting sequence data was performed with the Clustal program (Clustal Omega) (http://www.clustal.org/). Species abbreviations used can be found in Figure 4.1. The following proteins with NCBI and GenBank reference sequence numbers were used: ApHv1, XP_005028277.1; ApHVRP1, XP_005027974.1; ApTPTE2-like, XP_005014905.1; BtHv1, NP_001193182.1; BtHVRP1, XP_005222027.1; BtTPTE2-like, XP_005213782.1; CiHv1, NP_001071937.1; CiHVRP1, XP_002131775.1; CiVSP, NP_001028998.1; DrHv1, NP_001002346.1; DrHVRP1, NP_001074141.1; DrVSP, BAG50379.1; GgHv1, NP_001025834.1; GgHVRP1, XP_001233623.3; GgTPTE2, XP_417079.2; HsHv1, NP_001035196.1; HsHVRP1, NP_689548.2; HsTPTEα, NP_954870.2; HsTPTE2α, NP_570141.3; MbHv1, EPQ13961.1; MbHVRP1, XP_005874505.1; MbTPTE2-like, XP_005877021.1; MdHv1, XP_001372655.2; MdHVRP1, XP_001376486.2; MdPTEN-

like, XP_001363283.1; MoHv1, XP_003738360.1; MoTPTE2-like, XP_003745380.1; OaHv1, XP_001505975.2; OaTPTE2-like, XP_001513133.2; OhHv1, ETE71598.1; OhHVRP1, ETE66651.1; OhTPTE2, ETE70810.1; OoHv1, XP_004276784.1; OoHVRP1, XP_004276399.1; OoTPTE2-like, XP_004274689.1; PsHv1, XP_006132641.1; PsHVRP1, XP_006126300.1; PsTPTE2-like, XP_006124968.1; SpHv1, NP_001119779.1; SpHVRP1, XP_003724918.1; SpTPTE2-like. XP_003731108.1; TtHv1, XP_004310881.1; TtHVRP1, XP_004319937.1; TtTPTE2-like, XP_004323024.1; XtHv1, NP_001011262.1; XtHVRP1, XP_004916038.1; XtPTEN2like, NP_001015951.1.

In situ hybridization

Mouse HVRP1 cDNA fragments of 700 bp were inserted with opposite orientations in a pGEM vector between the T7 promoter and SphI restriction site using the SOEing technique and Phusion High-Fidelity polymeare (New England Biolabs). Sense and antisense digoxigenin-labeled RNA probes were prepared from SphI-linearized plasmids using the DIG RNA labeling mix from Roche. RNA probes were then cleaned and concentrated using a kit from Zymo Research. The cDNA sequence for the sense probe included the region starting with 5'-GAGCTTCTCATAGATA– and endding in –GAACCAGCAGTATGTG-3'. The corresponding reverse complement sequence was used as cDNA for the antisense probe. Adult C57BL/6 (Charles River) mice were deeply anesthetized with Nembutal and transcardially perfused with fixative (4% paraformaldehyde (PFA), 0.05% glutaraldehyde, and 0.2% picric acid dissolved in 0.1 M phosphate buffer, pH = 7.4) and saline. Brains were surgically removed following sacrifice,

fixed overnight, washed with PBS and treated with 30% sucrose overnight. Then, they were embedded in OCT compound (Tissue-Tek) in plastic molds (Ted Pella) and frozen. Sagittal cryosections of 10 – 14 μm thickness were prepared using a Leica 3050S cryostat. Individual sections were collected and floated into sterile PBS during the cryosectioning process and mounted onto SuperFrost Plus slides (Fisher) using the free-floating method. Sections were positioned onto the slides with a fine paintbrush. They were allowed to air dry and adhere to the slides, and then used immediately. The procedure for the *in situ* hybridization was adapted from ref. (Thisse and Thisse, 2008). The hybridization step and subsequent washing steps were performed in an Easy Dip Slide Staining System (Ted Pella). Samples were incubated with anti-digoxigenin antibody conjugated to alkaline phosphatase (Roche). The HVRP1 transcript was visualized by detection of digoxigenin by incubating samples overnight in a staining solution of Nitro blue tetrazolium (NBT) and 5-Bromo-4-chloro-3-indolyl phosphate (BCIP) solution (Roche). The staining reaction was stopped with 4% PFA. Sections were mounted with 70% glycerol under glass coverslips. Digital images were captured using DP Controller software (Olympus) connected to an upright Olympus SZX12 microscope.

HVRP1 antibody

Two rabbits were immunized against the mouse HVRP1 C-terminal peptide EEKFRSLESKEPKLHTVPEA by Open Biosystems. Antisera were tested on Western blots against the recombinant HVRP1 expressed in oocytes and in immunohistochemistry of rat cerebellar tissue. The antiserum with the smallest background in both assays was purified

by affinity chromatography (Open Biosystems) and used thereafter at dilutions 1:500 or 1:1000.

Confocal imaging

HEK293A cells transfected with hHVRP1-eGFP in pNICE were grown on poly-D-lysine coated glass-bottom dishes (Mattek) for 1 to 2 days. Directly before imaging, live cells were washed in cold HBSS (Life Technologies) to remove residual FBS, and bathed in fresh HBSS. FM 4-64 dye (Life Technologies) was added to the solution (5 μM final concentration) to label the plasma membrane. Cells were imaged on a Zeiss LSM 780 confocal microscope with an LD C-Apochromat 63x immersion objective with 1.15 numeric aperture. For eGFP, excitation was at 488 nm, and emission band was 491 – 560 nm. For FM 4-64, excitation was at 561 nm, and emission band was 592 – 759. Primary cerebellar granule neurons growing on poly-D-lysine coated coverslips were fixated in 1:1 methanol and acetone solution for ten minutes at -20° C. Immunocytochemistry was performed using either anti-HVRP1 antibody diluted 1:1000, or anti-HVRP1 antibody diluted 1:500 pre-incubated with peptide antigen (1:500 dilution of a 1 μg/μl solution), and AlexaFluor-594-labeled goat anti-rabbit secondary antibody. Coverslips were then mounted onto Fisher SuperFrost Plus slides with ProLong Gold Antifade Reagent with DAPI (Life Technologies). For AlexaFluor 594, excitation was at 561 nm, and emission band was 592 – 759 nm. For DAPI, excitation was at 405 nm and emission band was 415 – 735 nm.

Immunohistochemistry and electron microscopy

Adult Wistar rats were deeply anesthetized with ketamine-xilazine and transcardially perfused with ice cold saline for 1 minute then with fixative containing 4% paraformaldehyde 0.1% glutaraldehyde and 30% saturated picric acid dissolved in 0.1 M phosphate-buffer (PB). After overnight post fixation in the same fixative, brains were cut into 60 μm sections with a vibratome (Leica). Sections were treated with 0.1% sodium borohydrate in 0.1 M PB for 10 minutes, then extensively washed for 30 minutes in 0.1 M PB. Sections were thereafter incubated in 10% normal goat serum (NGS, Vector Labs), and then in 2% NGS and 1:500 rabbit anti-hHVRP1 antibody for 48 hours at 4 °C. After several washes in buffer, the sections were incubated in 0.8 nm gold-conjugated goat anti-rabbit dissolved in 0.1 M PB containing 0.1% cold-water fish skin gelatin (Aurion) and 1% bovine serum albumin (Sigma-Aldrich) overnight at room temperature. The gold particles were increased in size with R-Gent silver enhancement kit (Aurion). The sections were thereafter treated with 1% OsO_4 for 30 minutes, then contrasted with 1% uranil acetate, dehydrated and embedded in Durcupan (Sigma-Aldrich). Ultrathin sections (60 nm) were imaged with a Philips transmission electron microscope and pictures were taken with a Gatan camera.

Electrophysiology and voltage-clamp fluorometry

Two-electrode voltage clamp and voltage-clamp fluorometry measurements were performed on *Xenopus* oocytes 1 - 3 days post-injection as previously described (Tombola et al., 2010). Bath solution contained either 100 mM NaCl, 3 mM $CaCl_2$, 2.5 mM KCl, 5mM

HEPES, pH = 7.4, or 55 mM sodium methanesulfonate, 55 mM sodium acetate, 10 mM MES, 2 mM $MgCl_2$, pH = 6.3. For VCF recordings, native cysteines were blocked by incubating oocytes in glycine-maleimide (Toronto Research Chemicals) dissolved in ND96 for 30 minutes at room temperature 1 – 2 hours post-injection. Oocytes were labeled with 2-((5(6)-Tetramethyl-rhodamine)carboxylamino)ethyl Methanethiosulfonate (TAMRA-MTS) (Toronto Research Chemicals) in the dark for 1 minute at room temperature on the day of recording, and all labeled oocytes were stored at 10° C until use. An Oocyte Clamp OC-725C (Warner Instruments) was used to measure currents and control the membrane potential. A Dagan PhotoMax 200 coupled to a PIN photodiode was used to measure fluorescence signals. A CoolLED pE-2 excitation system (550 nm) connected to an Olympus IX71 microscope was used to excite the fluorophore. The oocyte membrane was visualized through a 20X Olympus UPlansApo objective and an Olympus TRITC filter cube. The amplifiers for current and fluorescence signals were interfaced to a PC through a 1440A Digidata analog/digital converter (Molecular Devices). Traces were filtered at 1 KHz and acquired at 5 KHz. Data were then analyzed with Clampfit 10.2 (Molecular Devices) and Origin 9 software (Origin Lab). Patch-clamp recordings were performed on excised inside-out patches from oocytes using an Axopatch 200B amplifier (Molecular Devices) as described in (Hong et al., 2013; Yu and Catterall, 2004). Both bath and pipette solutions contained 100 mM 2-(N-morpholino)ethanesulphonic acid (MES), 30 mM tetraethylammonium (TEA) methanesulfonate, 5 mM TEA chloride, 5 mM ethyleneglycol-bis(2-aminoethyl)-N,N,N',N'-tetra-acetic acid (EGTA), adjusted to pH 6.0 with TEA hydroxide. Measurements were performed at 22 ± 2 °C with pipettes of 2–4 MΩ access

resistance. Traces were filtered at 1 KHz and acquired at 5 KHz. They were then analyzed with Clampfit 10.2 (Molecular Devices) and Origin 9 (Origin Lab).

Western blotting

Total protein from transfected and non-transfected HEK293A cells was collected with lysis buffer (50 mM Tris-HCl, pH 7.5, 5 mM EDTA, 150 mM NaCl, 1% Triton-X 100, and protease inhibitor cocktail [Sigma]). The cell lysates were centrifuged at 13,000 rpm for 10 minutes at 4°C. Proteins from supernatants were separated by SDS-PAGE (4 – 20%, Tris-Glycine, Life Technologies). After gel electrophoresis, proteins were transferred to polyvinylidene difluoride (PVDF) membranes (Milllipore). The membranes were incubated with anti-HVRP1 antibody at a 1:1000 dilution, or anti-HVRP1 antibody neutralized by antigen peptide (1:1000 dilution of a 1 μg/μl solution). Mouse anti-rabbit secondary antibody was conjugated with horseradish peroxidase (Chemicon International) and used at a 1:50,000 dilution. The membranes were stripped by washing with a mild stripping buffer (1.5% glycine, 0.1% SDS, 0.5% Tween-20, pH 2.2) for 2 x 10 minutes, then PBS 2 x 10 minutes, and TBST 2 x 10 minutes. Membranes were then re-probed with anti-β-actin antibody conjugated to HRP (Abcam) at a 1:5000 dilution. All proteins interacting with primary antibodies were visualized with Super Signal West Pico chemiluminescent substrate (Thermo Fisher).

4.3 Results

To identify proteins similar to Hv1, we performed a search with BLASTP (Altschul et al., 1997; Ashcroft, 1999), using the sequence of the VSD and C-terminus of the human Hv1 protein as query. We then reduced the number of hits by imposing that the protein: 1) should be made of four transmembrane segments, 2) should possess a coiled-coil domain in the cytoplasmic region, and 3) should not be yet characterized. The predicted protein from the human gene *C15ORF27* was found to be a promising candidate (identity: 26%, coverage: 99%) in agreement with an earlier report in which the sequence similarity between HVRP1 and Hv1 was determined using a distinct approach (Murata et al., 2005; Musset et al., 2011).

The hydrophobicity plot of C15orf27/HVRP1 indicates that the protein lacks the S5 and S6 transmembrane segments typical of Na_V, K_V, and Ca_V channels (Fig. 4.1C). In Hv1, the cytoplasmic C-terminus is rather short (~50 a. a.) and it is composed solely of a coiled-coil domain starting right after the fourth transmembrane segment. In HVRP1, the C-terminus is as large as in CiVSP (~300 a. a.), and it contains a predicted coiled-coil domain similar in length and position to the coiled-coiled domain of Hv1 (Fig. 4.S1.).

Overall, HVRP1 is more tightly related to Hv1 than to other VSD-containing proteins (Fig. 4.1B) and it is highly conserved in vertebrates (e.g., human and zebrafish HVRP1 sequences are 60% identical). The evolutionary relationship between different VSD-containing proteins has been recently investigated (Kohout et al., 2010; Kulleperuma et al., 2013;

Murata et al., 2005; Smith et al., 2011), and Hv1 and C15orf27/HVRP1 were found to be more closely related to Na_V channels than to other voltage-gated ion channels. The arginine-repeat motif in S4, responsible for voltage sensing, is highly conserved between Hv1 and HVRP1, as are negatively charged residues in S2 and S3 known to form salt bridges with the S4 arginines (Fig. 4.1D). The Hv1 aspartate residue in S1 involved in the cooperative gating of the channel's two subunits (Li et al., 2014; Qiu et al., 2013) is conserved in HVRP1, and so is the S2 histidine that contributes to binding zinc in Hv1 (Ramsey et al., 2006; Suh et al., 2010; Takeshita et al., 2014; Yudin et al., 2011) (Fig. 4.1D). The VSDs of voltage-gated ion channels and voltage-sensitive phosphatases contain a signature phenylalanine in the middle of S2 known to play a key role in voltage sensing as charge transfer center (Lacroix and Bezanilla, 2011; Tao et al., 2010; Tapparel et al., 2003; Walker et al., 2001; Wu et al., 2001). The phenylalanine appears to be highly conserved also in HVRP1 proteins (Fig. 4.1D).

4.3.1 HVRP1 tissue distribution

The sequence similarity and the presence of a coiled-coil domain in both Hv1 and HVRP1 suggested that the two proteins could have similar physiological functions, or that they could work together as heteromultimers. A correlation in the tissue distribution between the two proteins would support this idea. So, we compared the tissue distribution of Hv1 and HVRP1 on a human genome-wide expression database produced using an Affymetrix genearray system that contained 54,675 probe sets per array, representing 21,974 unique Unigene clusters (i.e., more than 47,000 transcripts) (Hevezi et al., 2009; Roth et al., 2006;

Walker et al., 2001; Wu et al., 2001). This body index of gene expression (BIGE) database compares gene expression across 105 normal tissues representing all major systems of the human body. In agreement with previous reports (Neuhaus and Hollemann, 2009; Okamura, 2007; Ramsey et al., 2006; Ratzan et al., 2011; Wu et al., 2012), we found the highest levels of Hv1 transcript in the immune system and in the testis (Fig. 4.2A), and low expression in brain tissues. In contrast, we found HVRP1 primarily expressed in cerebellar tissues (Fig. 4.2A, Table 4.S1). We also examined the expression profile of the TPTE (human homolog of CiVSP) and found it very different from the expression profile of HVRP1. We confirmed that the HVRP1 transcript is mainly present in the cerebellum by qRT-PCR on total RNA extracts from human tissues (Fig. 4.2B). HVRP1 expression was detected also in cerebral cortex, skeletal muscle, and thyroid, but at much lower levels.

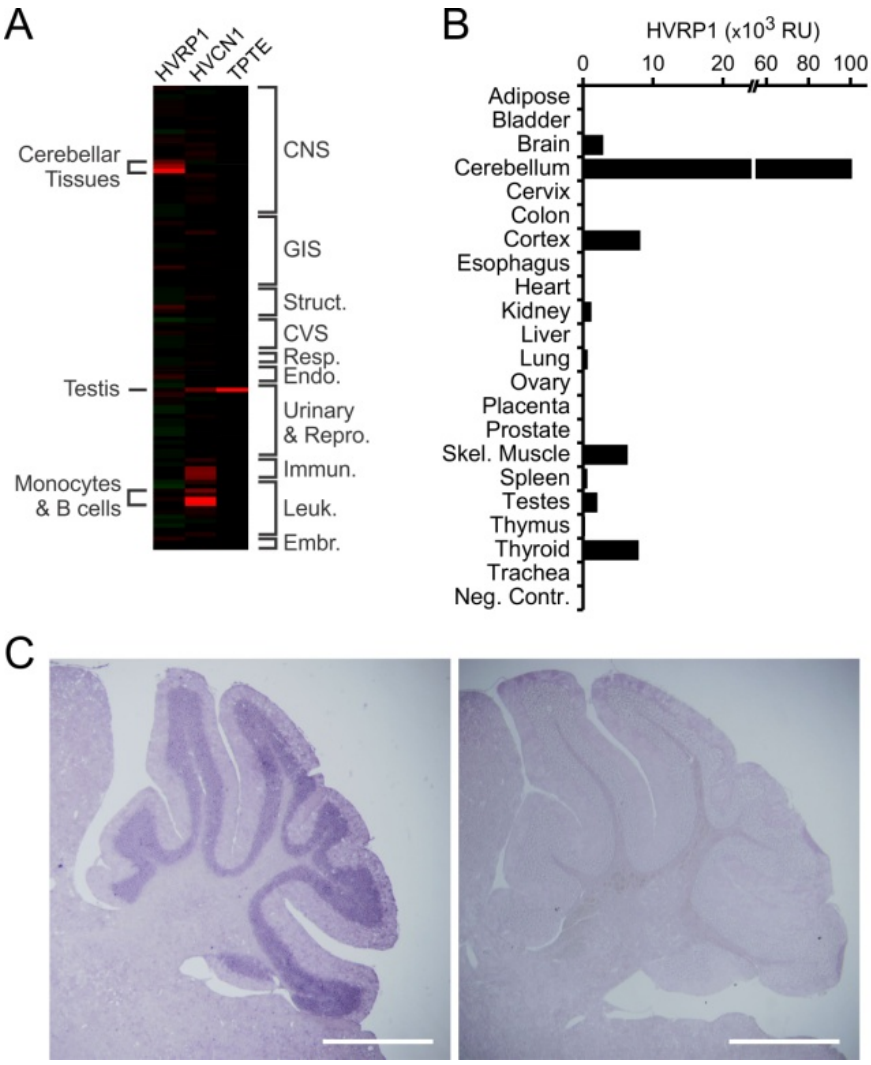

Figure 4.2. Tissue distribution of HVRP1 transcript. (A) HVRP1 expression in human tissues assessed by Affymetrix microarray analysis. HVRP1 tissue distribution was compared to the distributions of human Hv1 (HVCN1) and TPTE. Red and green signals indicate up-regulated and down-regulated expression, respectively. Struct.: skeletal muscle, adipose tissue, skin. CVS: heart and blood vessels. Resp.: respiratory system. Endo.: endocrine organs. Urinary & Repro.: urinary & reproductive systems (male and female). Immun.: immune tissues. Leuk.: peripheral white blood cells. Embr.: embryonic tissues (see also Table S1). **(B)** Levels of HVRP1 transcript in total RNA extracts from the indicated human tissues measured by RT-PCR. Levels are reported as relative expression units (RU) in relation to the housekeeping control gene beta-actin. Water was used as negative control. Error bars are S.E.M., n = 3. **(C)** *In situ* hybridization on a 20-µm thick sagittal section of an adult mouse brain cerebellar region, using a 600-bp riboprobe targeting the HVRP1 mRNA. Positively stained regions are dark purple. Left panel: antisense probe. Right panel: control sense probe. Scale bars: 1 mm.

4.3.2 HVRP1 cellular and subcellular localization

The cerebellum is made of well-characterized types of neurons and glial cells. To identify cerebellar cells expressing HVRP1, we performed *in situ* hybridizations on fixed cryosections of adult mouse brains. We detected high levels of HVRP1 mRNA in the cerebellar granule layer (Fig. 4.2C). We then investigated the cellular and subcellular localization of the HVRP1 protein by immunohistochemistry (IHC) and immunogold electron microscopy (EM) on fixed cryosections of adult rat brain, using a custom-made antibody raised against a C-terminal peptide of the mouse protein, which also recognizes human and rat HVRP1 (Fig 4.3A – C). We found that the protein is present in the dendrites and soma of cerebellar granule neurons, but not in their axon (parallel fibers were not stained, Fig. 4.3). The immunogold EM analysis revealed the presence of HVRP1 within glomerular structures, on the postsynaptic side of the contacts between glutamatergic mossy fibers and granule cells (Fig. 4.3C – D).

The immunostaining of native HVRP1 indicated that the protein resides on the plasma membrane. We confirmed this finding by expressing recombinant HVRP1 in HEK293A cells and establishing its co-localization with the plasma membrane marker FM-4-64 (Fig. 4.3G). We detected the presence of the HVRP1 protein also in cultured granule neurons from P5 – P6 neonatal mice assayed by immunocytochemistry (Fig. 4.3E – F). Western blots of HEK293A cells expressing human HVRP1 showed a band a 64 KDa (Fig. 4.3H). Preincubation of the primary antibody with the peptide antigen prevented protein recognition.

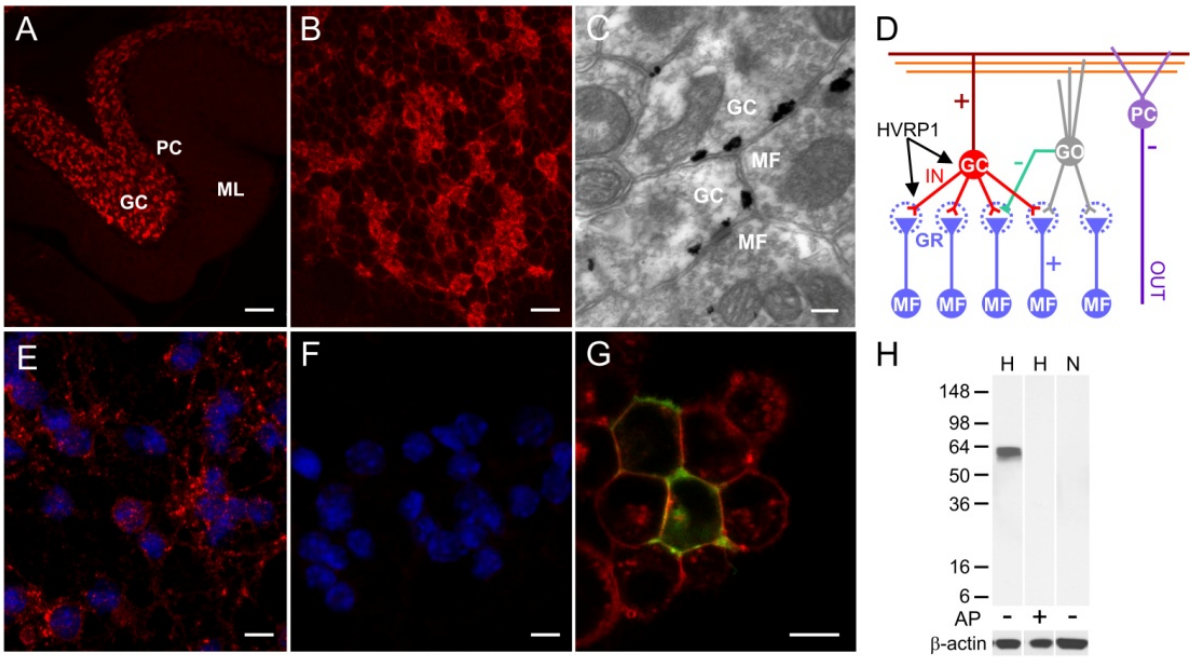

Figure 4.3. Cellular and subcellular localization of the HVRP1 protein. **(A)** Immunohistochemical analysis of HVRP1 distribution in cerebellar tissue. Cerebellar cortical section from a wild-type rat stained with polyclonal antibody raised against HVRP1 (red). GC: granule cell layer, PC: Purkinje cell layer, ML: molecular layer, scale bar: 50 μm. **(B)** Higher magnification of granule neurons expressing HVRP1, from (A). Scale bar is 10 μm. **(C)** Ultrastructural localization of HVRP1 in the rat cerebellar GC layer visualized with the pre-embedding immunogold method. Positive labeling is in black, in the glomeruli, at the dendritic claws of granule cells surrounding mossy fiber terminals. Scale bar is 0.1 μm. **(D)** Basic circuit diagram of the cerebellar cortex showing the location of HVRP1 in the dendrites and cell bodies of GCs. GO: Golgi cell, GR: glomerulus, MF: mossy fiber, PC: Purkinje cell. **(E)** Confocal images of cultured mouse cerebellar granule neurons fixed and immunostained at 8 DIV. HVRP1 signal is shown in red (antibody dilution 1:1000), DAPI signal is in blue. **F**) Staining as in (E) but with anti-HVRP1 antibody at dilution 1:500 pre-incubated with HVRP1 antigen peptide (see Methods). Scale bars are 10 μm. **(G)** Confocal image of live HEK293A cells expressing recombinant EGFP-tagged human HVRP1 (green) and labeled with the plasma membrane marker FM-464 (red). Scale bar is 10 μm. **(H)** Western blot of total protein extracts from HEK293A cells transfected with hHVRP1 (H) and non-transfected (N). AP indicates pre-incubation of anti-HVRP1 antibody with antigen peptide.

4.3.3 Differences in functional properties between Hv1 and HVRP1

To learn more about the relationship between Hv1 and HVRP1, we compared the functional properties of the two proteins expressed in *Xenopus* oocytes, and then examined chimeric proteins in which parts of HVRP1 were swapped with the corresponding parts of Hv1 (Fig. 4.4A).

We measured large voltage-dependent proton currents from oocytes expressing the human Hv1 protein using two-electrode voltage-clamp (TEVC) (Fig 4.4B – C). Under the same conditions, we could not detect any current from human HVRP1 (Fig. 4.4B-C), confirming a previous report in which a similar construct was expressed in HEK293 and COS-7 cells (Musset et al., 2011; Ramsey et al., 2006; Sasaki et al., 2006). To enhance the proton current, the intracellular pH of the oocytes was lowered to pH 6.1 with 55 mM sodium acetate at pH 6.3 in the extracellular solution, as previously described (Choe et al., 1997; Koch et al., 2008; Lee et al., 2008; Tombola et al., 2008; 2010). However, this did not have any measureable effect on HVRP1-expressing cells.

The lack of current from HVRP1 was not due to mislocalization of the protein in the oocyte. We labeled oocytes expressing an HVRP1 mutant with a substituted cysteine close to the extracellular end of S4 (F196C) with the thiol-reactive environment-sensitive dye TMRA-MTS (Fujiwara et al., 2012; Li et al., 2010; Tombola et al., 2010). From these oocytes, we were able to measure fluorescence changes in response to membrane depolarization using voltage-clamp fluorometry (Fig. 4.4D, central panel, black trace), indicating that the protein was on the plasma membrane. The magnitude of the fluorescence changes was similar to that observed with Hv1 labeled at the extracellular end of S4 (Fig. 4.4D, left panel, black trace). Oocytes expressing HVRP1 or Hv1 lacking cysteine substitutions did not show fluorescent changes (Fig. 4.4D, gray traces). In labeled Hv1, membrane depolarization causes a fast increase in fluorescence followed by a slower but more pronounced decrease. In labeled HVRP1 only the fast increase in fluorescence is observed upon depolarization

(Fig. 4.4D central panel), suggesting that the environment around the fluorophore changes in different ways in the two proteins as a result of voltage change.

The fact that HVRP1 does not conduct current under voltage-clamp conditions could be due to the lack of a functioning conduction pathway in the VSD or to the failure in properly activating the protein under the experimental conditions used. While membrane depolarization is sufficient to open the activation gate of the Hv1 channel, some other stimuli might be required to activate HVRP1. We explored the possibility that the N- or the C-terminus of HVRP1 may be responsible for preventing the opening of the VSD gate in the absence of proper stimulation (e.g., binding to other proteins missing in the reconstituted system, incorrect post-translational modifications, etc.). When we exchanged the N- and C-termini of Hv1 with those of HVRP1 ($Hv1NC_{HVRP1}$ chimera), we obtained functional channels for which we measured the conductance versus voltage relationship (G-V). We found that the G-V was shifted to less positive potentials compared to Hv1 wild type (Fig. 4.4E), indicating that VSD activation is facilitated in $Hv1NC_{HVRP1}$. On the other hand, we could not measure any voltage-dependent current from the chimera in which the N- and C-termini of HVRP1 were replaced by the corresponding parts of Hv1 ($HVRP1NC_{Hv1}$) (Fig. 4.4B-C). The substitution of cytoplasmic domains of Hv1 with the corresponding parts of CiVSP ($Hv1NC_{CiVSP}$ chimera) is known to produce a G-V shift to more positive potentials and to strongly accelerate VSD deactivation compared to Hv1 wild type (Gonzalez et al., 2010; Musset et al., 2010; Tombola et al., 2008; 2010). We found that in $Hv1NC_{HVRP1}$, deactivation was not as accelerated as in $Hv1NC_{CiVSP}$ (Fig. 4.4F). The smaller perturbation of VSD gating produced by the N- and C-termini of HVRP1 compared to CiVSP could be due to the fact

that HVRP1 contains a coiled-coil domain similar to Hv1 (Decoursey, 2013; Fujiwara et al., 2012).

In Hv1, aspartate D112 (located in the middle of the first transmembrane segment) has been proposed to be the channel's selectivity filter (Musset et al., 2011; Okochi et al., 2009; Wu et al., 2012). Its substitution to a valine (the residue at the homologous position in HVRP1) was found to strongly reduce conduction and selectivity for protons (Musset et al., 2011; Wu et al., 2012). We wondered whether the inverse substitution (V to D) in HVRP1 could confer proton permeability to its VSD. We generated HVRP1 and HVRP1-NC_{Hv1} constructs containing the V111D mutation (identified as $HVRP1^{V/D}$ and $HVRP1^{V/D}NC_{Hv1}$, respectively) expressed them in *Xenopus* oocytes, and tested their conduction properties in two-electrode voltage clamp. We found that the constructs did not produce detectable currents under conditions in which Hv1 WT and $Hv1NC_{HVRP1}$ were highly conducting (Fig. 4.4C shows the example of $HVRP1^{V/D}NC_{Hv1}$). Voltage-clamp fluorometry measurements performed on the labeled V111D mutants indicated that the proteins were targeted to the plasma membrane, albeit less effectively than the constructs lacking the V111D mutation (Fig. 4.4D).

Taken together, these findings indicate that: 1) the N- and C-termini of HVRP1 are compatible with VSD proton conduction. 2) The VSD of HVRP1 lacks a functional proton permeation pathway, despite the sequence similarity to Hv1. 3) Structural differences between the VSDs of Hv1 and HVRP1 prevent proton conduction in HVRP1 even in the presence of the S1 aspartate that forms the selectivity filter in Hv1.

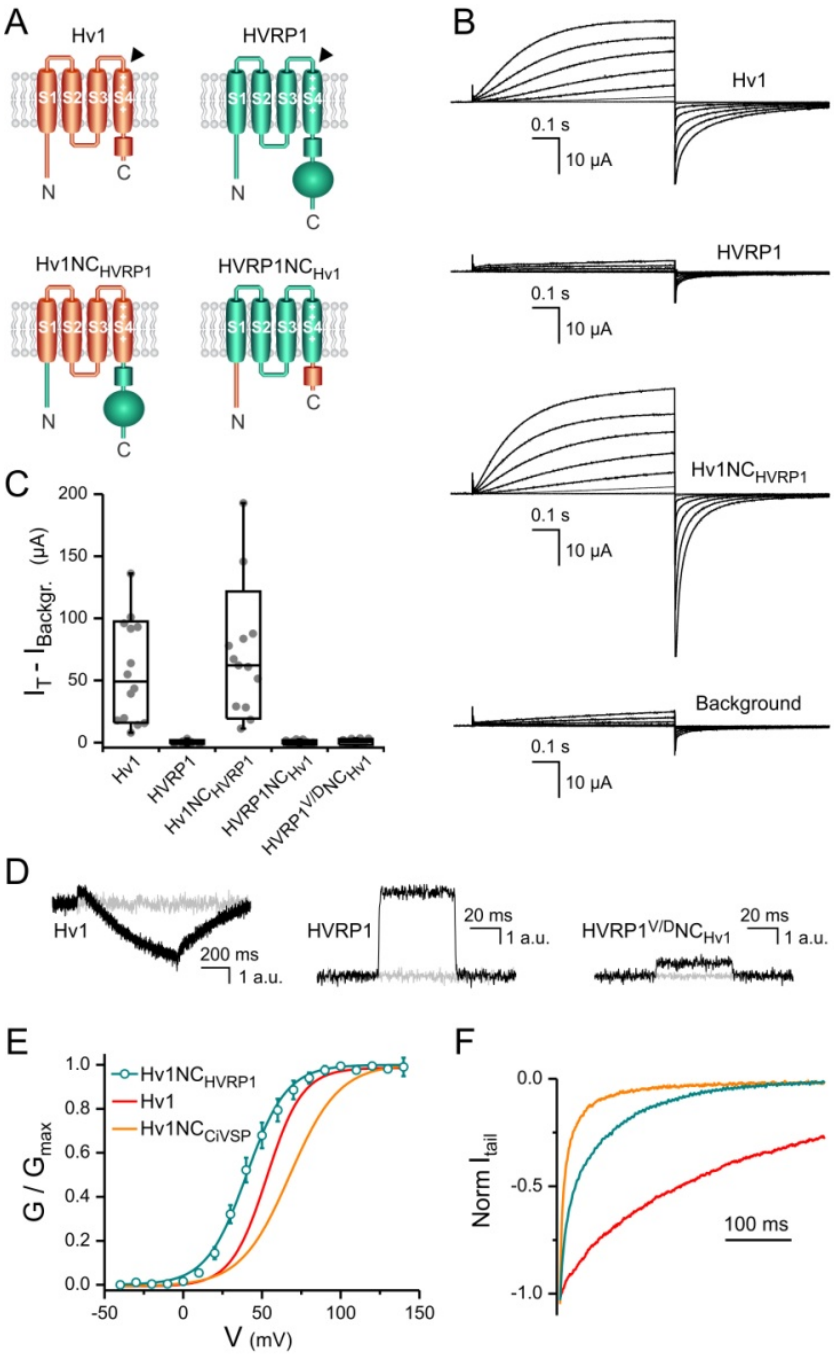

Figure 4.4. Comparison between the VSD conducting properties of Hv1 and HVRP1. (A) Schematics of constructs used for the comparison (B-C). Black arrowheads indicate positions of the cysteine substitutions for fluorophore attachment (D). **(B)** Proton currents from the indicated proteins expressed in a *Xenopus* oocyte measured in response to membrane depolarization by two-electrode voltage clamp. The test voltage was increased from 0 to +140 mV in 20 mV steps. Holding potential was -80 mV. Currents measured with HVRP1 are indistinguishable from the background. **(C)** Quantification of test currents measured at +120 mV from traces like those shown in (B). Box indicates median ± S.D., whisker shows range. Individual measurements are shown as gray circles, n = 10 – 14. **(D)** Fluorescence changes (expressed in arbitrary units) from TMRA-MTS-labeled oocytes expressing the indicated proteins with or without cysteine substitution (shown in black and light gray, respectively). Substituted positions were: H193 in Hv1 and S196

in HVRP1. HVRP1$^{V/D}$ contained the additional mutation V111D. The membrane was depolarized to +120 mV from a potential of -100 mV. **(E)** G-V relationship for the Hv1NC$_{HVRP1}$ chimera compared to the G-V of Hv1 wild type and the Hv1NC$_{CiVSP}$ chimera. Error bars are S.E.M., n = 5. Normalized conductances were measured from tail currents recorded in inside-out patches from oocytes. Curved line for Hv1NC$_{HVRP1}$ represents a Boltzmann fit with parameters: $V_{1/2}$ = 40 ± 3 mV, and slope = 12.8 ± 1.1 mV. Curves for Hv1 and Hv1NC$_{CiVSP}$ represent previously published G-Vs with: $V_{1/2}$ 53 ± 3 mV, slope 11.6 ± 0.6 mV, and $V_{1/2}$ 68 ± 2 mV, slope: 15.0 ± 0.2 mV, respectively (Tombola et al., 2008). **(F)** Example of deactivation kinetics of Hv1NC$_{HVRP1}$ (teal) compared to Hv1 (red) and Hv1NC$_{CiVSP}$ (orange). Tail currents were measured in response to a voltage step from +140 mV to -80 mV and normalized to the maximal current.

4.4 Discussion

The nervous system relies on proteins that can detect changes in membrane potential to generate and modulate electrical signals (Hille, 2001; Thomas and Meech, 1982). Accordingly, most of these proteins are highly expressed in the brain (Okochi et al., 2009; Ramsey et al., 2009; Vacher et al., 2008; Wu et al., 2012), and mutations in their genes produce neurological disorders (Ashcroft, 1999; Cannon, 2006; Catterall et al., 2008; Schmahmann and Sherman, 1998). All the known VSD-containing proteins involved in neuronal signaling are ion channels containing a pore domain. The voltage sensitive phosphatases and voltage-gated proton channels cloned so far are expressed primarily in non-excitable cells, and do not appear to perform functions specific to the nervous system (Marr, 1969; Okamura, 2007; Okochi et al., 2009; Ramsey et al., 2009; Tapparel et al., 2003; Walker et al., 2001; Wu et al., 2012; 2001).

Here we have identified HVRP1, a VSD-containing protein lacking a pore domain primarily expressed in the central nervous system. From a human gene expression profiling and qRT-PCR screening, HVRP1 was found to be highly expressed in cerebellar tissues. *In situ* hybridization on mouse brain revealed the presence of HVRP1 transcripts in the granule

layer of the cerebellar cortex. Expression of the HVRP1 protein in cerebellar granule neurons in brain slices and cell culture was confirmed by IHC/ICC. Protein subcellular localization was then determined by immunogold electron microscopy. HVRP1 was detected at the dendritic claws of the granule cells surrounding glutamatergic mossy fiber terminals.

Since the protein most closely related to HVRP1 is Hv1, we tested whether the two proteins had similar channel activity. We found that, unlike Hv1, HVRP1 did not conduct ions when expressed in *Xenopus* oocytes. We then tested chimeras between HVRP1 and Hv1 to establish whether the different behavior of the two proteins was due to the transmembrane VSD or to the N- and C-terminal cytoplasmic domains. We found that while the chimera Hv1-NC_{HVRP1} operated as an ion channel, the inverse chimera HVRP1-NC_{Hv1} did not. This indicated that, even though the VSD is the part of HVRP1 with the highest homology to Hv1, it is also the part responsible for the difference in ion channel activity between the two proteins. On the other hand, the N- and C-terminal domains of HVRP1 appear to be compatible with VSD gating and ion permeation.

We also found that the inability of HVRP1 to conduct ions did not depend on the presence of an aspartate residue in the middle of helix S1, while the corresponding residue in Hv1 was previously shown to act as the channel's selectivity filter (Marr, 1969; Musset et al., 2011). This suggests that the functional divergence between the VSDs of Hv1 and HVRP1 is not simply the result of a localized occlusion of the permeation pathway in HVRP1, but rather of a broader structural difference between the two domains.

Cerebellar granule neurons have rather short dendrites ending in glomerular structures that receive both excitatory inputs from glutamatergic mossy fibers and inhibitory inputs from GABAergic Golgi cells (Fig. 4.3C). The presence of HVRP1 on the dendritic plasma membrane of granule cells, and in particular in compartments rich in glutamate receptors and their regulatory proteins, suggests a function for HVRP1 related to the modulation of postsynaptic potentials and/or back-propagating action potentials. The presence of a VSD and a coiled-coil domain in HVRP1 and the lack of ion channel activity raise the possibility that the protein's function is to provide voltage sensitivity to a distinct effector. The limited homology to known proteins of the HVRP1's cytoplasmic region attached to the coiled-coil domain suggests that HVRP1 could affect neuronal physiology in a way not previously described in other VSD-containing proteins.

4.5 Supporting Information

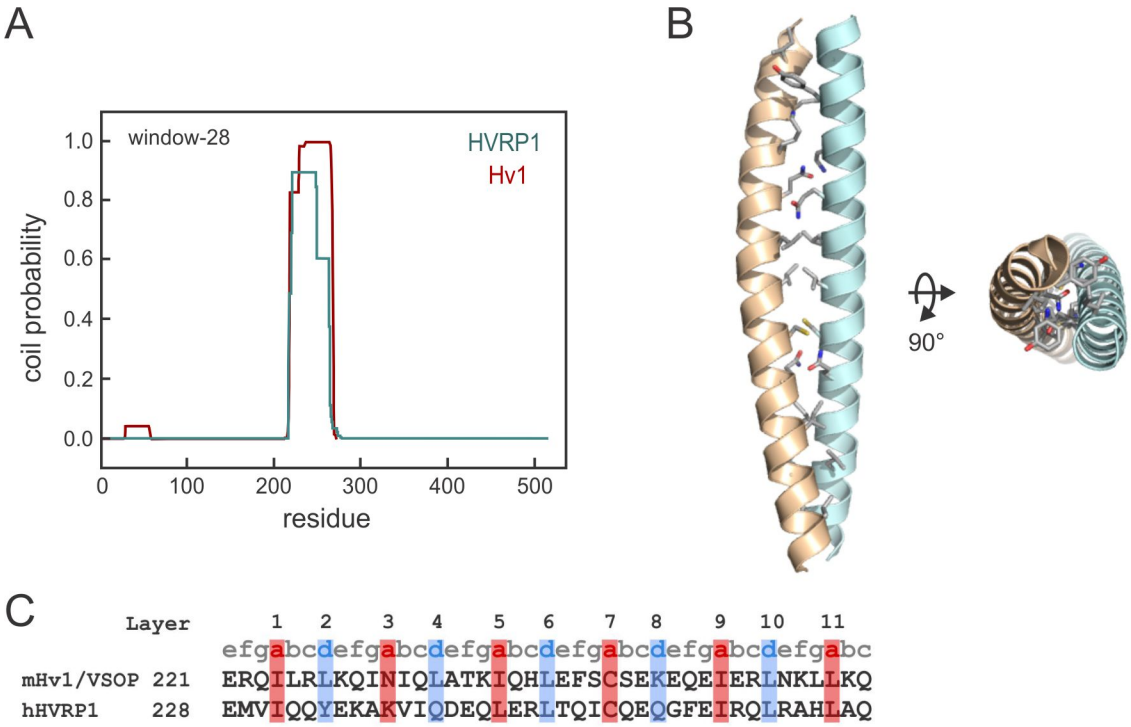

Figure S4.1. Predicted coiled-coil domain in HVRP1. (A) Human HVRP1 and Hv1 sequences were analyzed with the program Coils (Lupas et al., 1991) in ExPASy. The program predicts parallel two-stranded coiled-coil domains in the C-terminal regions right after the S4 transmembrane segments of the two proteins. The coiled-coil domain of Hv1 has been confirmed experimentally by X-ray crystallography (Fujiwara et al., 2012; Li et al., 2010). **(B)** Homology modeling by molecular dynamics simulations of the coiled-coil domains of HVRP1 and Hv1. **(C)** Sequence alignment of the coiled-coil domains of HVRP1 and Hv1.

Table S4.1. Tissue distribution of HVRP1

n	Tissue	HVRP1/ C15orf27*	HVCN1/ MGC15619*	TPTE/ PTEN2*
1	Cerebral cortex	0.1028	-0.0382	-5.12463E-4
2	Prefrontal cortex	0.00953	-0.06775	-4.03111E-4
3	Frontal cortex	-0.05867	-0.0395	-5.8629E-4
4	Frontal lobe	0.05989	-0.02112	-1.45221E-4
5	Parietal lobe	0.06119	-0.02778	1.33576E-4
6	Occipital lobe	0.06071	-0.02341	-4.90764E-4
7	Temporal lobe	0.06626	-0.02386	9.30587E-4
8	Corpus callosum	0.02011	0.04222	-1.61723E-4
9	Accumbens	7.1291E-4	-0.02121	-3.29741E-4
10	Putamen	-0.00473	-0.02332	7.3381E-10
11	Globus pallidus	-0.12441	0.07486	1.74259E-4
12	Amygdala	0.09238	-0.0361	2.56122E-5
13	Hippocampus	0.12182	-0.01772	-6.43837E-5
14	Ventral tegmental area	0.05941	0.0941	7.51509E-4
15	Thalamus	0.03427	0.04341	9.70315E-4
16	Subthalamic nuclei	-0.00603	0.10989	6.16615E-4
17	Hypothalamus	0.0701	0.0744	1.71761E-4
18	Cerebellar hemisphere	0.35123	-0.05444	0.00131
19	Cerebellar vermis	0.64944	-0.01868	6.09891E-4
20	**Cerebellum**	**1**	-0.04708	4.6069E-4
21	Substantia nigra	0.06297	0.12751	0.00119
22	Midbrain	-0.00517	0.05388	0.00145
23	Pons	0.04834	-0.0443	-7.71975E-4
24	Medulla	0.00348	0.03542	-1.54578E-4
25	Vestibular nuclei superior	0.01314	0.0348	9.15503E-4
26	Nodose nucleus	0.01364	0.07923	4.30438E-5
27	Spinal cord	-0.01218	0.06345	-2.85842E-4
28	Dorsal root ganglia	-0.07158	-0.0248	1.70288E-4
29	Trigeminal ganglia	-0.07643	-0.01194	-2.51115E-4
30	Oral mucosa	-0.06583	-0.04181	-0.00218
31	Pharyngeal mucosa	-0.04185	-0.0374	9.45631E-5
32	Tongue	0.11861	0.0034	-3.15883E-4
33	Tongue main corpus	0.01689	-0.03283	5.03468E-4
34	Tongue superior	0.01941	0.16346	-0.00123
35	Salivary gland	0.0181	-0.01487	4.24108E-4
36	Esophagus	-0.01711	-0.03642	-0.00121
37	Stomach	-0.05831	-0.00742	6.63115E-5
38	Stomach cardiac	0.06758	0.00902	7.95397E-4
39	Stomach fundus	-0.02056	-0.00491	-7.74737E-4
40	Stomach pyloric	-5.49618E-8	0	-2.74972E-4
41	Small intestine duodenum	-0.04671	0.03013	7.54349E-5
42	Small intestine jejunum	0.23393	0.02189	-1.5209E-4
43	Small intestine	-0.02717	-0.00448	5.867E-4
44	Colon cecum	-0.02503	0.02288	3.20271E-4
45	Colon	-0.03862	-0.03335	1.13957E-4
46	Liver	-0.02567	-0.03361	-6.39347E-5
47	Adipose	-0.06076	0.02187	-6.4118E-4
48	Adipose omental	-0.05082	0.02954	-2.94722E-4
49	Adipose subcutaneous	-0.05001	0.09632	9.1209E-4
50	Joint tissue synovium	-0.06515	0.01103	-0.00108
51	Skeletal muscle	0.28103	-0.00276	5.67782E-4
52	Skeletal muscle-sup. Quad.	0.14975	0.00361	0.00454
53	Skin	0.02511	-0.04216	-2.08378E-4
54	Pericardium	-0.15885	-0.05233	9.12675E-4
55	Heart	0.06282	0.01091	-3.32965E-4
56	Heart atrium	0.00511	0.03273	4.77277E-5
57	Heart ventricle	0.12466	0.02073	7.67343E-4
58	Aorta	-0.07828	-0.00701	-9.50775E-4
59	Coronary artery	-0.08049	0.02606	8.78745E-5
60	Saphenous vein	-0.06853	-0.01143	5.36649E-4

61	Vena cava	0.04146	0.02372	0.00201
62	Trachea	-0.00679	-0.04172	-7.31785E-4
63	Bronchus	-0.07813	0.0065	-7.85764E-4
64	Lung	-0.08811	0.06728	-7.65704E-4
65	Adrenal gland cortex	0.06495	0.00135	-8.89138E-4
66	Pancreas	0.08974	0.00422	6.15043E-4
67	Pituitary gland	0.23849	-0.01573	7.19812E-4
68	Thyroid gland	-0.07697	-0.02272	-3.97022E-4
69	Ovary	-0.1021	0.00343	-0.00117
70	**Testes**	0.08721	0.39569	**1**
71	Kidney	0.15946	-0.0311	-0.00139
72	Kidney cortex	0.06141	-0.07694	-4.69458E-4
73	Kidney medulla	0.08781	-0.03885	-4.11375E-4
74	Urethra	-0.12793	-0.00957	-8.66727E-4
75	Fallopian tube	-0.13675	-0.02268	-0.0016
76	Uterus	-0.04897	0.06935	-3.76565E-4
77	Myometrium	-0.09354	-7.6435E-4	-3.16721E-4
78	Endometrium	-0.08684	-0.00491	-0.00137
79	Cervix	-0.10549	0.00367	-0.00104
80	Vagina	-0.10939	-0.01428	-6.32884E-4
81	Vulva	0.01544	0.00984	2.42907E-4
82	Mammary gland	-0.0841	-5.80533E-4	-1.44052E-4
83	Nipple cross section	-0.03856	-0.00921	-0.00131
84	Penis	-0.05551	-0.00825	-0.00125
85	Prostate gland	-0.09386	-0.0401	-1.44072E-4
86	Bone marrow	0.00532	0.16588	5.15395E-4
87	Thymus gland	-0.09151	0.02143	-0.00115
88	Lymph node	0.01921	0.44154	-0.00108
89	Spleen	0.00904	0.47385	-0.00116
90	Tonsil	-0.03892	0.42621	5.91467E-4
91	PBMC media BB	-0.12826	0.16665	-3.48472E-4
92	PBMC PMA+ionomycin	-0.19097	-0.04773	0.00232
93	Monocytes resting-30h	0.06389	0.44558	0.00219
94	Monocytes LPS+IFNg-30h	0.04055	0.14308	0.00147
95	**B cells resting-30h**	0.1388	**1**	0.00361
96	B cells antiCD40+IL4-30h	0.02876	0.9774	0.00126
97	T cells resting-30h	-0.02438	0.09947	0.00219
98	T cells antiCD3-30h	0.07684	0.1135	0.00257
99	CD4+	-0.14257	0.04733	3.24902E-4
100	CD4+ antiCD3+antiCD28	-0.0634	-0.05988	-9.55343E-4
101	CD8+	-0.10564	-0.00224	-0.00171
102	CD8+ antiCD3+antiCD28	-0.02323	-0.04484	0.00136
103	Fetal liver	0.02353	0.11673	4.25718E-4
104	Fetal brain	0.16881	0.002	1.31635E-4
105	Placenta	-0.04602	-0.03684	0.01122

* For each individual gene, values were normalized to the maximum expression level (shown in red) after median subtraction.

4.6 References

Altschul, S.F., Madden, T.L., Schäffer, A.A., Zhang, J., Zhang, Z., Miller, W., and Lipman, D.J. (1997). Gapped BLAST and PSI-BLAST: a new generation of protein database search programs. Nucleic Acids Res. *25*, 3389–3402.

Ashcroft, F.M. (1999). Ion Channels and Disease (Academic Press).

Cannon, S.C. (2006). Pathomechanisms in channelopathies of skeletal muscle and brain. Annu. Rev. Neurosci. *29*, 387–415.

Catterall, W.A., Dib-Hajj, S., Meisler, M.H., and Pietrobon, D. (2008). Inherited neuronal ion channelopathies: new windows on complex neurological diseases. J. Neurosci. *28*, 11768–11777.

Choe, H., Zhou, H., Palmer, L.G., and Sackin, H. (1997). A conserved cytoplasmic region of ROMK modulates pH sensitivity, conductance, and gating. Am. J. Physiol. *273*, F516–F529.

Decoursey, T.E. (2013). Voltage-gated proton channels: molecular biology, physiology, and pathophysiology of the H(V) family. Physiol. Rev. *93*, 599–652.

Fujiwara, Y., Kurokawa, T., Takeshita, K., Kobayashi, M., Okochi, Y., Nakagawa, A., and Okamura, Y. (2012). The cytoplasmic coiled-coil mediates cooperative gating temperature sensitivity in the voltage-gated H(+) channel Hv1. Nat Commun *3*, 816.

Gonzalez, C., Koch, H.P., Drum, B.M., and Larsson, H.P. (2010). Strong cooperativity between subunits in voltage-gated proton channels. Nat. Struct. Mol. Biol. *17*, 51–56.

Hall, J.E., and Guyton, A.C. (2010). Guyton and Hall Textbook of Medical Physiology (Saunders).

Heijne, von, G. (1992). Membrane protein structure prediction. Hydrophobicity analysis and the positive-inside rule. J. Mol. Biol. *225*, 487–494.

Hevezi, P., Moyer, B.D., Lu, M., Gao, N., White, E., Echeverri, F., Kalabat, D., Soto, H., Laita, B., Li, C., et al. (2009). Genome-wide analysis of gene expression in primate taste buds reveals links to diverse processes. PLoS ONE *4*, e6395.

Hille, B. (2001). Ion Channels of Excitable Membranes (Sunderland: Sinauer Associates Inc).

Hirokawa, T., Boon-Chieng, S., and Mitaku, S. (1998). SOSUI: classification and secondary structure prediction system for membrane proteins. Bioinformatics *14*, 378–379.

Hong, L., Pathak, M.M., Kim, I.H., Ta, D., and Tombola, F. (2013). Voltage-sensing domain of voltage-gated proton channel Hv1 shares mechanism of block with pore domains. Neuron *77*, 274–287.

Horton, R.M., Cai, Z.L., Ho, S.N., and Pease, L.R. (1990). Gene splicing by overlap extension:

tailor-made genes using the polymerase chain reaction. BioTechniques *8*, 528–535.

Koch, H.P., Kurokawa, T., Okochi, Y., Sasaki, M., Okamura, Y., and Larsson, H.P. (2008). Multimeric nature of voltage-gated proton channels. Proc. Natl. Acad. Sci. U.S.a. *105*, 9111–9116.

Kohout, S.C., Bell, S.C., Liu, L., Xu, Q., Minor, D.L., and Isacoff, E.Y. (2010). Electrochemical coupling in the voltage-dependent phosphatase Ci-VSP. Nat. Chem. Biol. *6*, 369–375.

Kulleperuma, K., Smith, S.M.E., Morgan, D., Musset, B., Holyoake, J., Chakrabarti, N., Cherny, V.V., Decoursey, T.E., and Pomès, R. (2013). Construction and validation of a homology model of the human voltage-gated proton channel hHV1. J. Gen. Physiol. *141*, 445–465.

Lacroix, J.J., and Bezanilla, F. (2011). Control of a final gating charge transition by a hydrophobic residue in the S2 segment of a K+ channel voltage sensor. Proc. Natl. Acad. Sci. U.S.a. *108*, 6444–6449.

Lee, H.Y., Greene, L.A., Mason, C.A., and Manzini, M.C. (2009). Isolation and culture of post-natal mouse cerebellar granule neuron progenitor cells and neurons. J Vis Exp.

Lee, S.-Y., Letts, J.A., and Mackinnon, R. (2008). Dimeric subunit stoichiometry of the human voltage-dependent proton channel Hv1. Proc. Natl. Acad. Sci. U.S.a. *105*, 7692–7695.

Li, Q., Wanderling, S., Paduch, M., Medovoy, D., Singharoy, A., McGreevy, R., Villalba-Galea, C.A., Hulse, R.E., Roux, B., Schulten, K., et al. (2014). Structural mechanism of voltage-dependent gating in an isolated voltage-sensing domain. Nat. Struct. Mol. Biol. *21*, 244–252.

Li, S.J., Zhao, Q., Zhou, Q., Unno, H., Zhai, Y., and Sun, F. (2010). The role and structure of the carboxyl-terminal domain of the human voltage-gated proton channel Hv1. J. Biol. Chem. *285*, 12047–12054.

Liman, E.R., Tytgat, J., and Hess, P. (1992). Subunit stoichiometry of a mammalian K+ channel determined by construction of multimeric cDNAs. Neuron *9*, 861–871.

Lupas, A., Van Dyke, M., and Stock, J. (1991). Predicting coiled coils from protein sequences. Science *252*, 1162–1164.

Marr, D. (1969). A theory of cerebellar cortex. The Journal of Physiology *202*, 437–470.

Murata, Y., Iwasaki, H., Sasaki, M., Inaba, K., and Okamura, Y. (2005). Phosphoinositide phosphatase activity coupled to an intrinsic voltage sensor. Nature *435*, 1239–1243.

Musset, B., Smith, S.M.E., Rajan, S., Cherny, V.V., Sujai, S., Morgan, D., and Decoursey, T.E. (2010). Zinc inhibition of monomeric and dimeric proton channels suggests cooperative gating. The Journal of Physiology *588*, 1435–1449.

Musset, B., Smith, S.M.E., Rajan, S., Morgan, D., Cherny, V.V., and Decoursey, T.E. (2011). Aspartate 112 is the selectivity filter of the human voltage-gated proton channel. Nature

480, 273–277.

Neuhaus, H., and Hollemann, T. (2009). Kidney specific expression of cTPTE during development of the chick embryo. Gene Expr. Patterns *9*, 568–571.

Okamura, Y. (2007). Biodiversity of voltage sensor domain proteins. Pflugers Arch. *454*, 361–371.

Okochi, Y., Sasaki, M., Iwasaki, H., and Okamura, Y. (2009). Voltage-gated proton channel is expressed on phagosomes. Biochem. Biophys. Res. Commun. *382*, 274–279.

Qiu, F., Rebolledo, S., Gonzalez, C., and Larsson, H.P. (2013). Subunit interactions during cooperative opening of voltage-gated proton channels. Neuron *77*, 288–298.

Ramsey, I.S., Moran, M.M., Chong, J.A., and Clapham, D.E. (2006). A voltage-gated proton-selective channel lacking the pore domain. Nature *440*, 1213–1216.

Ramsey, I.S., Ruchti, E., Kaczmarek, J.S., and Clapham, D.E. (2009). Hv1 proton channels are required for high-level NADPH oxidase-dependent superoxide production during the phagocyte respiratory burst. Proc. Natl. Acad. Sci. U.S.a. *106*, 7642–7647.

Ratzan, W.J., Evsikov, A.V., Okamura, Y., and Jaffe, L.A. (2011). Voltage sensitive phosphoinositide phosphatases of Xenopus: their tissue distribution and voltage dependence. J. Cell. Physiol. *226*, 2740–2746.

Roth, R.B., Hevezi, P., Lee, J., Willhite, D., Lechner, S.M., Foster, A.C., and Zlotnik, A. (2006). Gene expression analyses reveal molecular relationships among 20 regions of the human CNS. Neurogenetics *7*, 67–80.

Sasaki, M., Takagi, M., and Okamura, Y. (2006). A voltage sensor-domain protein is a voltage-gated proton channel. Science *312*, 589–592.

Scheiffele, P., Fan, J., Choih, J., Fetter, R., and Serafini, T. (2000). Neuroligin expressed in nonneuronal cells triggers presynaptic development in contacting axons. Cell *101*, 657–669.

Schmahmann, J.D., and Sherman, J.C. (1998). The cerebellar cognitive affective syndrome. Brain *121 (Pt 4)*, 561–579.

Smith, S.M.E., Morgan, D., Musset, B., Cherny, V.V., Place, A.R., Hastings, J.W., and Decoursey, T.E. (2011). Voltage-gated proton channel in a dinoflagellate. Proc. Natl. Acad. Sci. U.S.a. *108*, 18162–18167.

Suh, B.-C., Leal, K., and Hille, B. (2010). Modulation of high-voltage activated Ca(2+) channels by membrane phosphatidylinositol 4,5-bisphosphate. Neuron *67*, 224–238.

Takeshita, K., Sakata, S., Yamashita, E., Fujiwara, Y., Kawanabe, A., Kurokawa, T., Okochi, Y., Matsuda, M., Narita, H., Okamura, Y., et al. (2014). X-ray crystal structure of voltage-gated

proton channel. Nat. Struct. Mol. Biol.

Tao, X., Lee, A., Limapichat, W., Dougherty, D.A., and Mackinnon, R. (2010). A gating charge transfer center in voltage sensors. Science *328*, 67–73.

Tapparel, C., Reymond, A., Girardet, C., Guillou, L., Lyle, R., Lamon, C., Hutter, P., and Antonarakis, S.E. (2003). The TPTE gene family: cellular expression, subcellular localization and alternative splicing. Gene *323*, 189–199.

Thisse, C., and Thisse, B. (2008). High-resolution in situ hybridization to whole-mount zebrafish embryos. Nat Protoc *3*, 59–69.

Thomas, R.C., and Meech, R.W. (1982). Hydrogen ion currents and intracellular pH in depolarized voltage-clamped snail neurones. Nature *299*, 826–828.

Tombola, F., Ulbrich, M.H., and Isacoff, E.Y. (2008). The voltage-gated proton channel Hv1 has two pores, each controlled by one voltage sensor. Neuron *58*, 546–556.

Tombola, F., Ulbrich, M.H., Kohout, S.C., and Isacoff, E.Y. (2010). The opening of the two pores of the Hv1 voltage-gated proton channel is tuned by cooperativity. Nat. Struct. Mol. Biol. *17*, 44–50.

Vacher, H., Mohapatra, D.P., and Trimmer, J.S. (2008). Localization and targeting of voltage-dependent ion channels in mammalian central neurons. Physiol. Rev. *88*, 1407–1447.

Walker, S.M., Downes, C.P., and Leslie, N.R. (2001). TPIP: a novel phosphoinositide 3-phosphatase. Biochem. J. *360*, 277–283.

Wu, L.-J., Wu, G., Akhavan Sharif, M.R., Baker, A., Jia, Y., Fahey, F.H., Luo, H.R., Feener, E.P., and Clapham, D.E. (2012). The voltage-gated proton channel Hv1 enhances brain damage from ischemic stroke. Nat. Neurosci. *15*, 565–573.

Wu, Y., Dowbenko, D., Pisabarro, M.T., Dillard-Telm, L., Koeppen, H., and Lasky, L.A. (2001). PTEN 2, a Golgi-associated testis-specific homologue of the PTEN tumor suppressor lipid phosphatase. J. Biol. Chem. *276*, 21745–21753.

Yu, F.H., and Catterall, W.A. (2004). The VGL-chanome: a protein superfamily specialized for electrical signaling and ionic homeostasis. Sci. STKE *2004*, re15.

Yudin, Y., Lukacs, V., Cao, C., and Rohacs, T. (2011). Decrease in phosphatidylinositol 4,5-bisphosphate levels mediates desensitization of the cold sensor TRPM8 channels. The Journal of Physiology *589*, 6007–6027.

Chapter 5: Conclusion and future studies

5.1 Overview of thesis work

Through my dissertation work, I have characterized one novel protein, HVRP1, associated with the families of voltage-gated proteins without a pore domain, which includes Hv1, and contributed work towards development of inhibitors of Hv1.

In Chapters 2 and 3, I described the work done to better understand permeation through the Hv1 VSD by means of channel blockers. Until our work, no intracellular blockers of Hv1 were known. The guanidine derivatives that bind to the Hv1 channel from the intracellular side shown here are useful tools for studying the mechanisms of gating and permeation through the Hv1 VSD. We showed that one molecule in particular, 2GBI, blocked the channel only in the open conformation, and proposed a mechanism of binding in which an intracellular gate regulates access of the blocker to its binding site in the core of the VSD. Following this work, we showed that a modified version of 2GBI, ClGBI, is able to block Hv1 from the extracellular side, due to its decreased polarity and improved membrane partitioning. These data open the way for further optimization of guanidine derivatives using the 2GBI scaffold as a base. It is our hope that this work can be used to develop treatments for ischemic stroke or cancer, diseases that Hv1 is implicated in.

In Chapter 4, I discussed the initial characterization of HVRP1, the first VSD-containing protein without a pore domain to be found in neuronal cells. HVRP1 is localized specifically

to cerebellar granule cells, at the post-synaptic side of contacts between mossy fibers and granule cells. HVRP1 shares a similar structural organization with Hv1 as well as having a similar amino acid sequence, yet does not conduct protons or ions. We believe that HVRP1 represents a new family of voltage-sensitive proteins with a function as of yet unknown to VSD-containing proteins. In addition, understanding why HVRP1 is not able to conduct ions, despite its similarity to the Hv1 channel, could reveal basic structural principles underlying ion conduction in VSDs.

The work laid out in this dissertation represents only the initial stages of the characterization of a novel voltage-sensing protein. The discovery of HVRP1 is significant due to it being the first of its kind: a VSD-containing protein without a pore domain, found in neuronal cells. The body of this thesis serves to enhance the understanding of the field of voltage-sensing protein research, particularly of those proteins with VSDs and without pore domains. From this basis I see the potential for continuing the search for more proteins closely related to both Hv1 and HVRP1, containing a VSD which functions as more than just a voltage sensor.

5.2 Investigation of the physiological role of HVRP1

The most significant breakthrough in the study of HVRP1 would be the determination of thus protein's function. The limited homology of the HVRP1 C-terminus to other known proteins in particular suggests that it may have a function as of yet unassociated with VSD-

containing proteins. I believe that answering the following questions in future studies would be an essential step toward the determination of the physiological role of HVRP1.

First, does the overexpression or knockdown of HVRP1 alter the electrical excitability of cerebellar granule neurons? The HVRP1 protein is very selectively expressed in these cells. Additionally, HVRP1 is found only at these cells' contacts with glutamatergic mossy fibers. Here, HVRP1 is able to detect small and fast depolarizations. These observations suggest that the VSD of HVRP1may be responsible for modulating the activity of post-synaptic ion channels. This activity could be in response to excitatory post-synaptic potentials or back-propagating action potentials in the cerebellar granule cell dendrites.

I have demonstrated in Chapter 4 that HVRP1 can be detected in cultured cerebellar granule neurons isolated from post-natal mice. Use of this primary culture would allow us to study the HVRP1 protein in its native state, with any as of yet unidentified proteins that may co-assemble or interact with HVRP1. Over-expression of HVRP1 in HEK293A cells would not allow for this environment. Here, we would be able to perform electrophysiology experiments on the cerebellar granule neurons and evaluate their electrical excitability with or without the knockdown of HVRP1 by RNA interference.

Second, as briefly mentioned earlier, which other cerebellar proteins, if any, directly interact with HVRP1? I discussed in Chapter 4 that HVRP1 is able to detect changes in membrane potential but could not conduct ions when we expressed this protein in heterologous systems. This may be due to the nature of the heterologous system, which

may be lacking in interacting proteins necessary for the function of HVRP1. We believe the best approach for this study is to use immunoprecipitation of HVRP1 and, following this, mass spectrometry analysis to determine interacting proteins. Mass spectrometry analysis is outside the scope of our laboratory and thus this study would most likely be completed by a collaboration with another lab. An alternative approach to identify HVRP1 interacting proteins could be the use of yeast two hybrid assays using the N- and C-termini of HVRP1 as baits.

Third, does HVRP1 form a multimer? Considering the two families of VSD-containing proteins with a pore domain, the voltage-sensitive phosphatases function as monomers (Kohout et al., 2008), but voltage-gated proton channels function as dimers, and the region responsible for dimerization of the proton channels is the coiled-coil domain (Tombola et al., 2008)3. An analysis with the program Coils (Lupas et al., 1991) as well as homology modeling reveal that the coiled-coil domains of HVRP1 and Hv1 are highly similar. From this, we hypothesize that HVRP1 may also be using this coiled-coil domain in order to multimerize.

Hv1 is able to function and conduct protons when monomerized, since each subunit of Hv1 contains its own voltage sensor which acts as a pore (Tombola et al., 2008). However, it was found that as a dimer, the opening of the two Hv1 pores is cooperative (Tombola et al., 2010). I have begun preliminary studies to determine whether HVRP1, like Hv1, forms multimers in its functional state. The answer to this question may provide certain insights into the mechanism of HVRP1's function, as it did for Hv1.

The initial approach taken was to create a version of only the HVRP1's C-terminus. We believed that without the VSD, HVRP1 would no longer be able to properly traffic to the plasma membrane. To this truncated protein we attached a GFP tag. The truncated protein, which we called HVRP1-CTFP (**C-T**erminus, **F**luorescent **P**rotein), was co-expressed with non-GFP-tagged wild-type HVRP1 into HEK293A cells in hopes that CTFP would be able to multimerize with the intact protein. If so, we expected to see fluorescence on the membrane, since the wild-type protein, properly trafficking to the plasma membrane, would not fluoresce on its own. Difficulties in the optimization of TIRF microscopy prevented definitive results from these experiments so far, but I believe that with refinements to the technique, we will be able to use or adapt this experimental approach to understand HVRP1 multimerization or lack thereof.

An alternative strategy that I began was SDS-Page/Western blot analysis of crosslinked HVRP1 protein. The coiled-coil domain of HVRP1 was deleted either partially or entirely, and over-expressed in HEK293A cells along with the intact protein. This technique, too, has not yet been optimized since several artifacts not indicative of true multimerization have been seen in our results. So far, I have worked out the conditions to detect the non-crosslinked protein as a monomer in Western blot without the interference of intersubunit bridges formed by endogenous cysteines. I plan to continue these experiments to verify if the bands in the Western blot representing the multimerized proteins disappear when comparing the coiled-coil domain-deleted protein to the wild-type protein. I hope also to

use these experiments to determine whether the coiled-coil domain of HVRP1 is involved with the subcellular localization of the protein, as it is with Hv1 (Li et al., 2010).

These questions I posed represent long-term goals for the characterization of HVRP1. However, I also propose a short-term goal for which I have already taken immediate steps. This goal involves the study of the HVRP1 VSD in relation to that of Hv1. In Chapters 2 and 3, I discussed the inhibition of Hv1, which provides insight into design of drugs for the treatment of various cancers. These inhibition studies involve the blocking of the Hv1 pore, which, as previously discussed, is also the VSD. A better understanding of why the HVRP1 VSD seemingly does not conduct ions or protons would approach the issue of Hv1 inhibition from another angle.

This study was touched upon in Chapter 4, in a discussion of the aspartate at residue 112 in Hv1, proposed to be the selectivity filter of Hv1 (Musset et al., 2011). We found that the mutation of the corresponding residue in HVRP1 to match that of Hv1, V111D, did not allow ion permeation through the HVRP1 VSD. We concluded from these studies that the presence of this aspartate is not sufficient for ion permeation in HVRP1 and thus the functional divergence between HVRP1 and Hv1 may extend much more beyond single residue differences.

The next step we took in this study was to evaluate the key differences between HVRP1 and Hv1. We analyzed the sequences of the VSDs from human HVRP1 and Hv1 and compared them with the VSD sequence of Hv1 from *Ciona intestinalis*. We hypothesized that residues

that are necessary for the function of proton permeation will be maintained during evolution and so they will be conserved in the Hv1 proteins from different species. On the other hand, the corresponding residues in HVRP1 would be less likely to be conserved because not needed to perform the function of ion transport. We identified a pull of 12 residues in the core of the VSD which were conserved between human and Ciona Hv1 but significantly different in human HVRP1. Through a systematic approach, we mutated each of the 12 residues in HVRP1 to the corresponding Hv1 residues. The mutations for the new HVRP1 construct are listed in Table S5.1. I plan to express this mutant in *Xenopus* oocytes by RNA injection, and to measure currents by two-electrode voltage-clamp, as described in Chapter 4. The proton current generated by Hv1 will serve as a positive control for this experiment.

These twelve mutations, all present in conjunction with each other, should make the VSD of HVRP1 even more similar to that of Hv1. It is possible that these twelve mutations all together represent the fundamental structural difference between the HVRP1 and Hv1 VSDs. If this is the case, these twelve changes could allow ion permeation through the HVRP1 VSD. If this drastic change is not sufficient to allow proton or ion permeation through the VSD during two-electrode voltage-clamp experiments, we would take this to mean that there is an even more fundamental difference in the structure or characteristics of the HVRP1 VSD compared to the Hv1 VSD that prevents permeation.

To verify that this large number of mutations does not disrupt the synthesis or plasma membrane targeting of the HVRP1 protein in the heterologous system of *Xenopus* oocytes,

we also designed an additional experiment in which HVRP1 with twelve mutations is also expressed in a vector that allows expression in HEK293A cells. This construct is tagged with GFP, so that we can verify both the proper expression of the protein and its localization to the plasma membrane. In the case that there is either be no fluorescence at all, indicating a lack of synthesized protein, or improper localization meaning that currents cannot be recorded from two-electrode voltage-clamp, we would scale back the number of mutations until we see a viable protein that can be tested.

I expect to generate enough data using these mutants to give a clearer evaluation of the degree of similarity of the HVRP1 and Hv1 VSDs, as well as bringing us closer to understanding why the HVRP1 VSD does not conduct ions. Whether this will provide a novel method for blockage of the Hv1 pore remains to be seen, but these studies will inevitably aid in the study of the HVRP1 protein's function while at the same time providing insight into the mechanism of conduction through the VSD.

Table 5.1. Mutations in the 12-mutant HVRP1 construct.

Transmembrane segment	Mutations
S1	V111D, L115V, T116L
S2	S151M, T153I
S3	G175A, P184L, M185D
S4	K213A, D217N, A218G, P222S

5.3 Significance of Hv1 inhibition for therapy and development of inhibitors

Ion channels have long been important targets for drugs for the pharamaceutical industry. Membrane proteins, a group to which ion channels belong, are 20 – 30% of the human genome (Fagerberg et al., 2010), but are the targets of over half of the currently known drugs (Bakheet and Doig, 2009; Yildirim et al., 2007). Part of the reason for this may be that membrane proteins uniquely bridge three kinds of biochemical environments – the intracellular, the extracellular, and the membrane.

As a potential target for breast cancer and colorectal cancer diagnosis and prognosis, Hv1 is an attractive subject of channel inhibition research. It is exciting that our work has shown that it is possible to apply an inhibitor to Hv1 that will block it from the extracellular side, making drug design much more feasible. To aid in this, our studies have provided much understanding of the binding environment of guanidine derivative blockers of Hv1, and how they interact with the Hv1 VSD. It is our hope that these data have clinical significance with the area of cancer treatment in mind.

5.4 Hv1 as a target for cancer treatment

The studies by Wang et. al demonstrated that Hv1 is specifically expressed in highly metastatic human breast cancer tissues and cell lines (Wang et al., 2012) and in colorectal tumor tissues and cell lines (Wang et al., 2013). In both cases, Hv1 inhibition caused a marked decrease in division and migration of cancer cells.

We hypothesize that high affinity Hv1 channel blockers such as those described in Chapters 2 and 3 may promote anti-metastatic activity during cancer treatment. To investigate this hypothesis, we will focus our studies using the breast cancer cell line identified by Wang et. al to highly express Hv1, the MB-231 cell line (Wang et al., 2012). The work by this group showed that the high expression of Hv1 in the MB-231 cell line promotes invasiveness and metastasis of the breast cancer cells, by means of facilitating H^+ efflux. This contributes to creating a high intracellular pH and low extracellular pH in an environment of already highly dysregulated pH typical of many cancers. The cancer cell survival is enhanced in turn by the resulting inhibition of acid-induced apoptosis. Additionally, acidification of the extracellular matrix then stimulates proteases that aid the cancer cell invasiveness (Giannelli and Antonaci, 2002).

The functional block of Hv1 by RNA interference has shown to successfully inhibit the proliferation and migration of breast cancer both *in vitro* and *in vivo* (Wang et al., 2012). Preliminary data from wound healing assays, performed as previously described (Wang et al., 2011), suggested that a similar reduction in cancer cell proliferation and migration could be achieved through Hv1 block by small molecules such as those described in Chapters 2 and 3. The application of GBOZ, GBI, and ClGBI to MB-231 cells was tested by a wound healing assay in which the cells, grown in a monolayer, were mechanically wounded. Under normal conditions, cells grow over time to close the wound. Each molecule was tested for its efficacy in blocking or slowing down this growth of cells. Of these, ClGBI acted as the strongest blocker, in a dose-dependent manner. These preliminary

results generated by Mona Wood indicated that Hv1 blockers have a high potential for use as anti-metastatic cancer treatment.

5.4.1 Experimental procedures

In collaboration with the Tobias group at UC Irvine, we propose a series of experiments to design effective Hv1 channel blockers. The wound assay experiment on cancer cell lines natively expressing the protein will be used to assess whether cell growth is slowed or stopped by the designed blockers. We also plan to perform a control experiment to test for the possibility that our blockers are inhibiting cancer progression through a mechanism other than Hv1 blockade. The Hv1 protein expressed in the cell lines will be silenced by RNA interference. We then expect to see the same rate of wound healing in Hv1-silenced cells as in the control cells. This is an important experiment for future drug design, since it may be a useful tool in designing blockers with higher channel affinity, indicated by a decrease in off-target effects seen in the Hv1-silenced cells.

We plan to use immunostaining with an antibody against Hv1 in order to verify the presence or knockdown of Hv1 protein in the cell cultures. These experiments are now in progress, testing our Western blotting system to verify to presence of Hv1 protein in our cell cultures.

5.5 Reflectin and practical uses in technology

Alongside these experiments, we plan to approach the issue of Hv1 as a target for drugs from other angles. Our proposed work for testing Hv1 channel blockers in the previous sections is based upon the drug design of these guanidine derivative channel blockers as described in Chapters 2 and 3. We also envision a use for Hv1 in drug discovery, in a larger scale screening for new inhibitors. High-throughput screening would be a favorable method for discovery of new Hv1 inhibitors, and we hope that our studies could someday be used in the development of such a system.

In conjunction with these ideas, we are pairing the Hv1's acid extrusion functions with another practical use not yet discussed in this thesis. In addition to its high potential as a target for cancer treatment, we would like to utilize Hv1 in an exploration of camouflage technology. There are numerous practical applications for camouflage and stealth technology, particularly in the military. The Gorodetsky group at UC Irvine is using the reflectin family of proteins to explore this avenue of research. Reflectins are proteins identified in cephalopods, which use these proteins to manipulate incident light. Reflective platelets from squid were found to be composed of reflectin proteins, which have a unique amino acid composition: the four relatively rare residues tyrosine, methionine, arginine, and tryptophan make up approximately 57% of the reflectin protein, while relatively common residues alanine, isoleucine, leucine, and lysine do not appear at all. The five repeating domains that make up the protein are conserved throughout the family of

reflectins. This family is a key example of nanofabrication in animal systems (Crookes et al., 2004).

A simple fabrication technique has been developed to generate thin films of a reflectin isoform from *Loligo (Doryteuthis) pealeii* onto graphene oxide-coated substrates. The isoform used is the histidine-tagged reflectin A1 (Rfa1). The reflectance of these coatings can then be tuned over 600 nm, the largest tunable reflectance window of any currently available biological thin film. This property of finely tuning the films allows the reflectin to appear and disappear from the visible spectrum, and likewise appear and disappear when visualized with infrared imaging. Preliminary experiments showed that use of an acid vapor could be used to tune the reflectin and induce color change. These findings and further research could allow for an inexpensive and reproducible method for creating dynamically tunable camouflage coatings on many surfaces (Phan et al., 2013), which would have numerous applications in military settings in which improved stealth and camouflage technology could better protect members of the armed forces.

5.5.1 Experimental procedures

We hypothesize that the activity of Hv1 on cells grown on to a reflectin film will be sufficient to alter the visible color of the reflectin and are collaborating with the Gorodetsky group to undertake these studies. We over-expressed Hv1 in HEK293A cells. Additionally, we are using two cell lines that natively express the Hv1 protein, BV2 (Song et al., 2012) and MB-231 (Wang et al., 2012). We have begun preliminary experiments to test the

viability and growth to confluence of all three cell lines on the reflectin-coated chips and found that the BV2 and MB-231 can quickly grow a monolayer on the chips.

Currently, we are optimizing a quantitative system for assessing the degree of color change on the reflectin. We expect to be able to evaluate the difference in reflectin-coated chips with cell growth versus reflectin-coated chips with no cells. The H^+ extrusion by the Hv1 channels should create a pH environment different from that of the control chips without cells. We hope to use our designed Hv1 blockers or RNA interference in order to achieve the same color in the reflectin as in the control chips without cells.

One goal of this study is the synthesis of a rigorous high-throughput screening assay for Hv1 channel inhibitors to enhance the process of drug development. One method currently in use for measurement of ion channel function during high-throughput screening is FLIPR (**Fl**uorescent **I**maging **P**late **R**eader). When originally developed, it was used to detect G-protein coupled receptor activation by the concentration of intracellular Ca^{2+}. FLIPR can measure the movement of Ca^{2+} by loading the cells with a fluorescent Ca^{2+} indicator dye, and cells are treated with a ligand for the receptor that ultimately leads to elevation of intracellular calcium. Alternatively, calcium elevation can be triggered by high KCl, which opens voltage-gated Ca^{2+} channels on the plasma membrane. An increase in fluorescence will therefore report on G-protein coupled receptor activation or calcium channel activity. Now, FLIPR can also be used to measure the intracellular flux of K^+ and other ions (Sittampalam et al., 2004). The design of a fast and accurate measurement system for the change in color by reflectin could therefore become a similarly useful tool in screening

compounds that alter extracellular proton concentration by altering the activity of Hv1 channels.

5.6 Final remarks

The most recent estimate for the number of protein-coding genes in the human genome is approximately 19,000 (Ezkurdia et al., 2013), although the true number of protein-coding genes is still under investigation. It is estimated now that about 20% of the protein-coding genes are yet uncharacterized. In other words, there is still much work to be done to understand the genes associated with disease, to learn how these genes may be used as targets for therapy, and to better understand ourselves through knowledge of the human genome. The work in this thesis demonstrates my ability to take the first steps in a goal so large and open-ended as "characterize a gene." I have been able to begin the work in characterization of the protein coded by gene *C15ORF27*, which we named HVRP1, by first focusing on localization studies, and then moving on to experiments that aim to elucidate its function. Through this work, I have also learned a variety of techniques outside the environment of our lab as was necessary to tackle the problem of HVRP1 characterization from many angles.

Ultimately, the goal would be to definitively show that HVRP1 is physiologically relevant for the electrical excitability of cerebellar granule neurons, thus contributing to the neuronal circuitry of the cerebellum. The studies laid out in this thesis represent only the early stages of the immense scope of work necessary to characterize a protein-coding gene.

The characterization of a gene is an undertaking larger than the scope of a single research group and I believe that the skills I have learned and demonstrated here are important and necessary for making contributions to such a project.

My data contributes to this dynamic field of voltage-sensitive protein research with the angle of drug design in mind. I consider it fortunate that the novel protein I have chosen to focus my studies on is so closely related to other voltage-sensitive proteins involved in human disease. It is my hope that the study of HVRP1 opens avenues of research into further treatment of disease, as is the case for Hv1 research currently.

5.7 References

Bakheet, T.M., and Doig, A.J. (2009). Properties and identification of human protein drug targets. Bioinformatics *25*, 451–457.

Crookes, W.J., Ding, L.-L., Huang, Q.L., Kimbell, J.R., Horwitz, J., and McFall-Ngai, M.J. (2004). Reflectins: the unusual proteins of squid reflective tissues. Science *303*, 235–238.

DeCoursey, T.E., and Cherny, V.V. (1996). Voltage-activated proton currents in human THP-1 monocytes. J Membrane Biol *152*, 131–140.

Ezkurdia, I., Juan, D., Rodriguez, J.M., Frankish, A., Diekhans, M., Harrow, J., Vazquez, J., Valencia, A., and Tress, M.L. (2013). The shrinking human protein coding complement: are there fewer than 20,000 genes? arXiv Preprint arXiv:1312.7111.

Fagerberg, L., Jonasson, K., Heijne, von, G., Uhlén, M., and Berglund, L. (2010). Prediction of the human membrane proteome. Proteomics *10*, 1141–1149.

Giannelli, G., and Antonaci, S. (2002). Gelatinases and their inhibitors in tumor metastasis: from biological research to medical applications. Histol. Histopathol. *17*, 339–345.

Kohout, S.C., Ulbrich, M.H., Bell, S.C., and Isacoff, E.Y. (2008). Subunit organization and functional transitions in Ci-VSP. Nat. Struct. Mol. Biol. *15*, 106–108.

Li, S.J., Zhao, Q., Zhou, Q., Unno, H., Zhai, Y., and Sun, F. (2010). The role and structure of the carboxyl-terminal domain of the human voltage-gated proton channel Hv1. J. Biol. Chem. *285*, 12047–12054.

Lupas, A., Van Dyke, M., and Stock, J. (1991). Predicting coiled coils from protein sequences. Science *252*, 1162–1164.

Musset, B., Smith, S.M.E., Rajan, S., Morgan, D., Cherny, V.V., and Decoursey, T.E. (2011). Aspartate 112 is the selectivity filter of the human voltage-gated proton channel. Nature *480*, 273–277.

Phan, L., Walkup, W.G., Ordinario, D.D., Karshalev, E., Jocson, J.-M., Burke, A.M., and Gorodetsky, A.A. (2013). Reconfigurable infrared camouflage coatings from a cephalopod protein. Adv. Mater. Weinheim *25*, 5621–5625.

Sakai, H., Li, G., Hino, Y., Moriura, Y., Kawawaki, J., Sawada, M., and Kuno, M. (2013). Increases in intracellular pH facilitate endocytosis and decrease availability of voltage-gated proton channels in osteoclasts and microglia. The Journal of Physiology *591*, 5851–5866.

Sittampalam, G.S., Gal-Edd, N., Arkin, M., Auld, D., Austin, C., Bejcek, B., Glicksman, M., Inglese, J., Lemmon, V., Li, Z., et al. (2004). FLIPR™ Assays for GPCR and Ion Channel Targets

(Bethesda (MD): Eli Lilly & Company and the National Center for Advancing Translational Sciences).

Song, J.-H., Marszalec, W., Kai, L., Yeh, J.Z., and Narahashi, T. (2012). Antidepressants inhibit proton currents and tumor necrosis factor-α production in BV2 microglial cells. Brain Res. *1435*, 15–23.

Tombola, F., Ulbrich, M.H., and Isacoff, E.Y. (2008). The voltage-gated proton channel Hv1 has two pores, each controlled by one voltage sensor. Neuron *58*, 546–556.

Tombola, F., Ulbrich, M.H., Kohout, S.C., and Isacoff, E.Y. (2010). The opening of the two pores of the Hv1 voltage-gated proton channel is tuned by cooperativity. Nat. Struct. Mol. Biol. *17*, 44–50.

Wang, Y., Li, S.J., Pan, J., Che, Y., Yin, J., and Zhao, Q. (2011). Specific expression of the human voltage-gated proton channel Hv1 in highly metastatic breast cancer cells, promotes tumor progression and metastasis. Biochem. Biophys. Res. Commun. *412*, 353–359.

Wang, Y., Li, S.J., Wu, X., Che, Y., and Li, Q. (2012). Clinicopathological and biological significance of human voltage-gated proton channel Hv1 protein overexpression in breast cancer. J. Biol. Chem. *287*, 13877–13888.

Wang, Y., Wu, X., Li, Q., Zhang, S., and Li, S.J. (2013). Human voltage-gated proton channel hv1: a new potential biomarker for diagnosis and prognosis of colorectal cancer. PLoS ONE *8*, e70550.

Yildirim, M.A., Goh, K.-I., Cusick, M.E., Barabási, A.-L., and Vidal, M. (2007). Drug-target network. Nat. Biotechnol. *25*, 1119–1126.